

ISSN number 0971 - 9709



The Journal of Indian Geophysical Union

AN OPEN ACCESS BIMONTHLY JOURNAL OF IGU

VOLUME 23, ISSUE 5, September 2019



Journal of Indian Geophysical Union Editorial Board	Indian Geophysical Union Executive Council
Chief Editor O.P. Pandey (Geosciences), Hyderabad	President Prof. Shailesh Nayak, Director, National Institute of Advanced Studies, Bengaluru
Associate Editors Sandeep Gupta (Seismology), Hyderabad G.R. Ravindra Kumar (Geology, Geochemistry), Trivandrum A.K. Chaubey (Marine Geosciences), Mumbai Elango Lakshmanan (Hydrology, Ground water), Chennai S.N. Tripathi (Atmospheric Sciences), Kanpur	Vice-Presidents Dr. VM Tiwari, Director, CSIR-NGRI, Hyderabad Dr. Sunil K. Singh, Director, CSIR-NIO, Goa Prof. Talat Ahmad, VC, JMI, New Delhi Shri AK Dwivedi, Director (Exploration), ONGC, New Delhi
Editorial Team Solid Earth Geosciences: Vineet Gahlaut (Geodynamics), New Delhi M.R.K. Prabhakara Rao (Ground Water Geophysics), Hyderabad S.P. Sharma (Exploration Geophysics), Kharagpur Mita Rajaram (Geomagnetism), Mumbai K. Mallick (Exploration Geophysics), Hyderabad Rima Chatterjee (Exploration Geophysics), Dhanbad J.R. Kayal (Seismology), Kolkata N.V. Chalapathi Rao (Geology, Geochemistry & Geochronology), Varanasi V.V. Sessa Sai (Geology & Geochemistry), Hyderabad Marine Geosciences and Atmospheric and Space Sciences: K.S.R. Murthy (Marine Geophysics), Visakhapatnam Rajiv Nigam (Marine Geology), Goa Vijay P. Kanawade (Atmospheric Sciences), Hyderabad Umesh Kulshrestha (Atmospheric Sciences), New Delhi U.S. De (Meteorology), Pune Archana Bhattacharya (Space Sciences), Mumbai Editorial Advisory Committee: Walter D Mooney (Seismology & Natural Hazards), USA Manik Talwani (Marine Geosciences), USA Ravi P. Srivastava (Exploration Geophysics), Norway Larry D Brown (Atmospheric Sciences & Seismology), USA Alfred Kroener (Geochronology & Geology), Germany Irina Artemieva (Lithospheric Studies), Denmark R.N. Singh (Theoretical & Environmental Geophysics), Ahmedabad Rufus D Catchings (Near Surface Geophysics), USA Surjalal Sharma (Atmospheric Sciences), USA H.J. Kumpel (Geosciences, App. Geophysics, Theory of Poroelasticity), Germany Saulwood Lin (Oceanography), Taiwan Jong-Hwa Chun (Petroleum Geosciences), South Korea Xiujuan Wang (Marine Geology & Environment), China Jiro Nagao (Marine Energy and Environment), Japan Managing Editor: ASSRS Prasad (Exploration Geophysics), Hyderabad	Honorary Secretary Dr. Kalachand Sain, CSIR-NGRI Joint Secretary Dr. O. P. Mishra, MoES Organizing Secretary Dr. ASSRS Prasad, CSIR-NGRI Treasurer Mr. Md. Rafique Attar, CSIR-NGRI Executive Members Prof. M. Radhakrishna, IITM, Mumbai Prof. P. Rama Rao, Andhra University, Visakhapatnam Prof. B. Madhusudan Rao, Osmania University, Hyderabad Dr. M. Ravikumar, ISR, Ahmedabad Dr. N. Satyavani, CSIR-NGRI, Hyderabad Dr. Devesh Walia, North-Eastern Hill University, Shilong Dr. N. Puranchandra Rao, NCESS, Thiruvananthapuram Prof. Dinesh Kumar, Kurukshetra University, Kurukshetra Prof. Rima Chatterjee, IIT (ISM), Dhanbad Prof. Manoj Kumar Srivastava, BHU, Varanasi Prof. SKG Krishnamacharyulu, SRTM University, Nanded Dr. P. Sanjeeva Rao, SERB, DST, New Delhi Prof. Surjalal Sharma, University of Maryland, USA Sri GVJ Rao, Oil India Limited, Duliajan Sri N. Chandrashekar, ONGC, Mumbai
EDITORIAL OFFICE Indian Geophysical Union, NGRI Campus, Uppal Road, Hyderabad- 500 007 Telephone: +91 -40-27012799; 27012734; Telefax: +91-04-27171564 E. mail: jigu1963@gmail.com, website: www.j-igu.in	
The Open Access Journal with six issues in a year publishes articles covering Solid Earth Geosciences; Marine Geosciences; and Atmospheric, Space and Planetary Sciences.	
Annual Subscription Individual ₹ 1000 per issue and Institutional ₹ 5000 for six issues Payments should be sent by DD drawn in favour of "The Treasurer, Indian Geophysical Union", payable at Hyderabad, Money Transfer/NEFT/RTGS (Inter-Bank Transfer), Treasurer, Indian Geophysical Union, State Bank of India, Habsiguda Branch, Habsiguda, Uppal Road, Hyderabad- 500 007 A/C: 52191021424, IFSC Code: SBIN0020087, MICR Code: 500002318, SWIFT Code: SBININBBHO9. For correspondence, please contact, Hon. Secretary, Indian Geophysical Union, NGRI Campus, Uppal Road, Hyderabad - 500 007, India; Email: igu123@gmail.com; Ph: 040 27012799, 272012734	

CONTENTS

Research Articles

1. Prediction of pore pressure and fracture pressure from well log data in a gas hydrate reservoir of the Krishna-Godavari basin
Uma Shankar*, **Shikha Srivastava**, **Dip Kumar Singha** and **Birendra Pratap** **376**
 2. Study of ionospheric precursors of Nepal earthquakes of magnitude $M = 7.8$ and 7.3 occurred on 25 April and 12 May, 2015 using GPS based total electron content (TEC)
Kajal, **Birbal Singh**, and **Devbrat Pundhir*** **387**
 3. Evolution of gas bearing structures in Jaisalmer Basin (Rajasthan), India
Rajesh Pandey*, **Dinesh Kumar**, **A.S. Maurya**, and **Pooja Pandey** **398**
 4. Delineation of groundwater potential zones in hard rock basement terrains of East Godavari district, Andhra Pradesh, India
P. Venkateswara Rao, **M. Subrahmanyam***, and **P. Ramdas** **408**
 5. Structural interpretation and automated extraction of digital terrain model by triangulated irregular network rock mass: A case study from Boboyo (Cameroon)
Jean Jacques Nguimbous-Kouoh*, **Thomas D'Aquin Biyindi**, and **Eliezer Manguelle-Dicoum** **420**
 6. Integration of probabilistic and knowledge driven models for delineating groundwater potential zones: a study on Hinglo river basin, Eastern India
Jagabandhu Roy*, and **Sunil Saha** **435**
 7. Validation of model-based techniques for characterization of surface sediments at Khadakwasala Lake using field Data
Jyoti Sadalage*, **Rashmi Sharma**, **Arnab Das**, and **Yashwant Joshi** **460**
 8. Assessing groundwater potential zones using remote sensing, GIS and MIF techniques: Renigunta area, Andhra Pradesh
E. Balaji*, **G. Veeraswamy**, **A. Narsimha**, **M. Rajasekhar**, and **R. Siddi Raju** **469**
- A Report of the 55th Annual Convention of Indian Geophysical Union (IGU)** **479**

Prediction of pore pressure and fracture pressure from well log data in a gas hydrate reservoir of the Krishna-Godavari basin

Uma Shankar*, Shikha Srivastava, Dip Kumar Singha and Birendra Pratap

Department of Geophysics, Institute of Science, Banaras Hindu University, Varanasi-221005

*Corresponding author: umashankar@bhu.ac.in

ABSTRACT

Pore pressure is the pressure exerted by the fluids within pore space of a reservoir formation while, fracture pressure is the pressure in the wellbore at which formation wall of a wellbore will crack. The detection of over pressure zone is necessary to manage the risks and uncertainties associated with drilling. Pore pressure as well as the fracture pressure affects the well design, such as mud weight profile and casing depth. These parameters in gas hydrate bearing sediments are estimated from sonic logs in two wells (NGHP-01-10A and NGHP-01-03) located in Krishna Godavari (K-G) basin, eastern continental margin of India (ECMI), using various methods such as Eaton's, Bower's and Miller's. After analysing pore pressure estimated from various methods in two wells, pore pressure estimation from Eaton's sonic shows close correspondence to the available pressure core measurements in the selected depth intervals in well NGHP-01-10A. The estimated pore pressure and fracture pressure ranges from 10.05 to 15.21 and 16.61 to 19.29 MPa for well site NGHP-01-10A in the depth range from 1062.05 to 1225.88 m and 12.11 to 14.75 MPa and 16.68 to 20.21 MPa for well site NGHP-01-03 in the depth range from 1140.38 to 1363.80 m. The vertical stress varies from 17.74 to 20.39 MPa in well NGHP-01-10A and 17.94 to 20.91 MPa in well NGHP-01-03 for the whole depth of the logs. The normal pore pressure has been observed in gas hydrate bearing sediments in both the wells. The magnitude of pore pressure slightly increases below bottom simulating reflector (BSR), which may indicate presence of free gas in the study area.

Keywords: Pore pressure and fracture pressure, NGHP wells, K-G basin, Gas hydrate, Eaton method.

INTRODUCTION

The prediction of pore pressure and fracture pressure, is essential in any producing sedimentary basin for safe drilling and design and well construction (Singha et al., 2015; Tingay et al., 2009; Dutta, 2002; Sayers et al., 2002). The pressure exerted by fluid in equilibrium at a given point within the fluid due to the force of gravity is hydrostatic pressure. Abnormally high subsurface pressure exceeding hydrostatic pressure at a given depth is known as overpressure. It can cause serious drilling incidents such as well blowout, pressure kicks if abnormal pore pressure is not accurately predicted before and also during the course of drilling (Dutta, 2002). Similarly, the prediction of fracture

pressure is also necessary for mud designing, cementing, matrix and fracture acidizing, hydraulic fracturing, and fluid injection in secondary recovery (Eaton, 1969; Osborne and Swarbrick, 1997). If the pressure due to mud weight exceeds the fracture pressure, mud loss from the wellbore occurs into the induced fracture during drilling. It is very expensive and troublesome to control loss circulation (Dasgupta et al., 2016).

Gas hydrates are formed from the combination of water and hydrocarbon gases, mainly methane. It is ice-like crystalline solid structure. Gas hydrates are formed at low temperature and highly compressed environment in the continental margins and permafrost region worldwide

(Kvenvolden, 1993). It is considered an unconventional energy resource for the future. Gas hydrate is remotely detected by active seismic method on seismic section by a reflector called bottom simulating reflector (BSR) (Sain et al., 2012). The gas hydrate stability zone (GHSZ) is the depth range within which gas hydrate is present. GHSZ is primarily governed by the water temperature at the seafloor, geothermal gradient, water depth, gas composition, and pore water salinity. The pore pressure and fracture pressure play crucial role in drilling wells in gas hydrate bearing sediments (Singha and Chatterjee, 2014).

The main objective of this paper is to determine the pore pressure and fracture pressure from gas hydrate reservoir in the Krishna-Godavari (K-G) basin at wells NGHP-01-10A and NGHP-01-03. Our purpose is to determine fracture pressure present in the wells to get the idea of selection of maximum mud weight density. We have used different methods for determining the pore pressure and fracture pressure and finally compare the results obtained from these methods.

STUDY AREA

K-G Basin is a peri-cratonic passive margin basin located in central part of eastern continental margin of India (Bastia, 2006). K-G Basin is extensive deltaic plain formed by two large rivers, Krishna and Godavari. It lies in the state of Andhra Pradesh and the adjoining areas of Bay of Bengal. In K-G Basin, there are large number of structures and traps which have been identified for drilling in the on land as well as offshore parts of the basin (Rao, 2001). This basin can be subdivided into three sub basins namely Krishna,

west Godavari, and east Godavari, which are separated by Bapatla and Tanuku horsts respectively (Sastri et al., 1973, 1981). Two rivers, Godavari and Krishna supply the clastic sediments to sea shore initiating deltaic processes (Biswas, 1993). The proven petroliferous K-G Basin has thick layer of sediments deposit with horst and graben system (Gupta, 2006). The deposition in this basin ranges in age from Late Carboniferous to Holocene. In K-G basin, a major delta which has a thick, argillaceous facies that has prograded seaward since the Late Cretaceous, has been a hydrocarbon exploration target (Rao, 2001). It has Cretaceous successions which comprises Raghavapuram (early Cretaceous) and the Tirupati (middle to late Cretaceous) formations. Here, the clastic sedimentary rocks are present which indicates the past environments and also their geodynamic settings (Swarup et al., 2013). In K-G Basin, we have selected two well sites NGHP-01-10A and NGHP-01-03 (Figure 1). Gas hydrate was recovered during NGHP Expedition-01 at site NGHP-01-10A while no gas hydrates at well site NGHP-01-03.

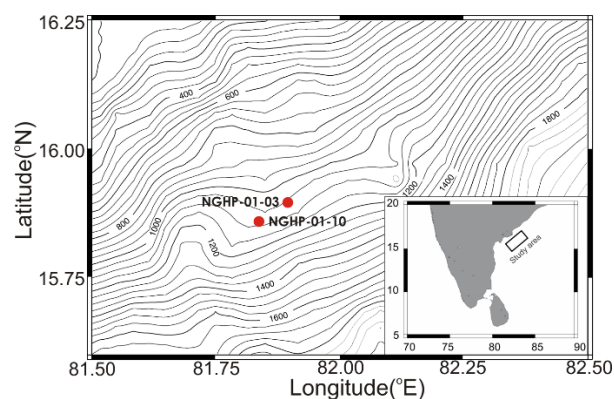


Figure 1. Inset shows the study area location map. Bathymetric map of the K-G basin shown with continuous contour curves targeted during Indian National Gas Hydrate Drilling Expedition-01. The red circles show the drilling site NGHP-01-010A and NGHP-01-03.

METHODOLOGY

An attempt is made to predict pore pressure and fracture pressure of the two well sites selected in K-G Basin. The methodology aims to calculate these two parameters using several methods and various types of log data, such as gamma ray log, density log and sonic log. Figure 2a and b shows the gamma ray log with higher values in GHSZ indicating clay dominated sediments for well site NGHP-01-10A and NGHP-01-03 respectively. Similarly, Figure 3a and b shows neutron porosity log values in gas hydrate sediments with respect to depth from sea surface for well site NGHP-01-10A and NGHP-01-03 respectively. High neutron porosity values indicate the presence of shale

dominated lithology in the study sites. This porosity represents fluid type porosity which gives the total porosity of the formation rock. It is also required to understand the presence of high pressure zone from higher porosity values. Figure 4a and b shows density log value and figure 5a and b show sonic velocity for well site NGHP-01-10A and NGHP-01-03 respectively. BSR marked with dotted line on density and sonic velocity log (Figures 4 and 5). Density and velocity log response from both well indicates presence of free gas below BSR due to sharp decrease of velocity and density (Collett et al., 2008; Lee et al., 2009; Ghosh et al., 2010).

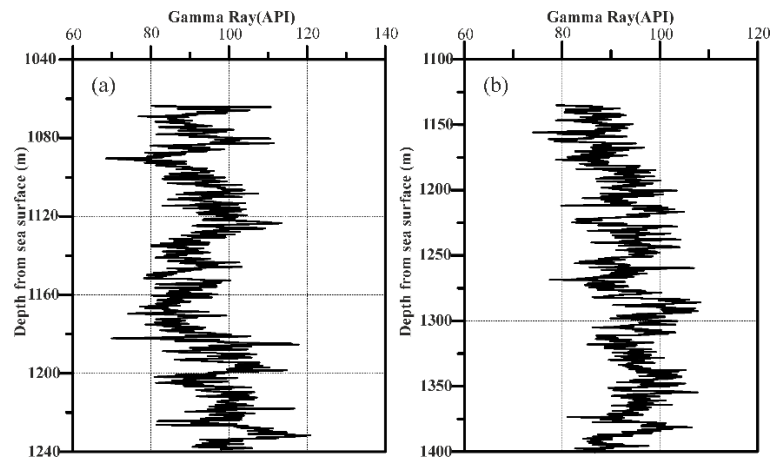


Figure 2. Gamma ray log for (a) well site NGHP-01-10A and (b) well site NGHP-01-03. High gamma ray observed at both wells in clay dominated reservoir. Maximum and minimum value of gamma ray at site NGHP-01-10 is 69 and 116, and at the other site NGHP-01-03, are 74 and 106.

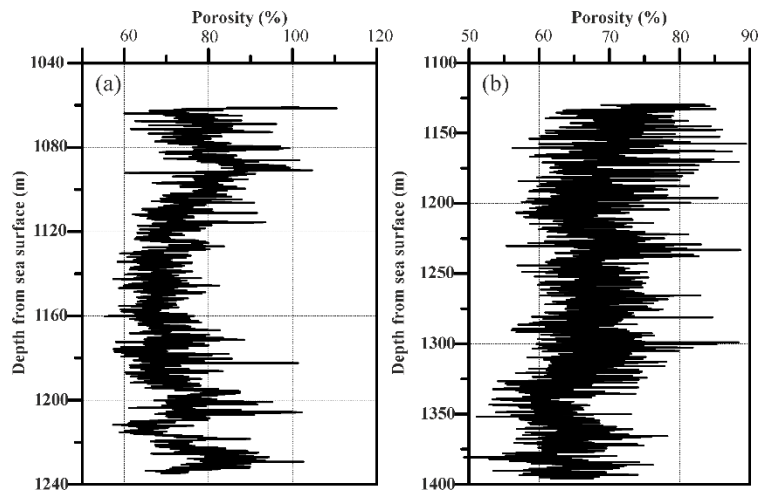


Figure 3. Neutron porosity for (a) well site NGHP-01-10A and (b) well site- NGHP-01-03. High porosity observed at both the well in clay dominated reservoir.

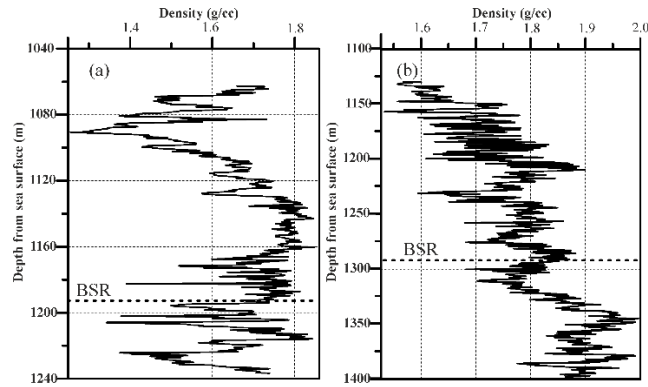


Figure 4. Density log for (a) well site NGHP-01-10A and (b) well site NGHP-01-03. BSR is marked with dotted line.

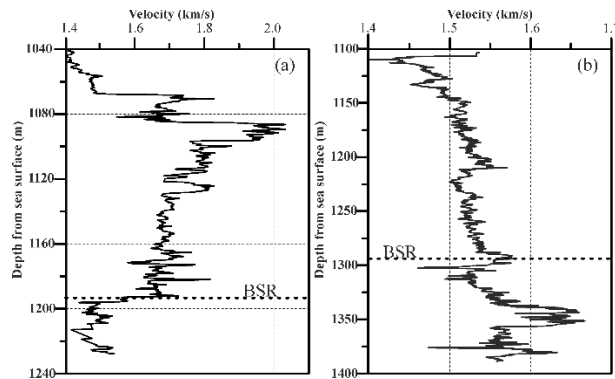


Figure 5. Sonic velocity log for (a) well site NGHP-01-10A and (b) well site NGHP-01-03. BSR is marked with dotted line. Sharp decrease in velocity below BSR indicates presence of free gas below BSR.

Estimation of pore pressure

Estimation of pore pressure is done using Eaton’s method, Bower’s and Millers method. For this, we need to determine the volume of shale as normal compaction trend is valid for shaly sand formation. Volume of shale is calculated using the gamma ray log. The formula used for calculating shale volume in percentage as given below:

$$Volume\ of\ shale = \left(\frac{GR_{log} - GR_{min}}{GR_{max} - GR_{min}} \right) * 100 \dots (1)$$

Shale volume above 45% is considered for further calculation, as we are considering normal compaction trend which is valid for shaly sand formation. Average shale volume is 73% for site NGHP-01-10 and 75% for site NGHP-01-03, as shown in figure 6. Maximum and minimum value of gamma ray at site NGHP-01-10 is 69 and 116 and at site NGHP-01-03 is 74 and 106. In these sites very high shale volume has been calculated

and it shows that reservoir is mostly dominated by shale. Therefore, NCT was drawn for the sonic transit travel time data of the wells as shown in figure 7. The calculation of pore pressure from methods like Eaton’s or Bower’s is possible with some assumptions, but we should have some idea about the geology of the region before applying these method. Eaton’s as well as Bower’s methods consider the fact that overpressure occurs due to some specific mechanism such as disequilibrium compaction generated through burial deposition. Empirical relations between effective stress versus velocity has been established and called as a Bower’s equation to calculate pore pressure from log data. For this purpose, we choose sonic and density log to determine the overpressure generation mechanism and the appropriate pore pressure prediction method (Eaton, 1972; Bower, 1995; Azadpour and Manaman, 2015).

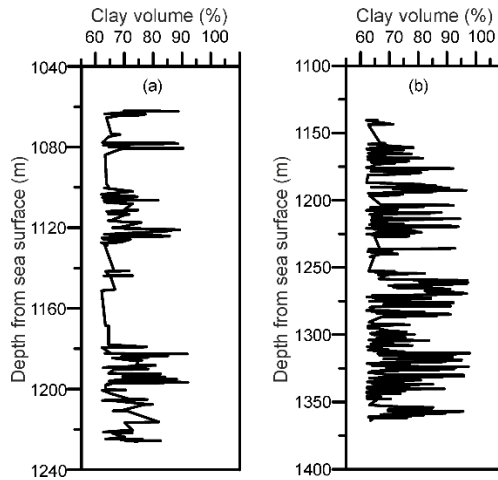


Figure 6. Volume of shale in percentage of (a) well site NGHP-01-10A and (b) well site NGHP-01-03.

The hydrostatic pressure due to the liquid alone at a given depth depends only upon the density of the liquid, the acceleration of gravity and the depth below the surface of the liquid not on the total mass, surface area, or the geometry of the container. The formula used to calculate hydrostatic pressure is

$$P_h = \rho * g * h \dots \dots \dots (2)$$

Here, ρ is the water density and taken equal to 1.03 g/cc, g is acceleration due to gravity and h is the depth of interest of formation.

The overburden pressure at any depth is the pressure which results from the combined

weight of the rock matrix and the fluids in the pore space overlying the formation. Overburden pressure, σ_v , is calculated as given by Plumb et al. (1991).

$$\sigma_v = \int \rho (h) * g dh \dots \dots \dots (3)$$

Where, h is the depth at point of measurement and $\rho(h)$ is bulk density from density log

Normal compaction trend (NCT) line is drawn by fitting linear trend line on sonic log transit time for normal velocity value based on volume of shale. Figure 7a and b shows NCT line for sonic velocity for well site NGHP-01-10A and NGHP-01-03 respectively.

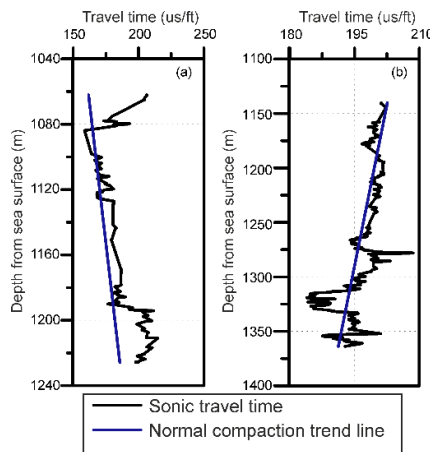


Figure 7. Normal compaction trend (NCT) line for sonic velocity of (a) well site NGHP-01-10A and (b) well site NGHP-01-03.

Pore pressure prediction methods

Several methods and statistical approaches are available for predicting the pore pressure and fracture pressure from log data or other geophysical data. In 1965, Hottman and Johnson studied the pore pressure prediction method using the shale properties derived from well logs. Afterwards, pore pressure prediction was done considering any deviation of measured properties such as velocity, density, resistivity etc from normal trend which is considered as abnormal pressure. Therefore, different logs such as resistivity log, sonic log, density logs are used to predict pore pressure (Eaton, 1972; Miller, 1995; Bower, 1996; Chatterjee and Mukhopdhyay, 2002; Singha and Chatterjee, 2014; Azadpour and Manaman, 2015; Zhang and Yin, 2017). In this study, Eaton's, Bower's and Miller's methods are used to predict pore pressure from various log data.

Eaton's Method

It is one of the most conventional methods used for pore pressure prediction. The basis for calculation of pore pressure by Eaton's method is compaction disequilibrium, which causes overpressure. Eaton gave empirical formulas using resistivity log and sonic log. To apply this method, one needs to determine normal transit time and normal velocity trend using sonic logs and normal resistivity trend from resistivity log (Eaton, 1972; Zhang and Yin; 2017). The NCT represents the optimum linear fitted trend of petrophysical properties such as resistivity, velocity, transit time, density etc. in low permeable zone. To draw the normal compaction trend line, a best fit trend line between a porosity indicator, such as sonic velocity or transit time or resistivity, and normal effective stress is drawn. Using equation 4, initially we have assumed normal hydrostatic

pressure equal to pore pressure for shallow depth in the subsurface. Eaton gave the following formula for pore pressure (PP):

$$pp = \sigma_v - (\sigma_v - Ph) * \left(\frac{\Delta t_n}{\Delta t_{obs}}\right)^x \dots \dots \dots (4)$$

Where, pp is pore pressure gradient, σ_v is overburden gradient, Ph is hydrostatic gradient, Δt_n is normal sonic transit time obtained from NCT, Δt_{obs} is observed sonic transit time from sonic log and x is the exponent value which is dependent on formation properties. Here, x is taken equal to 3 for disequilibrium deposition of sediments (Contreras et al., 2011).

For seismic velocity data, Eaton's method is expressed as:

$$pp = \sigma_v - (\sigma_v - Ph) * \left(\frac{\Delta v_n}{\Delta v_{obs}}\right)^x \dots \dots \dots (5)$$

Where, p is the pore pressure gradient, Δv_{obs} is observed sonic velocity, Δv_n is sonic velocity from NCT, x is the exponent value which is dependent on formation properties. Here, x is taken equal to 3.

Bower's Method

This method used to calculate effective stress from sonic log data. Then, this effective stress is used to calculate pore pressure. Bower's method considers unloading effect due to fluid expansion as the main mechanism of overpressure generations (Azadpour and Manaman, 2015). In compaction disequilibrium conditions, Bowers (1995) proposed an empirically determined method to calculate the effective stress as follows:

$$V = V_o + A\sigma^B \dots \dots \dots (6)$$

where, V is the velocity at a given depth and V_o stands for the surface velocity, σ represents the vertical effective stress; A and B are the parameters obtained from calibrating regional offset velocity versus effective stress data. For no

unloading condition, Bower's introduced the following empirical formula:

$$pp = \sigma_v - \left(\frac{\Delta v_{obs} - \Delta v_{ml}}{a}\right)^{1/b} \dots \dots \dots (7)$$

Where, Δv_{obs} is the observed velocity, Δv_{ml} is the mudline velocity, a and b are the constants. Constant, a is taken equal to 14.2 and b is taken equal to 0.724 (Chris Fletcher, 2016).

Miller's Method

Miller's method (Miller, 1995) gave empirical relation for pore pressure prediction for unloading as well as for no unloading. The physical relationship which is built into the Miller's for no unloading equation is that at zero effective stress, the velocity is the fluid velocity, and as the effective stress approaches infinity, the velocity approaches the matrix. Miller's formula is given as:

$$pp = \sigma_v - \frac{1}{\lambda \left\{ \ln \left(\frac{v_m - v_{ml}}{v_m - v_p} \right) \right\}} \dots \dots \dots (8)$$

Where, v_m is the matrix velocity, v_{ml} is the mudline velocity, v_p is the compressional velocity, λ is the ratio of increase of velocity with stress equal to 0.00025. v_m is taken 1722 m/sec and 1620 m/sec for well site NGHP-01-10A and NGHP-01-03, and v_{ml} is taken 1402 m/sec.

Fracture Pressure Prediction Methods

Fracture pressure can be predicted by several methods including Eaton's and Zhang's methods.

Eaton's method

Eaton used value of Poisson's ratio of formation to calculate fracture pressure. It is based on minimum stress method. It is given as:

$$\sigma_{min} = \frac{\vartheta}{\vartheta - 1} (\sigma_v - pp) + pp \dots \dots \dots (9)$$

Where, σ_{min} is the minimum *in situ* stress or the lower bound of fracture pressure; ϑ is the

Poisson's ratio and its value equal to 0.25. Eaton's equation can be used as lower bound for fracture pressure.

Zhang's method

Zhang introduced that the average of the lower bound and upper bound of fracture pressures can be used as the most likely fracture pressure (Zhang and Yin, 2017). The upper bound fracture pressure given as:

$$P_{fmax} = 2\sigma_h - pp \dots \dots \dots (10)$$

The average of lower and upper bound is given as (Zhang and Yin, 2017):

$$P_{avg} = \frac{3\vartheta}{2(1-\vartheta)} (\sigma_v - pp) + pp \dots \dots \dots (11)$$

Where, P_{avg} is the most likely fracture pressure for formation rock.

Pore Pressure using Eaton's method from sonic log transit time can be estimated with equation 4. Fracture pressure is calculated by Eaton's method and Zhang method from equation 9 and 11 respectively.

RESULTS AND DISCUSSION

Pore pressure using the Eaton's method, Bower's method and miller's method is calculated and plotted with respect to total depth from sea surface for well site NGHP-01-10A and NGHP-01-03 (Figure 8a and b). Pore pressure range is shown in Table 1. By comparing the mud weight used 10.5 ppg (Collett et al., 2008), we find that pore pressure value derived from Eaton's method from sonic log is most appropriate. Bower's method and Miller's method over estimate the pore pressure approximately equal to overburden pressure. The fracture pressure is also calculated using Eaton's method and Zhang's method. The higher value for fracture pressure is found with Eaton's method, while the least value with Zhang's method. The fracture pressure range is shown in Table-2.

Table 1. Range of pore pressure in wells using different methods.

Range of pore pressure (MPa)			
Wells	Eaton's	Bower's	Miller's
NGHP-01-10A	10.05 to 15.21	12.76 to 20.12	17.74 to 20.39
NGHP-01-03	12.11 to 14.75	17.69 to 21.63	17.94 to 21.90

Table 2. Range of fracture pressure in well using different methods.

Range of fracture pressure (MPa)		
Wells	Eaton's	Zhang's
NGHP-01-10A	16.61 to 19.29	14.06 to 17.68
NGHP-01-03	16.68 to 20.21	15.02 to 18.22

Pore pressure and fracture pressure shows a regular trend in well site- NGHP-01-03 but for well site NGHP-01-10A, pore pressure as well as the fracture pressure has sharp increase below depth 1190 m with a difference up to 7 MPa. Fracture can be predicted from resistivity log data. Resistivity increases sharply from its normal trend in well site NGHP-01-10A from 5 ohm-m to 26 ohm-m and then increases up to 65 ohm-m, whereas, for well site NGHP-01-03 resistivity value ranges from 0.75 ohm-m to 1.2 ohm-m. Anomalous resistivity in site NGHP-01-10A due to presence of gas hydrate in fracture clay dominated sediment (Collett et al., 2008; Ghosh et al., 2010; Lee et al., 2009).

Also, it is observed that for fractured zone, pore pressure calculated from Eaton's resistivity formula is negative, while this is not the case with non-fractured zone. The reason behind this is that the normal compaction trend line cannot be determined accurately in fractured zone. Thus, in fractured zone, Eaton's method using the resistivity log data for pore pressure prediction is not valid. We know that the presence of hydrocarbon can be one reason for the abnormal

pressure. The pore pressure is normal pressure in the depth range 1100 to 1190m where gas hydrate is present. We observe slightly high pressure below depth 1190 m in the well site- NGHP-01-10A, i.e., pore pressure increases sharply up to bottom of borehole depth. Sonic velocity log also show sharp decreases in this depth range which satisfies the condition for the presence of free gas. So, there is presence of gas hydrates in the depth range 1100 m to 1190 m in well site NGHP-01-10A (Ghosh et al., 2010; Lee et al., 2009).

Pore pressure increases with decrease in permeability or reduction in porosity (Walder, Nur, 1984). Since, the formation is shaly sand and also decrease in porosity is observed, pore pressure is increasing in deeper depth of both the well sites. The well site NGHP-01-10A is fractured site, slight increase in permeability occurs compared to that of well site NGHP-01-03 which leads to decrease in pore pressure. Since, the well site NGHP-01-10A has gas hydrate reservoir, this decrease in pore pressure is compensated and we observe normal pore pressure value and high pressure value below the hydrate reservoir.

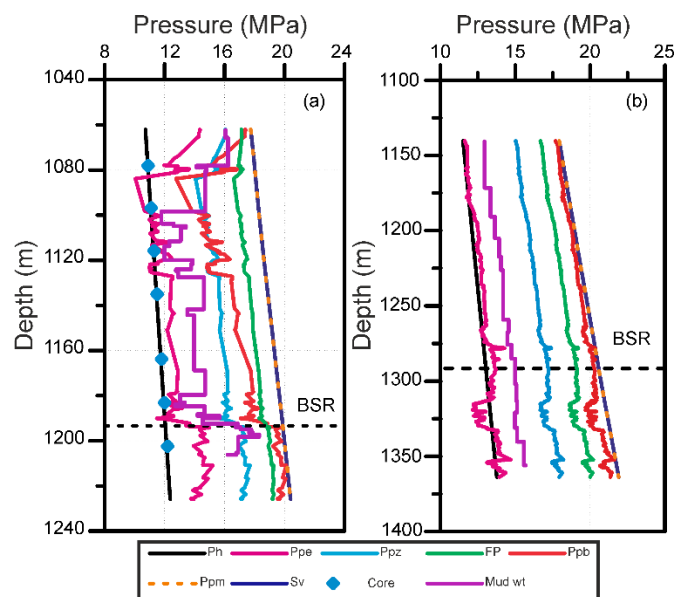


Figure 8. Estimated pore pressure and fracture pressure using different types of methods. Hydrostatic pressure and overburden pressure shown with solid black and blue line respectively. Mud weight shown with purple colour in step. Pore pressure Eaton, Zang and Bower shown with magenta, cyan and red colour curve. Formation pressure shown with green curve and BSR marked with black dotted line. Pore pressure measured from core data shown with square filled with cyan colour for (a) well site NGHP-01-10A and (b) well site NGHP-01-03.

CONCLUSIONS

Pore pressure, fracture pressure and overburden pressure are calculated from the two wells (NGHP-01-10A and NGHP-01-03) in gas hydrate bearing sediments of K-G Basin. Pore pressure is calculated using Eaton's method, Bower's method and Miller's equation and obtained results are compared. Slightly high pore pressures are detected below gas hydrate sediments as departure from NCT line in sonic travel time for two wells in K-G Basin. The gas hydrates are formed in fractured sediments within the stability zone above BSR. The pore pressure maintains normal pressure within gas hydrate reservoir while little high pressure observed below the reservoir indicating presence of free gas. The fracture pressure makes maximum limit for selecting the mud weight during the drillings of the well bore, to keep the borehole well unfracture and optimizing well bore designing.

ACKNOWLEDGEMENTS

We would like to thank DGH for the NGHP Expedition 01 well log data available to us for the research and development of gas hydrate studies in the continental margins of India.

Compliance with Ethical Standards

The authors declare that they have no conflict of interest and adhere to copyright norms.

REFERENCES

- Azadpour, M. and Manaman, N.S., 2015. Determination of Pore Pressure from Sonic Log: a Case Study on One of Iran Carbonate Reservoir Rocks. *Iranian J. Oil and Gas Sci. and Tech.*, 4(3), 37-50.
- Bowers, G.L., 1995. Pore pressure estimation from velocity data: Accounting for overpressure mechanisms besides undercompaction. *SPE Drilling and Completion*, 6, 89-95.

- Collett, T.S., Riedel, M., Cochran, J., Boswell, R., Presley, J., Kumar, P., Sathe, A., Sethi, A., Lall, M. and Sibal, V., 2008. The NGHP Expedition 01 Scientists, National Gas Hydrate Program Expedition 01 Initial Reports, Directorate General of Hydrocarbons, New Delhi.
- Contreras, O.M., Tutuncu, A.N., Aguilera, R.M., and Hareland, G.M., 2011. A case study for pore pressure prediction in an abnormally sub-pressured western Canada sedimentary Basin, in 45th US Rock Mechanics/Geomechanics Symposium.
- Eaton, B.A., 1969. Fracture gradient prediction and its application in oilfield operations. Paper SPE2163: JPT, 25-32.
- Eaton, B. A., 1972. Graphical method predicts pressure worldwide. *World Oil*, 182, 51-56.
- Chatterjee, R. and Mukhopdhyay, M., 2002. In-situ stress determination using well log data for the oil fields of the Krishna-Godavari basin. *Petrophysics*, 43, 26-27.
- Dasgupta, S., Chatterjee, R. and Mohanty, S.P., 2016. Prediction pore pressure and fracture pressure in Cauvery, Krishna-Godavari basin, India. *Marine and Petrol. Geol.*, 78, 493-506.
- Dutta, N.C., 2002. Geopressure prediction using seismic data: Current status and the road ahead. *Geophysics*, 67(6), 2012-2041.
- Ghosh, R., Sain, K. and Ojha, M., 2010. Effective medium modeling of gas hydrate filled fractures using the sonic log in the Krishna Godavari basin, offshore eastern India. *J. Geophys. Res.*, 115, 1-15.
- Gupta, S. K., 2006. Basin architecture and petroleum system of Krishna Godavari Basin, east coast of India. *The Leading Edge*, 25(7), 830-837.
- Kvenvolden, K.A., 1993. Gas hydrates—geological perspective and global change. *Rev Geophysics*, 31, 173-187.
- Lee, M.W. and Collect, T., 2009. Gas hydrate saturations estimated from fractured reservoir at Site NGHP-01-10, Krishna-Godavari Basin, India. *J. Geophys. Res.*, 114, 1-13.
- Miller, T.W., 1995. New insights on natural hydraulic fractures induced by abnormally high pressure. *AAPG Bulletin*, 79, 1005-1018.
- Plumb, R.A., Evans, K.F. and Engelder, T., 1991. Geophysical log responses and their correlation with bed-to-bed stress contrasts in Paleozoic rocks, Appalachian plateau, New York. *J. Geophys. Res.*, 96(B9), 14509-14528.
- Rao, G.N., 2001. Sedimentation, Stratigraphy and Petroleum Potential of Krishna-Godavari Basin, East Coast of India. *AAPG Bulletin*, 85(9), 1623-1643.
- Sain, K., Ojha, M., Satyavani, N., Rammadas, G.A., Ramaprasad, T., Das, S.K. and Gupta, H., 2012. Gas-hydrates in Krishna-Godavari and Mahanadi basins: New data. *J. Geol. Soc. India*, 79, 553-556.
- Sastri, V.V., Venkatachala, B.S. and Narayanan, V., 1981. The evolution of the east coast of India. *Paleogeogr. Paleoclimatol. Paleoecol.*, 36, 23-54.
- Sastri, V.V., Sinha, R.N., Singh, G. and Murti, K.V.S., 1973. Stratigraphy and tectonics of sedimentary basins on the East coast of peninsular India. *AAPG Bulletin*, 57, 655-678.
- Sayers, C.M., Johnson, G.M. and Denyer, G., 2002. Predrill pore-pressure prediction using seismic data. *Geophysics*, 67, 1286-1292.
- Singha, D.K. and Chatterjee, R., 2014. Detection of overpressure zones and a statistical model for pore pressure estimation from well logs in the Krishna–Godavari Basin, India. *Geoche. Geophys. Geosys.* 15(4), 1009-1020.
- Singha, D.K., Chatterjee, R., Sen, M.K. and Sain, K., 2015. Pore pressure prediction in gas hydrate bearing sediments of Krishna-Godavari Basin in India. *Marine Geology*, 357, 1-11.

Swarup, V., Kumar, T. and Kumar, N., 2013. Mineralogy and Petrology of the Krishna Godavari Basin on Shore Area, East Coast of India. *Int. J. Sci. and Res.*, 2319-7064.

Tingay, M.R.P., Hillis, R.R., Swarbrick, R.E., Morley, C.K., and Damit, A.R., 2009. Origin of overpressure and pore-pressure prediction in the Baram province, Brunei. *AAPG Bull.*, 93, 51-74.

Walder, J. and Nur, A., 1984. Porosity Reduction and Crustal Pore Pressure Development. *J. Geophys. Res.*, 89(13), 11539-11548.

Zhang, J. and Shang-Xian Yin, 2017. Fracture gradient prediction: an overview and an improved method. *Petroleum Sci.*, 14(4), 720-730.

Received on: 30.4.19; Revised on: 5.7.19; Accepted on: 5.8.19

Study of ionospheric precursors of Nepal earthquakes of magnitude $M = 7.8$ and 7.3 occurred on 25 April and 12 May, 2015 using GPS based total electron content (TEC)

Kajal¹, Birbal Singh¹, and Devbrat Pundhir^{2*}

¹Department of Electronics and Communication Engineering, Raja Balwant Singh Engineering Technical Campus, Bichpuri, Agra, India-283105

²Department of Physics, Raja Balwant Singh Engineering Technical Campus, Bichpuri, Agra, India-283105

*Corresponding author: devbratpundhir@gmail.com

ABSTRACT

The Global positioning system (GPS) based total electron content (TEC) variations of two Nepal earthquakes, which took place in 2015, were analyzed using a quartile based statistical technique with the aim to detect possible ionospheric anomalies associated with these seismic events and describe their main features. The effect of these earthquakes has been examined over three International GNSS Services (IGS) stations, one of which is Lucknow (Lck3) located in India, whereas others like Lhasa (Lhaz) and Wuhan (Wuhn), are located in China, all within 800 km from epicenters of two earthquakes except Wuhan, which is located at about 2865 km. The enhancements and depletions in TEC data are found prior to these earthquakes. The analysis indicate that TEC data show anomalies within 8-15 days prior to the earthquake of 25 April 2015 and the same occur within 5-7 days prior to the earthquake of 12 May of 2015. The TEC perturbations due to earthquakes may be interpreted in terms of $E \times B$ drift generated by seismic associated electric field.

Keywords: TEC, Magnetic storms, Nepal earthquakes, Acoustic gravity waves, Ionospheric precursors.

INTRODUCTION

Earthquakes and tsunami are two natural calamities for which no full proof prediction technique is developed yet, even though several workers have been working hard on seismo-electromagnetic technique to predict the earthquakes a few days before its main occurrence to save the life and properties. Davies and Baker (1965) were the first to identify the ionospheric perturbations due to Alaska earthquake of 28 March, 1964. Seismo-ionospheric effect's extended discussion was given by Lipervosky et al. (1992). Availability of GPS-TEC data now provide enhanced opportunities in identifying ionospheric precursors to scientists working in this area (Calais and Minster, 1995; Liu et al., 2004 b; Devi et al., 2004, 2010, 2012; Xia et al., 2011; Klimenko et al., 2011, 2012). The scientists have done statistical as well as case studies from the GPS data (Liu et al., 2001, 2004a,b, 2006, 2009, 2010, 2011; Le et al., 2011; Naaman et al., 2001; DasGupta et al., 2006; Dabas et al., 2007; Karia

and Pathak, 2011; Akhoondzadeh, 2012; Lin, 2012; Pundhir et al., 2014) and reported encouraging results. The Chi-Chi earthquake ($M=7.7$) of 21 September 1999 has been studied thoroughly by Liu et al. (2001), who observed the precursors 1-5 days before the earthquake occurrence and TEC decreases significantly around the epicenter in the afternoons of these days.

Similarly, Liu et al. (2011) using global ionospheric map (GIM-TEC), studied the effect of 736 earthquakes ($M<6.0$) that occurred during 2002-2012 and found anomalies few days before the earthquakes. Liu et al. (2009) have reported TEC reductions, 3-5 days prior to the occurrence of 17 earthquakes of magnitudes $M \geq 6.3$ in China region for the duration of 10 years from 1998 – 2008. They have also presented the results of a case study of Wenchuan earthquake of magnitude $M = 7.9$ in the year of 2008 and found the increase in TEC data in afternoon, 3 days prior to the main shock. Recently, Le et al. (2011) have further

examined the effect of 736 earthquakes of magnitudes $M \geq 6$ on GPS-TEC data for years 2002 to 2006 and shown that the occurrence rate of anomaly within several days before the earthquakes is than that during the background days, especially in case of large magnitude and low depth earthquakes. The long term precursors (9-19 days prior to the main shock) have also been found by Ho et al. (2013). However, in many cases, it is very difficult to find out the cause of ionospheric variations, because there are many reasons such as dust storms, nuclear explosions, volcanic eruptions, and lightning etc. which can be associated with the ionospheric perturbations (Pulinets and Davidenko, 2014).

Apart from the above, the strong earthquake of Tohoku ($M=9.1$) of 11 March 2011 was also studied by Akhoondzadeh (2012), who reported precursors 1-3 days prior to occurrence of the earthquakes. The Pakistan-Iran border earthquake of was further studied by Pundhir et al. (2014) by analyzing GPS-TEC data recorded at Agra station, who reported precursory period of 1-9 days prior to main event. Many attempts have thus been made, to identify the convincing precursors of the earthquakes and the results can be broadly divided into two categories of the periods 1-5 days depending on magnitude of the earthquakes (Liu et al., 2000, 2002, 2004a, 2009; Pulinets et al., 2005, 2010; Zakharenkova et al., 2007; Hasbi et al., 2011; Kon et al., 2011; Pulinets and Davidenko, 2014), and also in the range of 9-19 days in some other cases (Ho et al., 2013; Pundhir et al., 2017).

In the present paper, an attempt has been made to identify the precursors of the two largest earthquakes of Nepal $M = 7.8$ (Lat. 28.33°N , Long. 84.73°E) on 25 April and $M = 7.3$ (Lat. 27.7°N , Long. 86.0°E) on 12 May, 2015, using GPS-TEC data of three International GNSS Services (IGS) stations, one of which is Lucknow

(Lck3, Lat. 26.9°N , Long. 80.9°E), located in India, whereas others Lhasa (Lhaz, Lat. 29.6°N , Long. 91.1°E) and Wuhan (Wuhn, Lat. 30.5°N , Long. 114.3°E) are located in China, all within 800 km from epicenters of two earthquakes except Wuhan which is located at about 2865 km. The ionospheric data (GPS-TEC) for these months are not available at Agra station due to equipment failure.

Sources of Data

The earthquake data are taken from United State Geological Survey (USGS) website: <http://earthquake.usgs.gov/earthquakes/>. The details of earthquakes considered for this study are shown in Table 1 and their locations are shown in Figure 1 by solid star and of the IGS station by solid circles. As mentioned earlier, the ionospheric data (GPS-TEC) for these months are not available in Agra station due to equipment failure so the IGS stations TEC data are obtained from the Scripps Orbit and Permanent Array Center (SOPAC) and California Spatial Reference Center (CSRC) through the website of <http://geofit01.ucsd.edu/pub/rinex/>.

The ΣK_p is the sum of the K_p indices of the whole day ($\Sigma K_p \geq 30$ indicates the disturbed day). The Dst index reflects the dynamics of magnetospheric ring current, but at the same time the current is one of the sources of global magnetic field variations. Both the K_p and Dst are likely to be good indicator of magnetic activity at low and middle latitudes. Their values are taken from the website:

<http://omniweb.gsfc.nasa.gov/form/dx1.html>.

The solar radio flux at F10.7 (2800MHz) is an excellent indicator of solar activity, often called as F10.7 index. The F10.7 index data are taken from the website (<http://omniweb.gsfc.nasa.gov/form/dx1.html>).

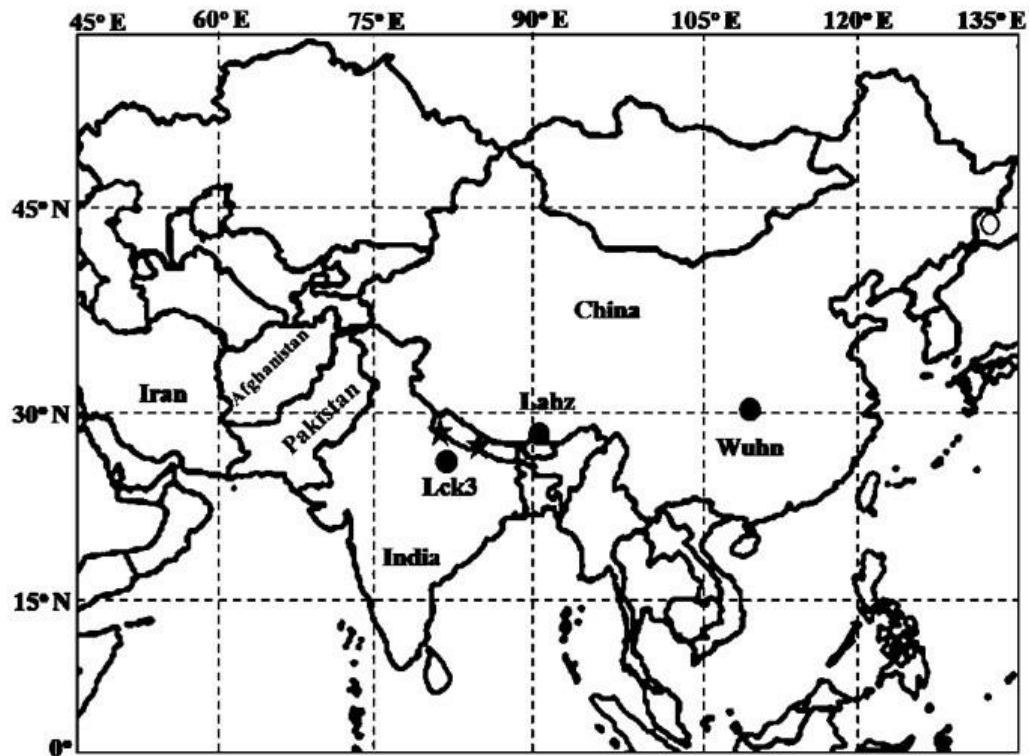


Figure 1. Map of India and surrounding regions, where locations of the two earthquakes are shown by solid star and of IGS stations by solid circles.

Methods of GPS-TEC Data Processing

A quartile based data processing technique is adopted. This statistical technique was adopted by other workers also (Liu et al., 2009 and Pundhir et al., 2014, 2017). In this technique, we initially calculate a moving median (M) of every successive 15 days GPS-TEC data is calculated initially and then the deviation between observed TEC data and median is found for the 16th day. Then upper and lower quartiles (UQ and LQ) are determined. For a normal distribution having mean (m) and standard deviation (σ), the median (M) is approximately equivalent to mean (m) and LQ or UQ is equivalent to 1.34σ (Klotz and Johnson, 1983). Under this criteria, the lower and upper bounds in the variation of data may be written as $LB = M - 1.5(M - LQ)$ and $UB = M + 1.5(UQ - M)$, and thus calculated accordingly. For the day to be considered anomalous, GPS-

TEC values should be more or less to the associated UB and LB on that particular day.

RESULTS AND DISCUSSIONS

The characteristics of the two powerful earthquakes of magnitude $M = 7.8$ and 7.3 that occurred in Nepal on 25 April and 12 May, 2015 are shown in Table 1. The table shows days of occurrence, location in latitude and longitude, magnitude and depth whereas, the last column shows the radius of influence zone in which the effect of such earthquake may be experienced determined from Dobrovolsky et al. (1979)'s relation ($R = 10^{0.43M}$, where M is magnitude of earthquake). The Table 2 shows the distances of the two earthquakes from the three IGS stations. The days of ionospheric precursors observed are also shown in Table 2 for the analyzed earthquakes.

Table 1. List of earthquakes and their characteristics

S. No.	Date of earthquake	Time (UT)	Lat. (deg.)	Long. (deg.)	Depth (km)	Mag.	Region	Radius of the influence zone (kms)
1	12.5.2015	07:05:19	27.7	86	15	7.3	19 km SE of Kodari, Nepal	1377.20
2	25.4.2015	06:11:25	28.33	84.73	8.22	7.8	36km E of Khudi, Nepal	2259.43

Table 2. Details of the earthquakes distances from the IGS stations considered for the determination of ionospheric perturbation.

S. No.	Mag. of earthquake	Earthquake distances from the observing station			
		Lhasa (kms)	Lucknow (kms)	Wuhan (kms)	Precursory Period
1	7.3	540.6	511.7	2760	6-7
2	7.8	635.5	409.5	2866	23-19

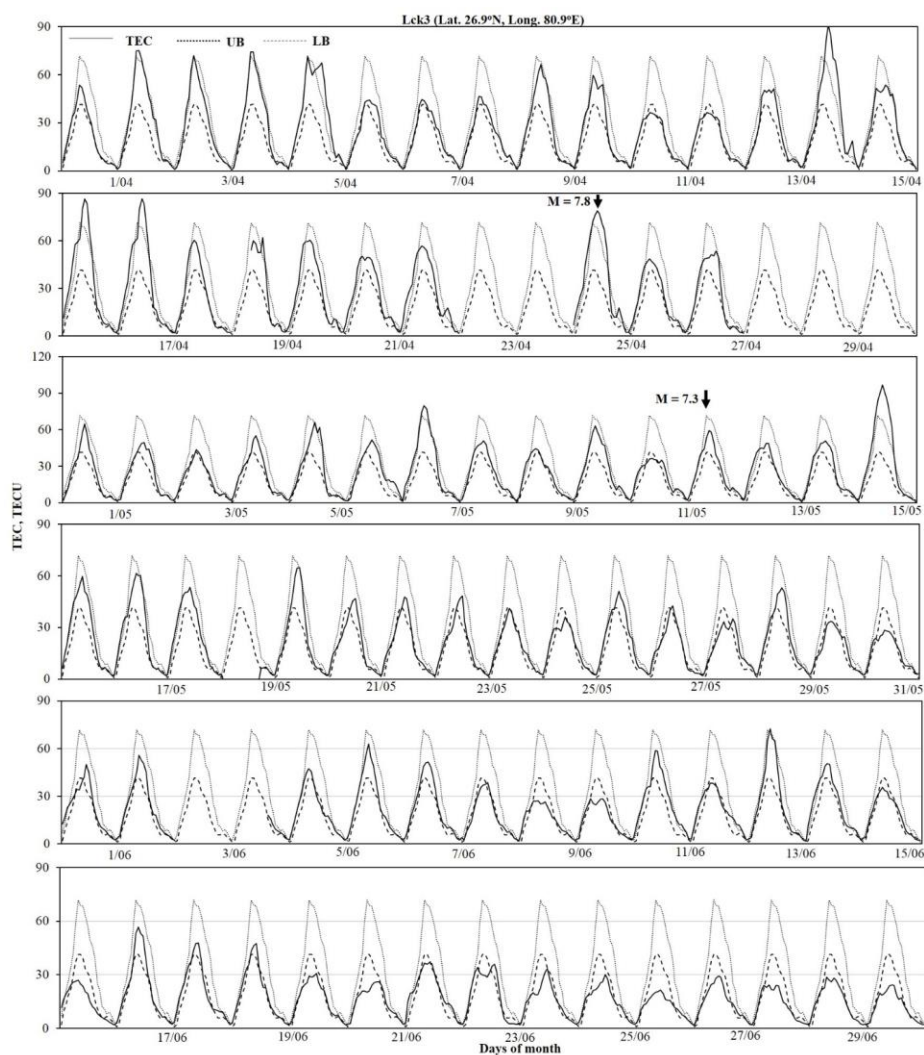


Figure 2. Diurnal variation of GPS-TEC data of Lucknow station for the earthquakes of magnitude M=7.8 and M= 7.3, for the duration of three months from 1 April to 30 June, 2015. Arrow (\uparrow) indicate the days of earthquakes.

The diurnal variations of the GPS-TEC data for a period of three months April, May and June, 2015 over Lucknow and Lhasa station and two months of April and May, 2015 over Wuhan station (the data for the month of June is not available over Wuhan) are shown in Figures 2,3,4. The Figure 5 shows the variation of $\sum Kp$ (solid histograms) and Dst (dotted line) and solar radio flux F10.7 (blank histograms) during the three months under consideration. The upper and lower bounds are shown by the dotted and dashed lines respectively, whereas diurnal variation is shown by the solid line. The downward arrows show the days of the two earthquakes in the months of April and May in each figure respectively. The variation of GPS-TEC data over Lucknow station (Lck3) shows significant enhancements on 2, 3, 4, 5, 14, 16, 17, 19, 20, 21, 22 April, 2015 before the earthquakes of M=7.8 occurred on 25 April, 2015. However, moderate magnetic storms occurred on 10 April ($\sum Kp=40$) and on other days like 15 ($\sum Kp=37$), 16 ($\sum Kp=47$), 17 ($\sum Kp=33$) and 21 ($\sum Kp=37$) April, 2015. Hence, anomalies occurring on 14 to 22 April, 2015, may not be clearly identified as due to earthquake, except that occurring on 2,3,4,5 April which occurred before the magnetic storms. This may be due to earthquake effect showing a precursory period of about 23-20 days. Similarly, for the earthquake of M=7.3 in the month of May, 2015, the significant enhancements can be seen on 5, 6, 7, 8, 9, 10, 11 May, 2015. However, a moderate magnetic storms occurred on 6 May ($\sum Kp=33$) and 13 May ($\sum Kp=50$), 2015. Here also 6-11 May, 2015 cannot be attributed entirely due to the earthquake occurring on 12 May 2015, because of magnetic storms of 6 May, 2015. Of course the anomaly of 5 May remains unaffected by magnetic storm and may be considered as precursor of the earthquake occurring 7 days before the main shock

In the GPS-TEC data of Lhasa station (Lahz) the TEC enhancements are identified on 2, 3, 9, 14, 17, 22, 23, 24 April, 2015. As mentioned above, anomalies occurring on 14 to 24 April may not be clearly identified as due to earthquake except that occurring on 2,3,9 April which occurred before the magnetic storms. This may be due to earthquake effect showing a precursory period of about 23-17 days. Similarly, 5, 6, 7, 8, 9, 10, 11 May, 2015, the anomalous variation cannot be attributed entirely due to the earthquake because of magnetic storms of 6 May, 2015. However, the anomaly of 5 May, 2015, may be considered as precursor of the earthquake occurring on 12 May 2015 occurring 7 days before the main shock.

In a similar manner, anomalous variation can be seen at Wuhan station (Wuhn) on 3, 4, 6, 7, 15, 11 April 2015, but due to occurrence of moderate magnetic storms, these anomalies cannot be clearly identified due to the earthquake of 25 April, 2015 but the anomalies of 3,4,6,7 April, 2015 can be clearly stated due to the largest earthquakes, showing a precursory period of 23-19 days before the main shock. Similarly for the earthquake of M = 7.3 in the month of May, 2015, the anomalous variation can be seen on 5, 6, 7, 8, 9, 10, 11 May, 2015. Here, the anomalies on 6-12 May, 2015 cannot be attributed entirely due to the earthquake occurring on 12 May 2015 because of magnetic storms of 6 May, 2015, but the anomaly of 5 May remain unaffected by magnetic storm and may be considered as precursor of the earthquake occurring 7 days before the main shock. There are no significant changes observed in TEC data over these three stations during the month of June, 2015. The solar flux have also been plotted for the period under consideration but its values lies between 100-150 sfu throughout the period, except one enhanced value (≈ 255 sfu) on 22 June.

There is no drastic change in solar flux value during this period. Hence, it may not affect the TEC data. Pundhir et al. (2017) reported the similar condition that the solar flux values lie in

the range of 100-150 sfu during the precursory period of earthquake magnitude $M = 7.8$ occurred on 16 April, 2013.

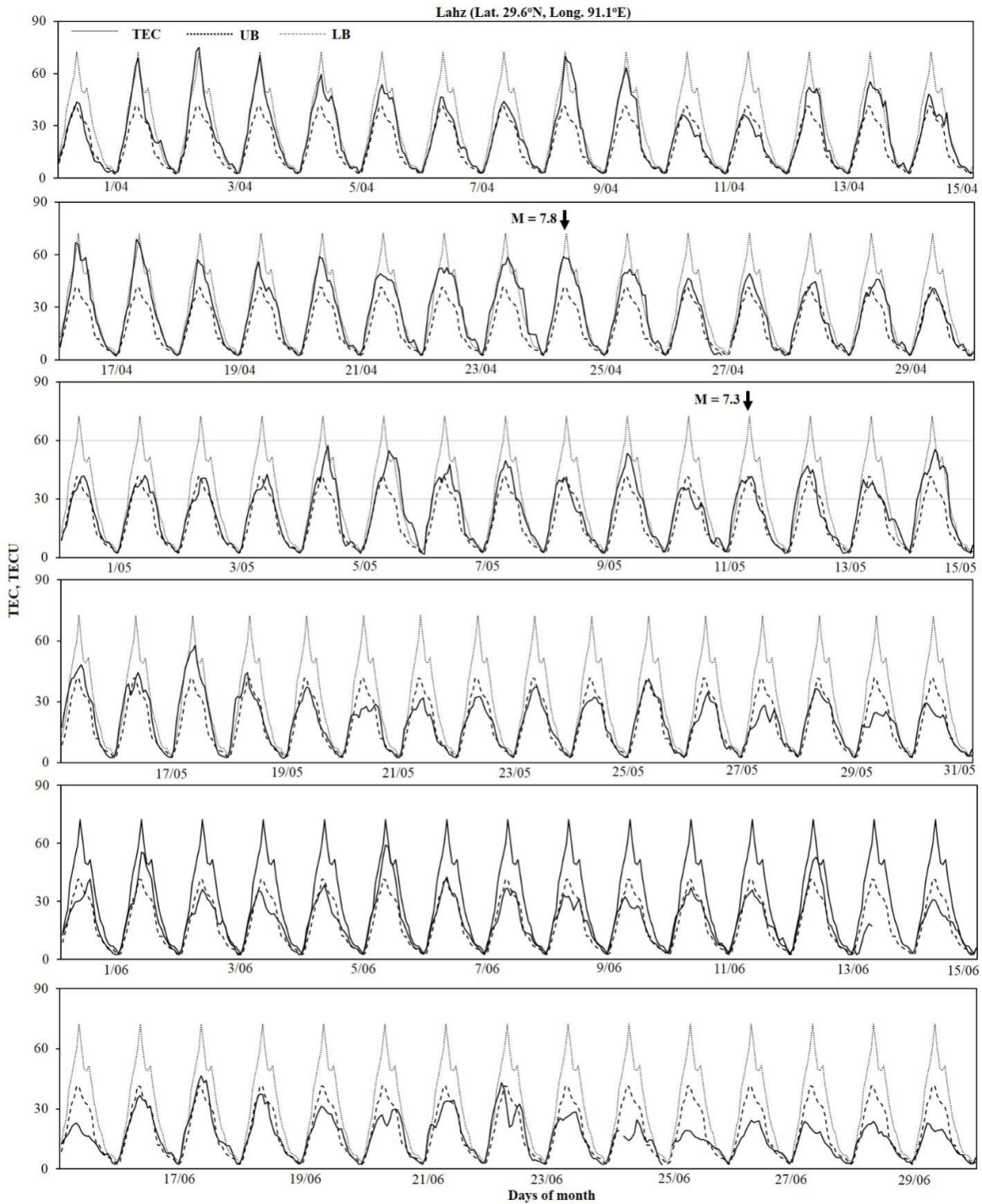


Figure 3. Diurnal variation of GPS-TEC data for Lhasa station. All other details are same as the Figure 2.

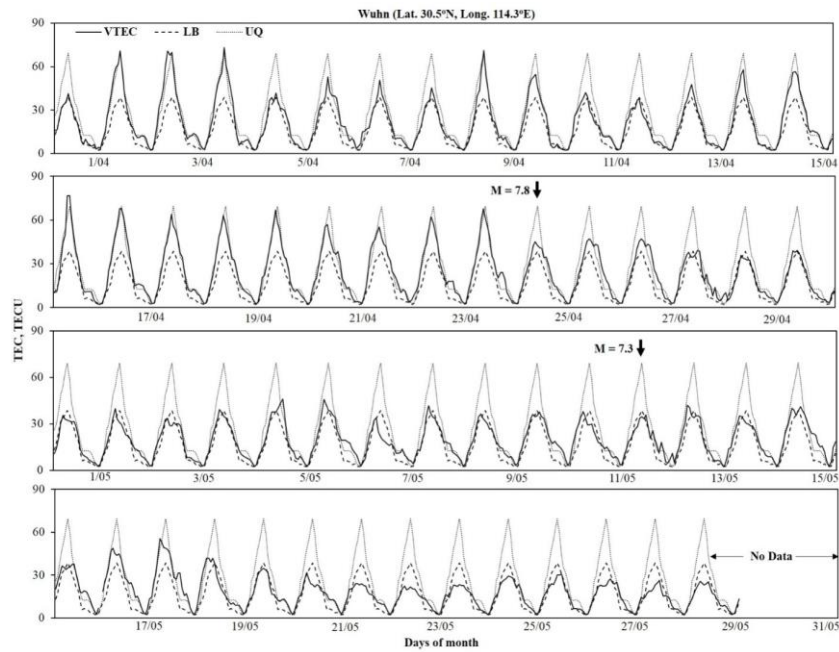


Figure 4. Diurnal variation of GPS-TEC data for the Wuhan station for two months 1 April to 31 May, 2015. The data for the month of June, 2013 are not available. Other details are same as Figures 2 and 3.

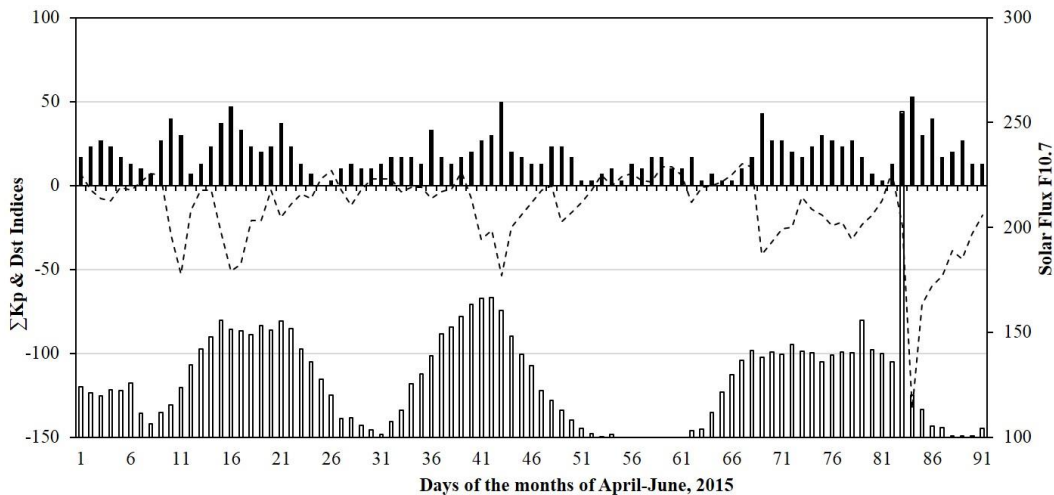


Figure 5. The variation of magnetic activity and solar flux parameters for the period of 3 months between 1 April and 30 June 2015.

The perturbations in TEC data are explained by using well-established mechanisms as suggested by earlier workers (Pulinets and Davidenko, 2014; Devi et al., 2004, Pundhir et al., 2014). Briefly, there are several mechanisms are approved for the ionospheric perturbations. However there is a growing consensus that it is due to $E \times B$ drift mechanism, where the electric field (E) triggered

by an earthquake preparatory process, penetrates the ionosphere and, in the presence of local magnetic field (B), causes upward or downward movement of the ionization depending upon the direction of the electric field. Then, the question remains about the mechanism of the electric field generation from the earthquake region. The radon emissions arise from epicenter, and ionize the near

earth atmosphere over the seismic zones. The formation of quasi-neutral ion clusters which are destroyed by the air motion caused by acoustic gravity waves generated by accumulation of greenhouse gases over the seismic region. The breaking of ion clusters makes the near ground layer of the atmosphere rich in ion (concentration $\sim 10^5 - 10^6 \text{ cm}^{-3}$). The charge separation process leads to generation of anomalously strong vertical electric field ($\sim 1 \text{ KVm}^{-1}$), in comparison with the fair weather electric field ($\approx 100 \text{ Vm}^{-1}$). This anomalous electric field penetrates up to ionosphere. The TEC increases or decreases during the earthquakes preparatory process, depends upon the direction of the electric field. This process is describes in Figure 6. As per our understanding, magnitude of the earthquake increases, fault length also increases. The energy release from the lithosphere is directly proportional to the magnitude of the earthquake. If magnitude increases, the release of energy also increases and vice-versa. Here, it may be concluded that due to large magnitude earthquake, huge amount of energy is released as a result of

strong electric filed is build up which penetrate up to the ionosphere. Singh et al. (2004) have shown that how much electric reaches to the ionosphere through atmosphere and lithosphere by using the data of borehole antenna as well as theoretical modeling. The establishment of any mechanism is out of the scope of paper.

Another possible mechanism i.e. generation of atmospheric gravity waves from the epicentral region due to the oscillations of local atmospheric temperature and pressure variations. These waves propagate from the atmosphere to ionosphere and affect the TEC data largely. As mentioned earlier, (Akhoondzadeh, 2012) shown that precursory period is 1-3 days before the earthquake of $M = 9.1$, but in our case ($M = 7.4$ and 7.8) it is quietly large may be due to the generation of atmospheric gravity waves from the epicenter area. The atmospheric gravity generated from the epicenter area many days prior to the earthquakes and penetrates up to the ionosphere in obliquely direction so they travel to long distance and affect largely far away from the epicenter (Pundhir et al., 2018).

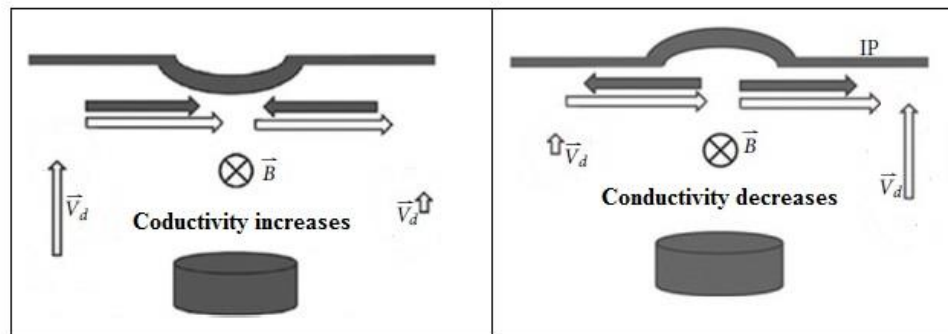


Figure 6. Schematic representation of atmosphere-ionosphere coupling through the global electric circuit (GEC). The left panel shows the condition of increased air conductivity and right panel shows the condition of decreased air conductivity.

CONCLUSIONS

We have analyzed the GPS-TEC data obtained from three International GNSS Services (IGS) stations, one of which Lucknow (Lck3, Lat. 26.9°N , Long. 80.9°E) located in India whereas others Lhasa (Lhaz, Lat. 29.6°N , Long. 91.1°E)

and Wuhan (Wuhn, Lat. 30.5°N , Long. 114.3°E) are located in China, for the analysis of two largest earthquakes of magnitude $M = 7.8$ (Lat. 28.33°N , Long. 84.73°E) and 7.3 (Lat. 27.7°N , Long. 86.0°E) occurred in Nepal on 25 April and 12 May, 2015 respectively. We observed that the

precursory period for $M=7.8$ is 23-19 days before the occurrence of the earthquake and 7-6 days for the earthquake of $M=7.3$ at all three stations. This study is very important in the context of large magnitude earthquakes and how these earthquakes affect the epicenter as well as adjoin region. It proves that large earthquakes affect not only in epicenter region but also in adjoin region.

ACKNOWLEDGEMENT

The authors are highly thankful to the Ministry of Earth Sciences, Government of India, and New Delhi for extending financial support to this research in the form of a major research project. Thanks are also due to Dr. Dushyant Singh, Head, Department of Electronics and Communication engineering for providing facilities for research and to Mr. Ajay Singh for help with the figures.

Compliance with Ethical Standards

The authors declare that they have no conflict of interest and adhere to copyright norms.

REFERENCES

- Akhoondzadeh, M., 2012. Anomalous TEC variations associated with the powerful Tohoku earthquake of 11 March 2011. *Nat. Hazards Earth Syst. Sci.*, 12, 1453-1462.
- Calais, E. and Minster, J.B., 1995. GPS detection of ionospheric perturbations following the January 17, 1994, Northridge earthquake. *Geophys. Res. Lett.*, 22(9), 1045-1048.
- Dabas, R.S., Das, R.M., Sharma, K. and Pillai, K.G.M., 2007. Ionospheric pre-cursors observed over low latitudes during some of the recent major earthquakes. *J. Atmos. Solar Terr. Phys.* 69(15), 1813-1824.
- DasGupta, A., Das, A., Hui, D., Bandyopadhyay, K.K. and Sivaraman, M.R., 2006. Ionospheric perturbations observed by the GPS following the December 26th 2004 Sumatra-Andaman earthquake. *Earth Planets Space (Japan)*, 58, 167-172.
- Davies, G.K. and Baker, D.M., 1965. Ionospheric effects observed round the time of Alaska earthquake of March 28, 1964. *J. Geophys. Res.*, 70(9), 2251-2263.
- Devi, M., Barbara, A.K. and Depueva, A., 2004. Association of total electron content (TEC) and f_oF_2 variations with earthquake events at the anomaly crest region. *Ann. Geophys.*, 47(1), 1-9.
- Devi, M., Barbara, A.K., Depueva, A.H., Ruzhin, Y.Y. and Depueva, V., 2010. Anomalous total electron content (TEC) and atmospheric refractivity prior to the very strong China earthquake of May 2008. *Int. J. Remote Sens.*, 31, 3589-3599.
- Devi, M., Sharma, A.J.D., Kalita, S., Barbara, A.K. and Depueva, A., 2012. Adaptive techniques for extraction of pre-seismic parameters of Total electron content (TEC) at the anomaly crest station. *Geomat. Nat. Hazards Risk*, 3, 193-206.
- Dobrovolsky, I.P., Zubkov, S.I. and Miachkin, V.I., 1979. Estimation of the size of earthquake preparation zones. *Pure Appl. Geophys.*, 117, 1025-1044.
- Hasbi, A.M., Ali, M.A.M. and Misran, N., 2011. Ionospheric variations before some large earthquakes over Sumatra. *Nat. Hazards Earth Syst. Sci.*, 11, 597-611.
- Ho, Y.Y., Jhuang, H.K., Su, Y.C. and Liu, J.Y., 2013. Seismo-ionospheric anomalies in total electron content of the GIM and electron density of DEMETER before the 27 February 2010 M 8.8 Chile earthquake. *Adv. Space Res.*, 51, 2309-2315.
- Karia, S.P. and Pathak, K.N., 2011. Change in refractivity of the atmosphere and large variation in TEC associated with some earthquakes,

- observed from GPS receiver. *Adv. Space Res.*, 47(1), 867-876.
- Klimenko, M.V., Klimenko, V.V., Zakharenkova, I.E., Pulinets, S.A., Zhao, B. and Tsidilina, M.N., 2011. Formation mechanism of great positive TEC disturbances prior to Wenchuan earthquake on May 12, 2008. *Adv. Space Res.*, 48, 488-499.
- Klimenko, M.V., Klimenko, V.V., Zakharenkova, I.E. and Pulinets, S.A., 2012. Variations of equatorial electrojet as possible seismo-ionospheric precursors at the occurrence of TEC anomalies before strong earthquakes. *Adv. Space Res.* 49, 509-517.
- Klotz, S. and Johnson, N.L. (Eds.), 1983. *Encyclopedia of Statistical Sciences*. John Wiley and Sons, New York City, United States.
- Kon, S., Nishihashi, M. and Hattori, K., 2011. Ionospheric anomalies possibly associated with $M \geq 6.0$ earthquakes in the Japan area during 1998-2010: Cases studies and statistical study. *J. Asian Earth Sci.*, 41, 410-420.
- Le, H., Liu, J.Y. and Liu, L., 2011. A statistical analysis of ionospheric anomalies before 736 $M=6.0+$ earthquakes during 2002-2010. *J. Geophys. Res.*, 116(A02303), 1-5.
- Lipervosky, V.A., Pokhotelov, O.A. and Shalimov, S.L., 1992. *Ionospheric precursors of earthquakes*. Mezhdunarodnaya Nauka Moscow, 304.
- Lin, J.W., 2012. Nonlinear principal components analysis in the detection of ionospheric electron content anomalies related to a deep earthquake (>300 km, $M 7.0$) on 1 January 2012, Izu Islands, Japan. *J. Geophys. Res.*, 117(A06314), 1-15.
- Liu, J.Y., Pulinets, S.A., Tsai, Y.B. and Chuo, Y.J., 2000. Seismo-ionospheric signature prior to $M \geq 6.0$ Taiwan earthquakes. *Geophys. Res. Lett.*, 27(19), 3113-3116.
- Liu, J.Y., Chen, Y.I., Chuo, Y.J. and Tsai, H.F., 2001. Variation of ionospheric total electron content during the Chi-Chi earthquake. *Geophys. Res. Lett.*, 28(7), 1383-1386.
- Liu, J. Y., Chuo, Y.J., Pulinets, S.A., Tsai, H.F. and Zeng, X., 2002. A study on the TEC perturbations prior to the Rei-Li, Chi-Chi, and Chai-Yi earthquakes, *Seismo Electromagnetic: Lithosphere-Atmosphere-Ionospherecoupling*, Eds. Hayakawa, M., Molchanov, O.A., Terra Scientific Pub. Co., Tokyo, Japan, 297-301.
- Liu, J.Y., Chen, Y.I., Jhuang, H.K. and Lin, Y.H., 2004a. Ionospheric foF2 and TEC anomalous days associated with $M \geq 5.0$ earthquakes in Taiwan during 1997-1999. *Terr. Atmos. Ocean. Sci.*, 15, 371-383.
- Liu, J.Y., Chuo, Y.J., Shan, S.J., Tsai, Y.B., Chen, Y.I., Pulinets, S.A. and Yu, S.B., 2004b. Pre-earthquake ionospheric anomalies registered by continuous GPS TEC measurements. *Ann. Geophys.* 22, 1585-1593.
- Liu, J.Y., Chen, Y.I., Chuo, Y.J. and Chen, C.S., 2006. A statistical investigation of pre-earthquake ionospheric anomaly. *J. Geophys. Res.*, 111.
- Liu, J.Y., Chen, Y.I., Chen, C.H., Liu, C.Y., Chen, C.Y., Nishihashi, M., Li, J.Z., Xia, Y.Q., Oyama, K.I., Hattori, K. and Lin, C.H., 2009. Seismo-ionospheric GPS total electron content anomalies observed before the 12 May 2008 $M_w 7.9$ Wenchuan earthquake. *J. Geophys. Res.*, 114(A04320), 1-10.
- Liu, J.Y., Chen, C.H., Chen, Y.I., Yang, W.H., Oyama, K.I. and Kuo, K.W., 2010. A statistical study of ionospheric earthquakes precursors monitored by using equatorial ionization anomaly of GPS TEC in Taiwan during 2001-2007. *J. Asian Earth Sci.*, 39, 76-80.
- Liu, J.Y., Chen, Y.I., Chen, C.H. and Hattori, K., 2011. Temporal and spatial precursors in the

- ionospheric global positioning system (GPS) total electron content observed before the 26 December 2004 M9.3 Sumatra-Andaman Earthquake. *J. Geophys. Res.*, 115(A09312), 1-13.
- Naaman, S., Aplerovich, L.S., Wdowinski, S., Hayakawa, M. and Calais, E., 2001. Comparison of simultaneous variations of the ionospheric total electron content and geomagnetic field associated with strong earthquakes. *Nat. Hazards Earth Syst. Sci.*, 1, 53-59.
- Pulinets, S.A., Contreras, A.L., Bisiacchi-Giraldi, G. and Ciralo, L., 2005. Total electron content variation in the ionosphere before the Colima, Mexico, earthquake of 21 January 2003. *Geo. Int.*, 44(4), 369-377.
- Pulinets, S.A., Bondur, V.G., Tsidilina, M.N. and Gaponova, M.V., 2010. Verification of the concept of seismoionospheric coupling under quiet heliogeomagnetic conditions, using quiet heliogeomagnetic conditions, using the Wenchuan (China) earthquake of May 12, 2008, as an example. *Geomag. Aero.*, 50(2), 231-242.
- Pulinets, S. and Davidenko, D., 2014. Ionospheric precursors of earthquakes and Global Electric Circuit. *Adv. Space Res.*, 53(5), 709-723.
- Pundhir, D., Singh, B. and Singh, O.P., 2014. Anomalous TEC variations associated with the strong Pakistan-Iran border region earthquakes of 16 April 2013 at a low latitude station Agra, India. *Adv. Space Res.*, 53(2), 226-232.
- Pundhir, D., Singh, B., Singh, O.P., Gupta, S.K., Karia, S.P. and Pathak, K.N., 2017. Study of ionospheric precursors using GPS and GIM-TEC data related to earthquakes occurred on 16 April and 24 September, 2013 in Pakistan region. *Adv. Space Res.*, 60, 1978-1987.
- Singh, R.P., Kushwah, V.K. and Chauhan, R.S., 2004. Attenuation of ULF-VLF seismo-electromagnetic signals and their propagation to long distances, *Ind. J. Rad. and Space Phys.*, 33, 189-195.
- Xia, C., Wang, Q., Yu, T., Xu, G. and Yang, S., 2011a. Variation in ionospheric total electron content before three earthquakes in the Quighai-Tibet region. *Adv. Space Res.*, 47, 506-514.
- Zakharenkova, I.E., Shagimuratov, I.I., Krankowski, A. and Lagovsky, A.F., 2007. Precursory phenomena observed in the total electron content measurements before great Hokkaido earthquake of September 25, 2003 (M=8.3). *Stud. Geophys. Geod.*, 51, 267-278.

Received on: 3.5.19; Revised on: 7.6.19; Accepted on: 17.7.19

Evolution of gas bearing structures in Jaisalmer Basin (Rajasthan), India

Rajesh Pandey^{1*}, Dinesh Kumar¹, A.S. Maurya¹, and Pooja Pandey²

¹Department of Earth Sciences, Indian Institute of Technology, Roorkee-247667

² Department of Applied Sciences, PEC University of Technology, Chandigarh-160012

*Corresponding author: rajeshbhu20@gmail.com

ABSTRACT

Evolution of the Jaisalmer Basin in terms of the structure and kinematics, are not well understood. This basin contains sediments ranging from Neoproterozoic age to Recent. Each tectonic unit of the basin has different evolutionary history. The basin has passive margin setting since inception and has been affected by regional tectonics of Dharwar, Aravalli and Satpura orogeny since Archean to Proterozoic periods. Present study is focused on the tectonic evolution of different gas bearing structures located over Jaisalmer Mari High. This high was evolved in Late Cretaceous-Paleocene time, with sinistral strike-slip movement in NNW-SSE to NW-SE direction, due to separation from Madagascar and Himalayan collision. Different gas bearing structures at Mari high are associated with transpressional tectonics, and thus study of these structures, will help in understanding of reservoir dynamics, as well as entrapment model of the basin.

Key words: Jaisalmer Basin, Kinematics, Himalayan collision, Transpressional tectonics, Mari High

INTRODUCTION

Jaisalmer Basin is a pericretonic basin, located in the eastern part of Great Indus Basin. It is subdivided in four tectonic units, namely, Jaisalmer Mari High, Shahgarh, Kisangarh and Miajlar sub-basins (Misra et al., 1993, Singh, 2000, Singh, 2006) (Figure 1). Structural analysis over these basins is very limited because of poor, dune covered scarce exposures. Most of the earlier studies are mainly focused on paleontological and sedimentological analysis of exposed sequences. The approach adopted in this paper was to investigate and display the effect of faults to the accumulation of hydrocarbons in the structures, identified in Jaisalmer Basin, Rajasthan. Pursuant to this investigation, it was predicted that which closure, have higher probability to act as trap and or otherwise. Explorationists harbor a variety of opinion concerning the role played by fault in the migration and entrapment of hydrocarbons. Exploration activities by ONGC (Oil and Natural Gas Corporation), have been centered over Jaisalmer Mari High, trending NW-SE direction. Surface geological map suggest the sinistral strike slip motion in same direction (Figure 2). Gas

discoveries has been established from 7 fields, namely, Manhera Tibba, Kharatar, Bankia, Ghotaru, Chinnewala Tibba, Sadewala and Bakhri Tibba (Figure 3). Focus Energy limited has further established one field i.e. SGL field from Cretaceous and Late Jurassic sequence, while OIL (Oil India Limited) has established Tanot Field from Cretaceous sequences. The structures on Mari High are gas bearing in both Tertiary as well as Cretaceous reservoirs. To understand the reservoir dynamics and entrapment model of the basin, a comprehensive understanding of fault kinematics is necessary. The main structural highs mapped in the sub-surface are from Manhera Tibba, Ghotaru and Kharatar gas fields. As mentioned earlier, interpretation of tectonic evolution of the structures, has been difficult due to sand dunes cover, thus newly acquired 3D seismic data from the area have improved our understanding about these structures. The character of the seismic reflectors in the Jurassic sequence (Jaisalmer Formation) is by far the best represented across the structure, where the growing number of wells provide an important control on the seismic interpretation.

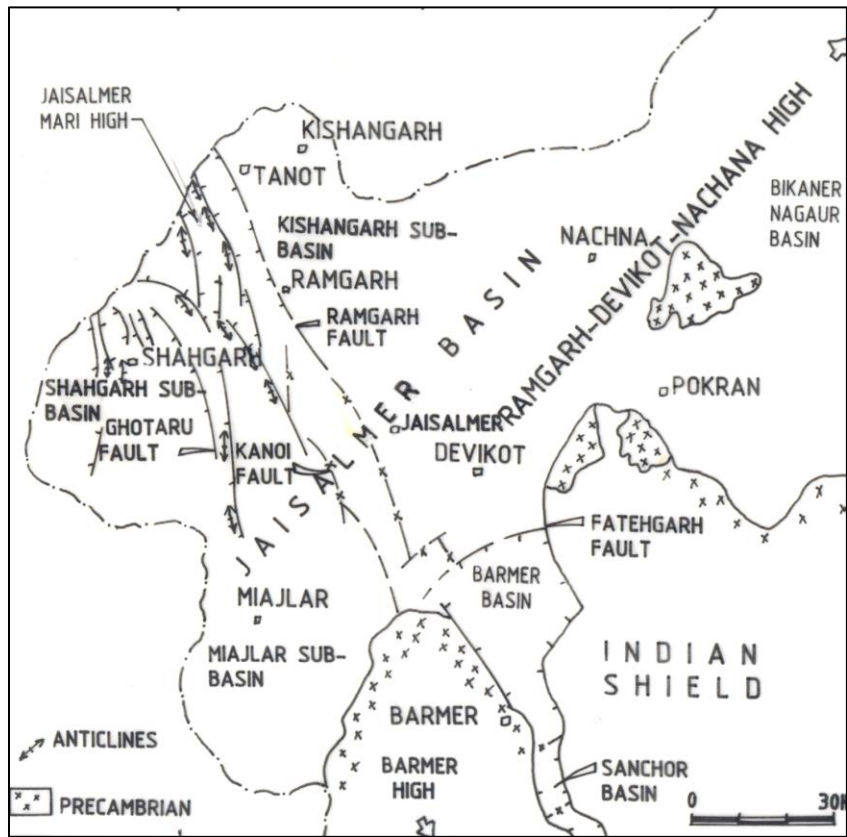


Figure 1. Structural elements of Jaisalmer Basin (modified after Singh, 2006)

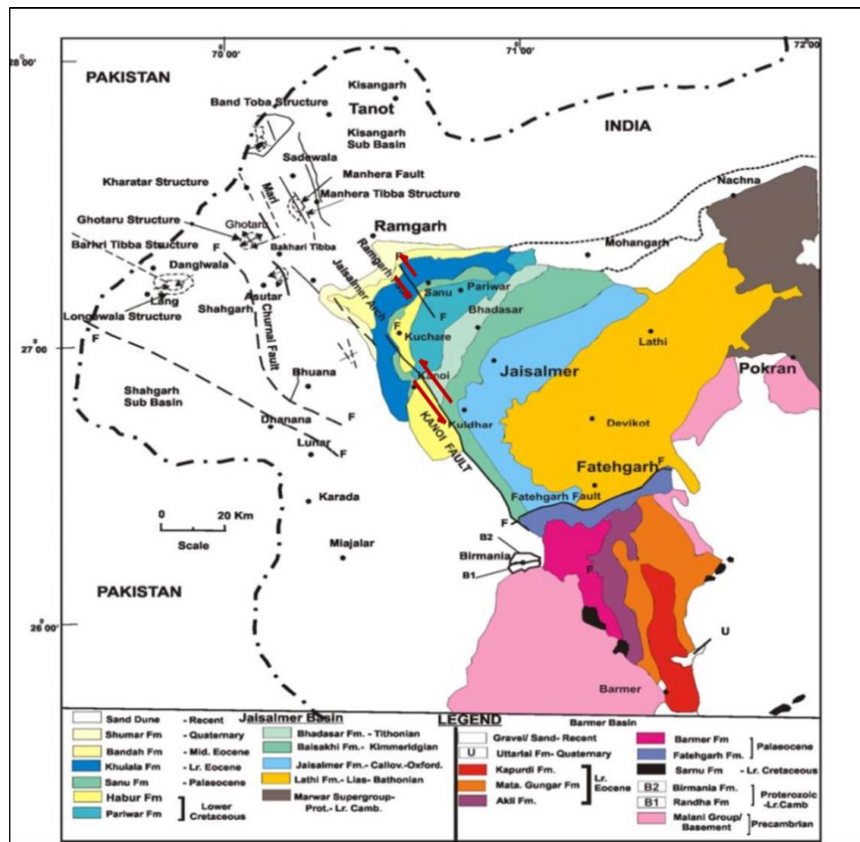


Figure 2. Geological Map of Jaisalmer with strike slips movement on surface exposures (Das Gupta, 1975).

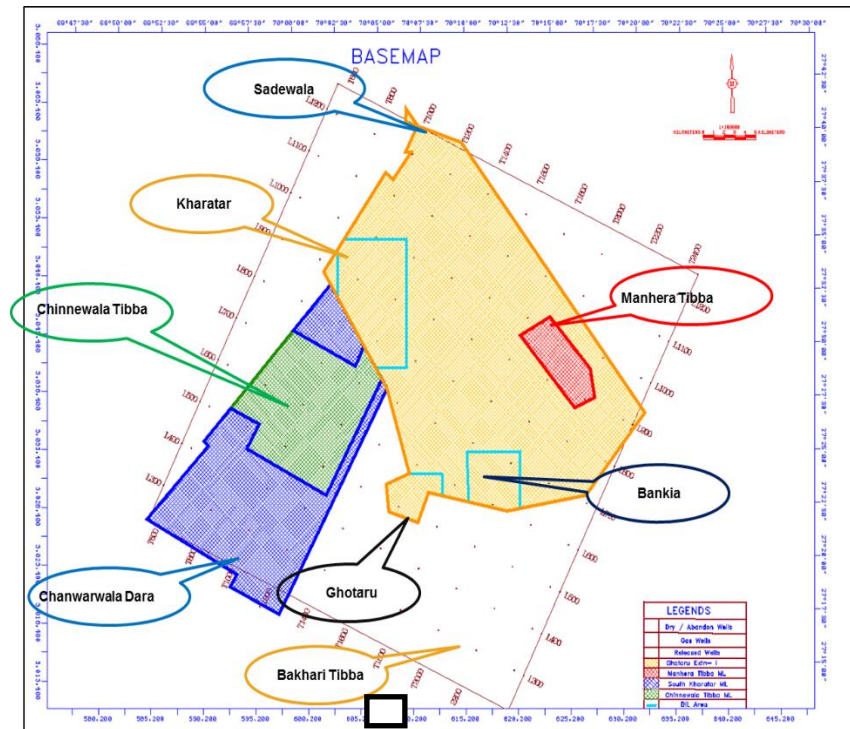


Figure 3. Different gas fields of ONGC with PML Acreages in Jaisalmer Basin

STRATIGRAPHY

The Neoproterozoic to recent sedimentary strata in the Jaisalmer Basin, has been subdivided into the Randha, Birmania, Karampur, Sumarwali, Lathi, Jaisalmer, Baisakhi-Badesar, Pariwar, Goru, Parh, Sanu, Khuiala, Bandah and Shumar formations,

with four major unconformities, Late Cambrian to Early Carboniferous, within Early Jurassic, Late Cretaceous- Early Paleocene and Early to Middle Eocene. Brief stratigraphic record of the Jaisalmer Basin, along with established depositional environment, is given in Table 1.

Table 1. Stratigraphic record of Jaisalmer basin

Formation	Age	Depositional environment
Shumar	Recent to Pleistocene	Fluvial, lacustrine, eolian
Bandah	Middle Eocene	Marine shelf environment
Khuiala	Lower Eocene	Shallow shelf environment
Sanu	Paleocene	Continental to marine
Parh	Upper Cretaceous	Open marine environment
Goru	Upper Cretaceous	Overall transgressive with smaller regressive pulses
Pariwar	Lower Cretaceous	Overall regressive phase with some marine incursions
Baisakhi-Badesar	Upper Jurassic	Near shore to shallow marine
Jaisalmer	Middle Jurassic	Low energy marine environment
Lathi	Lower Jurassic	Fluvio-Deltaic environment
Birmania	Proterozoic to Lower Cambrian	Marine, reducing environment with restricted circulation
Randha	Proterozoic to Lower Cambrian	Continental to Near shore

A more detailed description of the stratigraphy has been presented by Mishra et al., (1993) and recently reviewed by Khan and Khan (2015).

METHODOLOGY

Coherency maps on top of best reflector i.e. close to top of Jaisalmer Formation have been generated in 3D seismic volume within the study area, for identification and validation of prominent faults along with major fault trends (Figure 4). 3D seismic data is comparatively better for attribute generation. Therefore, the generated coherency attribute from this data brings out a better display of the fault trends. Taking the guidance from

attributes generated from the merged volume, detailed fault interpretation was carried out in every 10th inline and also in cross lines and time structure map was prepared (Figure 5). Based on the interpretation of the coherency maps, it became clear that major faults trends are oriented in NE-SW, E-W and NNW-SSE directions. On this basis, it was decided to use In-lines for fault picking because of their orthogonal orientation to the major faults in study area. It has been observed that the study area was subjected to extensional along with minor compressional tectonic forces during the geological past.

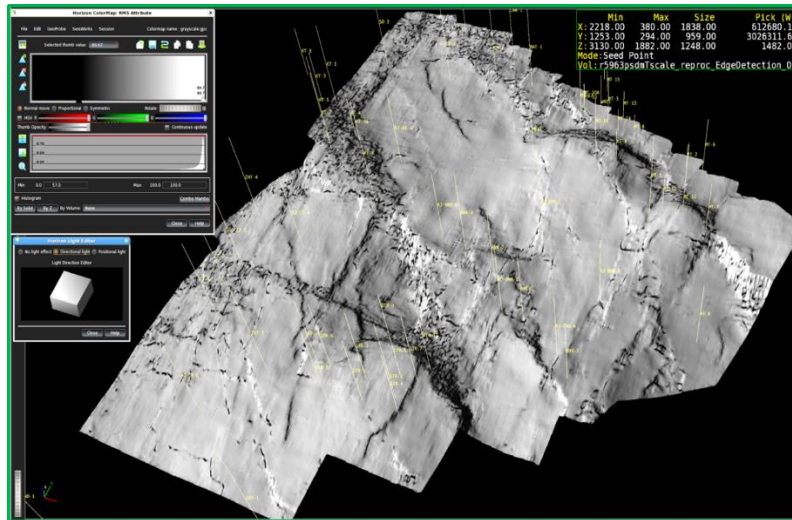


Figure 4. Coherency map on top of Jaisalmer Formation

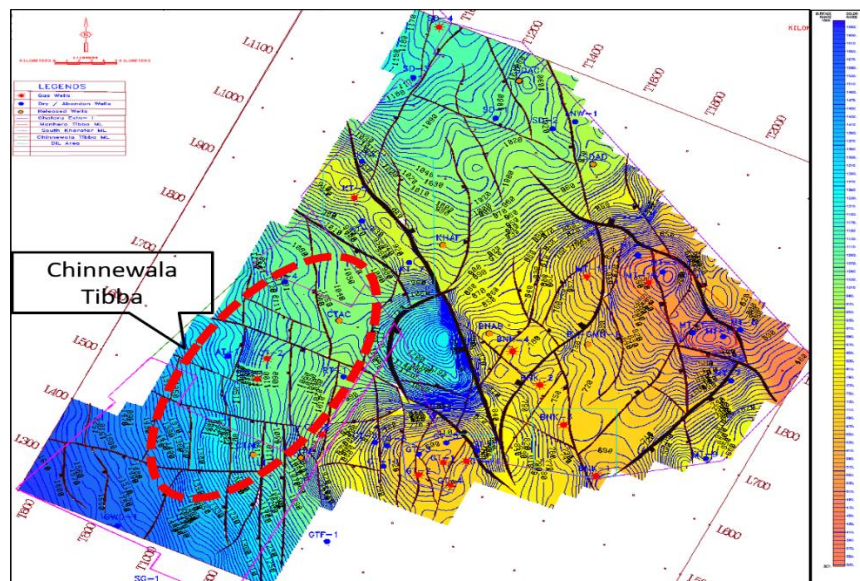


Figure 5. Paralleling monoclines and oblique, en echelon normal faults

Moreover, to compare the current study area with regional fault pattern of Jaisalmer Basin, fault correlation in entire basin has been carried out in sub-surface 3D and 2D seismic data and map was prepared (Figures 6a, b), which shows similar fault trends. Paleo-structural study was also carried out using drilled wells in the basin passing from Shahgarh depression to Jaisalmer Mari High. For this study, the well tops were flattened from bottom most Formation top to topmost, to see the thickness variation. It was observed that up to K-T (Cretaceous-Tertiary) boundary (Parh Top), the

thickness is same in Shahgarh depression and Jaisalmer Mari High, while in Paleocene and Eocene sequences, less thickness has been observed at Jaisalmer Mari High (Figure 7). This work utilised seismic data and well data of Jaisalmer Basin, which was loaded and quality checked into the interpretative tool, in this case Petrel software. Manual mapping of the major regional faults was done. The original seismic volume was steered to improve its quality by increasing the signal to noise ratio.

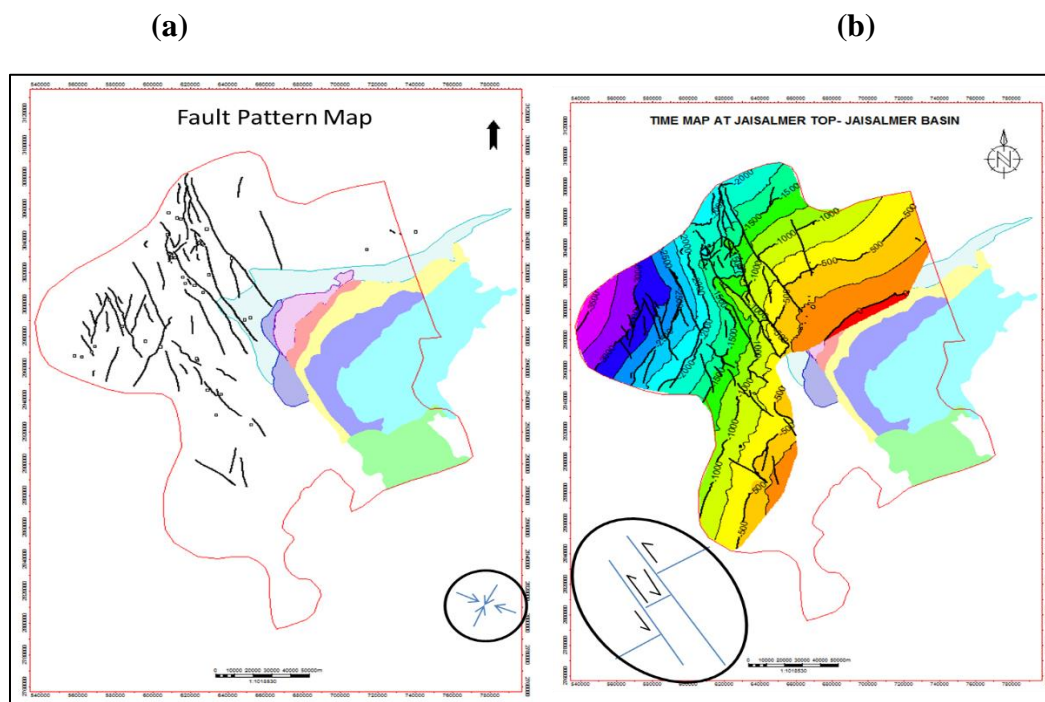
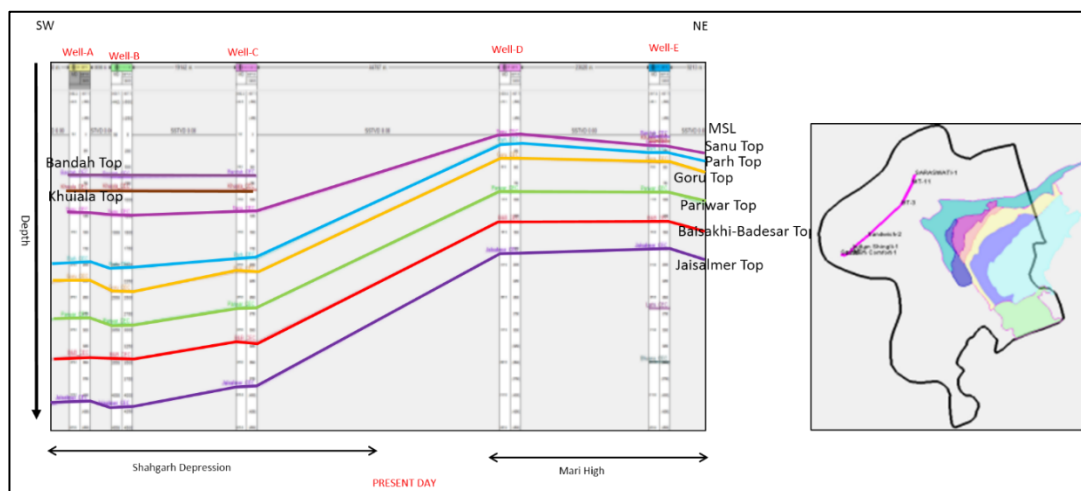


Figure 6. (a) Fault Pattern map in Jaisalmer Basin with surface geological exposures. (b) Time structure map on top of Jaisalmer Formation with displayed fault pattern



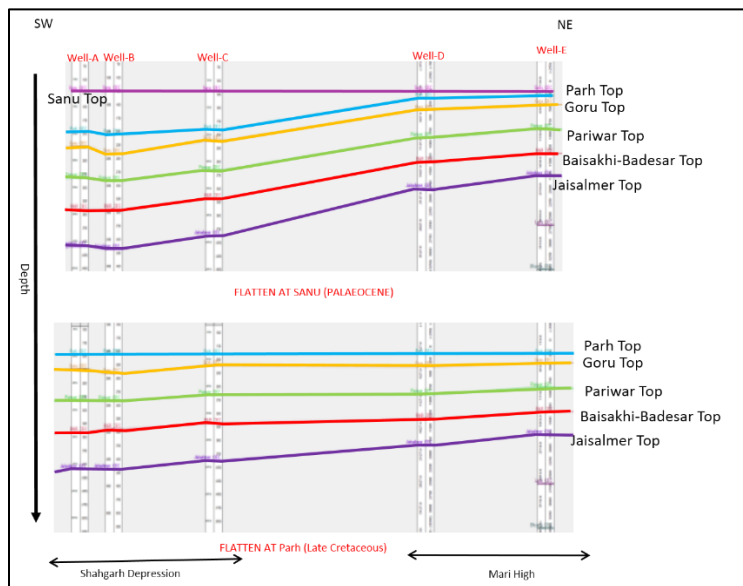


Figure 7. Paleo-Structural Analysis from Shahgarh low to Jaisalmer Mari High

STRUCTURAL PATTERN

Structural style of the basin is associated with major structural trends of the Indian subcontinent. Three major structural trends viz. NE-SW (Aravalli grain), ENE-WSW/E-W (Satpura grain) and NNW-SSE (Dharwarian grain), influenced the basin evolution and structural configuration from time to time (Das Gupta, 1975, Roy and Jakhar, 2002). These trends have given rise to a distinct fault pattern, with multiple orthogonally/obliquely-related faults straddling the area. The structural style of Jaisalmer Basin can be traced on outcrops and in subsurface, by faults and the maximum effect of faulting is limited between Ramgarh and Kanoi Faults (Sharma et al., 2016, Mishra and Sharma, 1986). Major Faults in the region are Mansurian Fault and Ghotaro Fault in the west, Kanoi Fault and Manpiya Ramgarh Fault near Jaisalmer. Surface faults demonstrate sinistral movement trending NW-SE (Figure 2), majority being the strike slip faulting. Further, thermal doming and hotspot activity in the basin is associated with the separation of the Indian and Madagascar plates (Khan et al., 2013) The Himalayan collision (Oligocene to present-day)

has also caused sinistral transpression in the west of the Lower Indus Basin, due to which fold-thrust structures are overprinted by sinistral flower structures in the basin (Farshor, 1972). In subsurface, faults in the study area are generally vertical excepts over the transpressional/transensional structures.

Two major fault trends mapped during the study are, (i) NNW-SSE trending mainly strike-slip/wrench faults, and (ii) NNE-SSW trending faults

The major NNW-SSE trending fault-set comprising the Ramgarh-Kanoi fault zone shows a distinct strike-slip movement. The fault profiles on the sections are near vertical. The main sense of strike-slip movement along the two major faults bounding the Ramgarh-Kanoi fault zone, appears to be sinistral (left-lateral), as is evident from NNE-SSW trending structure contours veering towards NNW in the fault zone and then again showing NNE-SSW trend (Figure 6).

The interplay of stresses, however, has created a right-lateral (clockwise) sense of movement in the area, confined between the bounding faults of the

zone (Figure 8). The fault throw in many cases shows wrenching effects, similar to Ramgarh Fault, mapped as the eastern bounding fault of the

zone that shows an increase away from a point, where there appears to be little or no throw ('Null Point'), which is an indication of wrench faulting.

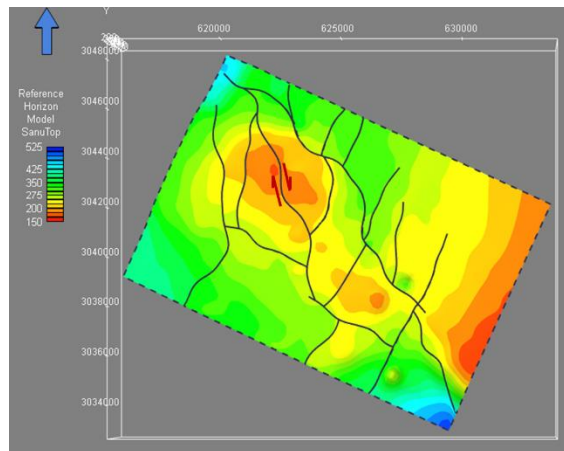


Figure 8. Right-lateral (clockwise) sense of movement between interplay stresses, Manhera Tibba Jaisalmer Basin.

The long-distance faults, as mapped in the area, often cover different segments. The fault toes tend to link together, where there is an overlap between two segments, giving rise to overstep or restraining bends. The oversteps or restraining bends, are sites where transpressional stresses are in play. An array of 'positive' flower structures was mapped in the areas of stepovers or restraining bends, where the transpressional stresses have led to formation of up-faulted blocks (Figure 9). The highs thus formed in

such sectors, where the fault toes link together (oversteps/stepovers) host some of the main gas fields in and around the Jaisalmer-Mari High area. The interaction between the NNW-SSE and NNE-SSW trending fault trends, as mapped in the Shahgarh Depression, has led to creation of an array of segments where entrapment of gaseous hydrocarbons is noticed as in the SGL field and the area in its vicinity.

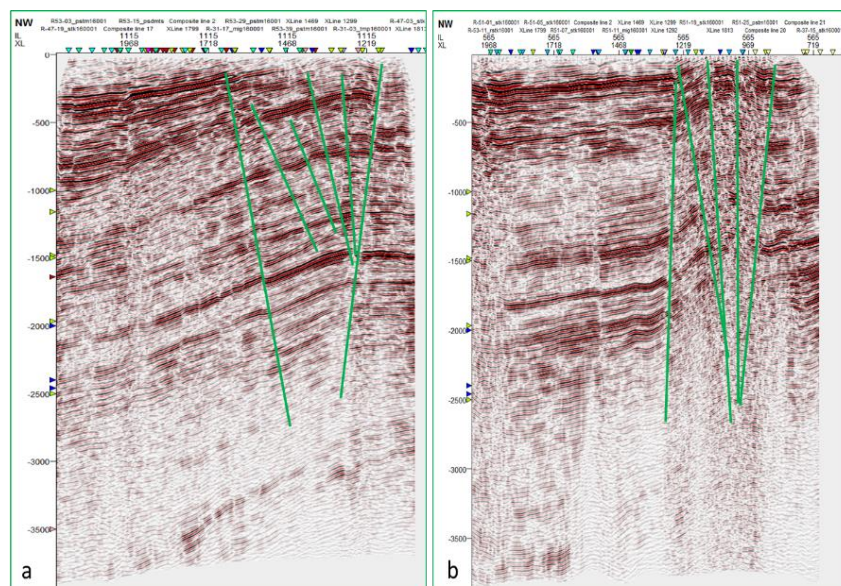


Figure 9. Seismic section showing transpressional (positive flower) structure from (a) Ghotaru (b) Manhera Tibba Structures.

Indications of Transpression/Transtension

Most of the gas bearing structures viz. Manhera Tibba, Kharatar, Bankia, Ghotaru and Chinnewala Tibba, are the results of strike slip tectonics in the basin. Paleostructural analysis from Shahgarh low to Jaisalmer Mari High suggests that Mari high has developed in Late Cretaceous to Paleocene time during Madagascar-India separation and Himalayan collision. Jaisalmer Mari High is strongly affected with transpressions/ transtension tectonics. There are several indications of transpressional deformation:

- (i) Major Fault zone Ramgarh-Kanoi shows a distinct strike-slip movement that occurred during Cretaceous-Tertiary time in Indus Basin.
- (ii) Seismic interpretation of new 3-D data from the ONGC mining leases (MLs) shows elements (contractional faults) with an orientation and sinistral transpression along a NW-SE lineament. Ghotaru Structure shows a prominent positive flower structure.

Such positive inverted structures imply specific modes of formation, and their distinctive characteristics make them important criteria for the identification of strike-slip structural styles (Harding, 1985).

- (iii) A central low between Ghoratu and Kharatar represents a negative flower structure, consisting of a shallow synform, bounded by upward-spreading strands of a wrench fault that have shown mostly normal separations (Figure 10).
- (iv) Paralleling monoclines and oblique en echelon normal faults and strike-slip faults of Chinnewala Tibba flank, which is the divergent wrench fault (Figure 4).
- (v) Deep seated fault of Mahnera Tibba gas field structure shows a right-lateral (clockwise) sense of movement in the area, confined between the bounding faults of the zone, which is thought to have experienced the interplay stresses within the basin.

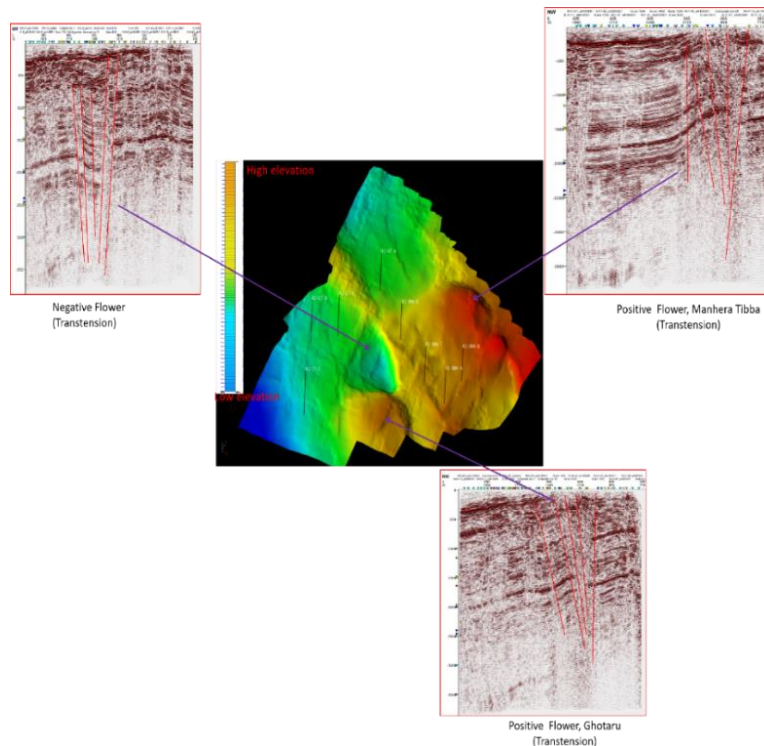


Figure 10. Positive and negative flower at Jaisalmer Mari High within ONGC Acreage

Evolution of Gas Bearing Structures

The basin has passive margin setting since inception and was affected by regional tectonics of Dharwar, Aravali and Satpura orogeny during Archean and Proterozoic periods, as mentioned before. The reactivation of major tectonics occurred during and after its separation from Madagascar and collision of Indian plate with Eurasian plate. Initially, during cretaceous time a 'Y' shaped major lineament existed around Ghotaru, Kharatar and Chinnewala Tibba Structure. During the separation of Madagascar/Himalayan collision, sinistral strike-slip motion took place in the lineament. This

resulted in transpressional regime in Ghotaru and Kharatar and a transtensional regime in between the both. The transtensional regime resulted in creation of central low of the study area. Similarly, the Manhera Tibba structure developed due to movement of Ramgarh-Kanoi fault zone. The interplay between these two major fault zones led to right-lateral (clockwise) sense of movement in the area (Figure 11). Shahgarh low is less affected with strike-slip tectonics, the hydrocarbon entrapment here is low due to interaction between the NNW-SSE and NNE-SSW trending faults. Coherency map on top of best reflector (Jaisalmer Formation), shows the present architecture of faults and to some extent their sense of movement.

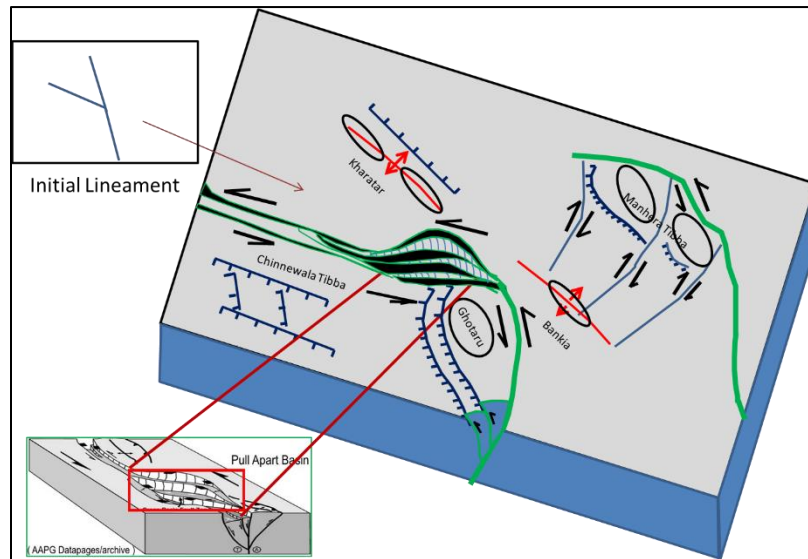


Figure 11. Cartoon diagramme representing structural elements of study area

CONCLUSIONS

Integrating various data sets from surface to sub-surface have provided a better understanding of tectonics and sedimentation history of the basin. The structural style in the study of Jaisalmer is tough, because of sand dunes. Few surface exposures away from the study area and regional tectonics helped us to understand evolution of different gas bearing structures. The analysis suggests that the basin has gone under various deformations since inception from its separation of

Madagascar. Thermal doming, hotspot activity and some strike-slip movements were associated with Madagascar and India separation in Cretaceous. Major hydrocarbon bearing structures of the area are related to Himalayan collision, which took place around 50 Ma back. Further, The Ghotaru, Kharatar, Bankia and Manhera Tibba gas fields are Transpressional structures. Chinnewala Tibba fields are also influenced with strike-slip tectonic movements, but the major hydrocarbon entrapment is due to interaction of NNW-SSE and

E-W fault systems. Entrapment in Chanerwala Dara and Shahgarh low is purely associated with interaction of NNW-SSE and NNE-SSW fault systems. The combined information from seismic and surface data enables understanding of fluid dynamics of potential fields and understanding of their spatial and temporal relationship within the study area.

ACKNOWLEDGEMENT

Authors are grateful to the management of ONGC for giving permission to publish this work. Authors also acknowledge GGM-Basin Manager, Frontier Basin, ONGC, Dehradun, for providing an opportunity and all necessary facilities to prepare this paper. Authors wish to acknowledge the support given by all colleagues in the group. The views expressed in the paper are of the authors not the organization, they belong.

Compliance with Ethical Standards

The authors declare that they have no conflict of interest and adhere to copyright norms.

REFERENCES

Das Gupta, S.K., 1975. Revision of the Mesozoic–Tertiary stratigraphy of the Jaisalmer Basin Rajasthan. *Indian J. Earth Sci.*, 2, 77–94.

Farshori, M.Z., 1972. *The Geology of Sindh*, University of Sindh, Jamshoro.

Harding, T.P., 1985. Seismic characteristics and identification of negative flower structures, positive flower structures and positive structural inversion, *Bull. Am. Assoc. Petrol. Geol.*, 69 (4), 582-600.

Khan N., Konaté, A.A. and Zhu, P., 2013. Integrated geophysical study of the Lower Indus Platform Basin area of Pakistan, *Int. J. Geosci.*, 4, 1242-1247, <http://dx.doi.org/10.4236/ijg.2013.49118>.

Khan Z. and Khan A.A., 2015. A Review on lithostratigraphy and biostratigraphy of Jaisalmer basin, western Rajasthan, India, *Int. Res. J. Earth Sci.* 3(8), 37-45

Mishra, P.C. and Sharma, P.C., 1986. Geological analysis of Lower Goru Formation with special reference to hydrocarbon occurrence, Jaisalmer basin, Rajasthan. ONGC report (unpublished).

Misra, P.C. and Singh, N.P., 1993. Lithostratigraphy of Indian Petroliferous Basin, Document-II, West Rajasthan Basin, ONGC report (unpublished).

Robertus H., 2013. Pull apart basin: Big power of Wrench Fault, AAPG datapages/Archive.

Roy, A.B. and Jakhar, S.R., 2002. *Geology of Rajasthan (Northwest India, Precambrian to recent)*, Scientific Publishers (India) Jodhpur.

Sharma, P., Vaishnav, K. and Bhu, H., 2016. Tectono-Geomorphic Features around Jaisalmer (Rajasthan), *Int. J. Sci. Res.* 5(4), 153-157.

Singh, N.P., 2000. Relevance of laboratory studies in geological modelling and field geology, ONGC report (unpublished).

Singh, N.P., 2006. Mesozoic lithostratigraphy of the Jaisalmer Basin, Rajasthan, *J. Paleontological Soc. India*, 51(2), 1-25.

Received on: 23.2.19; Revised on: 16.6.19; Accepted on: 18.7.19

Delineation of groundwater potential zones in hard rock basement terrains of East Godavari district, Andhra Pradesh, India

P. Venkateswara Rao, M. Subrahmanyam* and P. Ramdas

Department of Geophysics, Andhra University, Visakhapatnam- 530003 (A.P).

*Corresponding Author: smangalampalli@rediffmail.com

ABSTRACT

Exploration for groundwater in hard rock terrain has always been a herculean task. To address such an issue in the East Godavari district of Andhra Pradesh, resistivity data of about 70 vertical electrical soundings (with schlumberger array), are interpreted for obtaining true resistivities and thicknesses of the subsurface layers. Six apparent resistivity pseudo-sections, based on the layer parameters and their corresponding lithology sections, led to the understanding of the subsurface lithology in a better perspective. The fence diagrams drawn for five different regions resulted in delineation of the weathered zone, which is a good aquifer source that extends over an area of about 308 sq. km in the central part of the study region, with an average thickness of 15 m at a shallow depth of less than 6 m. On the other hand, in the SSW part of the study area, semi weathered/fractured rock forms the source of groundwater at relatively deeper levels of 10 to 27 m.

Keywords: Vertical electrical resistivity sounding, Groundwater potential zones, Hard rock basement terrains, Pseudo section, Fence diagram, Lithologic section.

INTRODUCTION

Hard rock complex terrains are underlain largely by impermeable igneous and metamorphic rocks, usually of Precambrian age. These rocks are most often characterized by low porosity and permeability. The occurrence of groundwater in these areas is mainly due to the development of secondary porosity and permeability resulting from weathering and fracturing. The geoelectrical method is an effective tool for ascertaining the subsurface geologic framework of an area, especially in hard rock terrains (Keller and Frischknecht, 1966; Bhimasankaran and Gaur, 1977; Zohdy, 1989; Srivastava and Bhattacharya, 2006; Prasanna et al., 2009; Srinivasamoorthy et al., 2013; Seyedmohammadi et al., 2016; Vasantrao et al., 2017; Subrahmanyam and Venkateswara Rao, 2017; Ashraf et al., 2018). The main purpose of the investigation is to detect promising zones for the location of new wells in

the study area, through an integrated analysis of the different types of interpretation techniques. Such zones can be exploited for drinking or agriculture purposes based on the quality of water.

Hydrogeology and Tectonics of the area

The area falls in the Yeleru river basin covering an area of 840 sqkm (Figure 1). The topography is steep with altitudes ranging from 80 m above mean sea level (amsl) near main stream of Yeleru river in southern part of study area to 560 m amsl in northern-most parts. This study area is covered by three major rock formations, including hard and massive khondalite, charnockites and granite-gneisses of hard foliated migmatite group. The Khondalite group is represented by quartz-garnet-silliminite-graphite gneiss along with quartzite and calc-granulites/gneiss. The Charnockites group consists of acidic, intermediate and basic varieties. The Migmatite group includes a host of rock types

like porphyroblastic granitoid gneiss, garnetiferous quartz of eldspathic gneiss (leptynite), garnet-biotite-hypersthene gneiss and quartz of eldspathic mobilizates. The annual normal rainfall of the district is 1280.0 mm. In this study area, the groundwater is restricted to soil and regolith cover, weathered and fissured zones,

under semi confined and confined water table conditions. The remote sensing image (ASTER) of the study area has also been processed for the lineaments. It is observed that central part of the study area is characterized by dense lineaments as shown in figure 1, which are possible sources for ground water recharge.

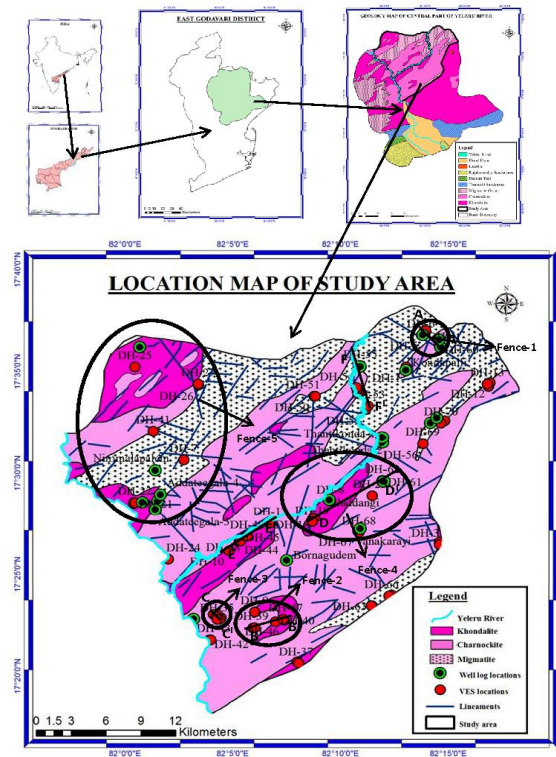


Figure 1. Location map of study area with lineaments (solid lines). Circles indicate the locations of fence diagrams. AA', BB', CC', DD', EE' and FF' are the lines of apparent resistivity pseudo and lithology sections

METHODOLOGY

Electrical resistivity data of 70 Vertical electrical soundings (VES) using Schlumberger array with maximum half- current electrode spacing varying between 40-110 m, has been used in this study. Data for 45 VES points have been taken from the Andhra Pradesh state groundwater board and remaining data was collected through this study. The entire data was initially interpreted with theoretical curves, prepared by Orellana and Mooney (1966) for a preliminary understanding of the true resistivities and thicknesses of the

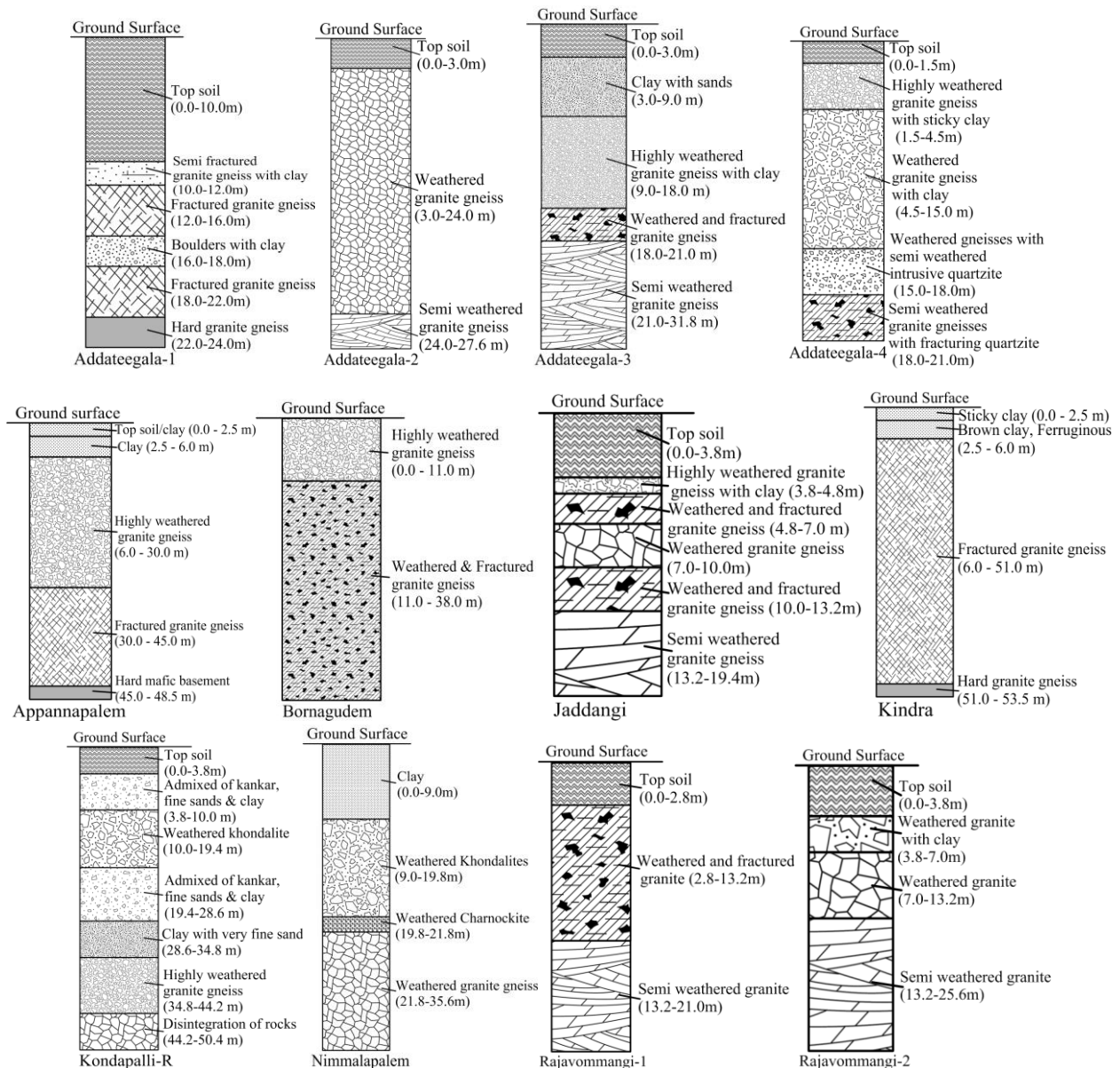
subsurface layers. The shapes of the curves indicate 3-5layer subsurface patterns, corresponding to A, H, AA, HA, KH, QH, HAA and QHA type. These curves have been reinterpreted with IPI2Win software (Bobachev, 1990-2002) as the interpreted parameters (resistivity and thicknesses) of this technique, are reasonably close to the actual values in spite of large deviations in the input models (Venkateswara Rao et al., 2019). The results obtained from partial curve matching technique were given as inputs for IPI2W in software. Basing on the interpreted values of the resistivity

and thickness of sounding curves and from the knowledge of the lithology at the observation wells, subsurface cross sections along possible lines and fence diagrams for regions with dense locations of VES points were prepared.

RESULTS AND DISCUSSION

Based on the interpreted resistivity values (Table 1), geology of the area and lithology of the existing twenty observation wells are shown in figure 2 where the subsurface lithology can be

classified broadly into top soil, clay/highly weathered, weathered, semi weathered/fractured and hard formations. The resistivity ranges of these formations are shown in Table 2. It is observed that out of the 70 locations, about 34 locations show H-type curves, while 31 locations show A-type curves. About 26 locations of the ascending type curves (which cover A and AA type) also indicate the first two layers, with considerable thickness (18-50m) as prospective zones of groundwater.



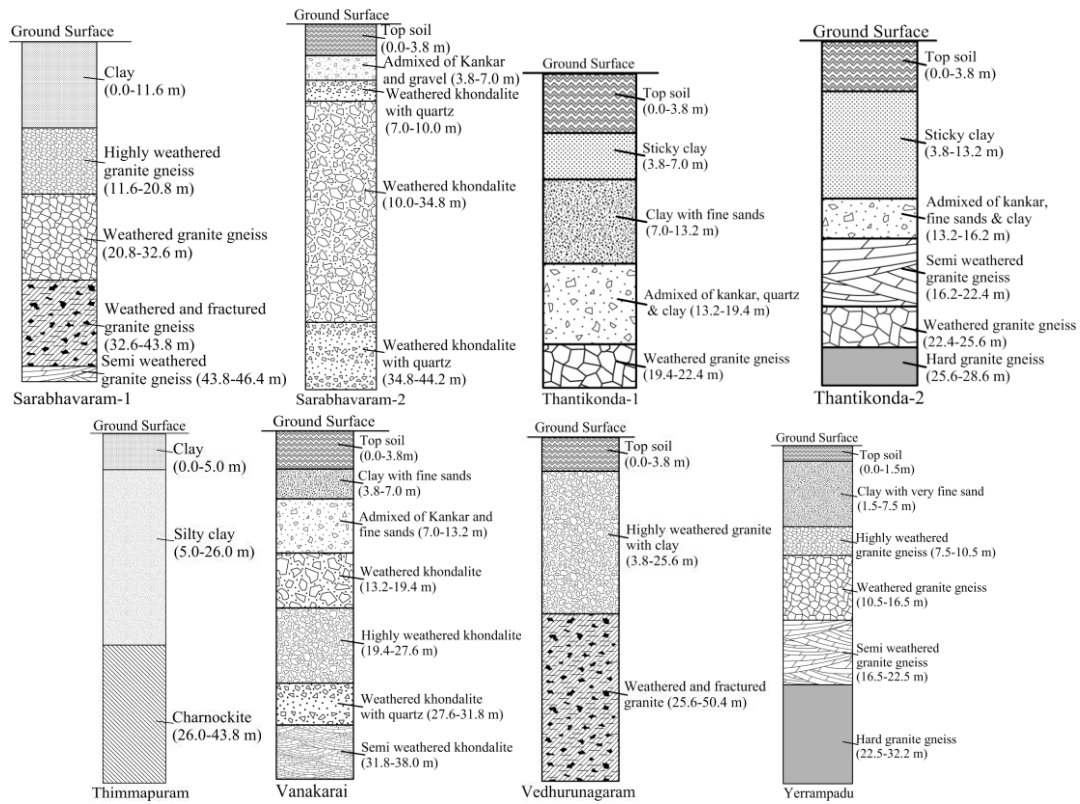


Figure 2. Lithology sections observed at the 20 bore wells in the study area.

Table 1. Interpreted results of the vertical electrical soundings.

Code	Longitude in meters	Latitude in meters	Elevation in meters	Type of Curve	Resistivity (Ω m)					Thickness (m)				Total Thickness (m)
					1st Layer	2nd Layer	3rd Layer	4th Layer	5th Layer	1st Layer	2nd Layer	3rd Layer	4th Layer	
DH-1	82.217	17.587	250	AA	14.8	19.5	66.9	2877	-	2.3	17.4	19.4	-	39.1
DH-2	82.243	17.443	271	HA	27.2	14.5	72.3	2187	-	5.6	9.4	35	-	50
DH-3	82.243	17.441	285	A	16.7	105	343	-	-	2.6	47.4	-	-	50
DH-4	82.23	17.614	270	H	187	35.4	240	-	-	3.2	14.8	-	-	18
DH-5	82.23	17.613	269	HA	52.8	14.7	464	3000	-	1.8	6.9	4.4	-	13.1
DH-6	82.229	17.613	269	HA	54.7	16	610	2942	-	1.4	9.5	8.2	-	19.1
DH-7	82.045	17.511	235	HA	56.1	25.2	53	1696	-	1	11.5	19	-	31.5
DH-8	82.159	17.477	177	HA	16.6	6.9	34.1	2241	-	1.6	7	7.5	-	16.1
DH-9	82.1	17.386	130	HA	19.3	6.6	13.9	863	-	1	6.9	17.9	-	25.8
DH-10	82.08	17.436	194	HA	22.5	9.2	22.5	572	-	1.3	16	10.4	-	27.7
DH-11	82.281	17.571	252	H	25.4	7	119	-	-	1	12.1	-	-	13.1
DH-12	82.282	17.574	255	HA	66.3	9.7	515	5851	-	5.6	5.7	8.1	-	19.4
DH-13	82.28	17.573	248	HA	39.3	9.3	492	5000	-	1.9	4.7	4.7	-	11.3
DH-14	82.181	17.565	212	HA	25.3	11.2	94.3	2070	-	1.7	16.2	17.4	-	35.3
DH-15	82.18	17.569	215	H	85	16	84.9	-	-	2.2	5.3	-	-	7.5
DH-16	82.179	17.57	215	HA	55.8	19.5	124	2827	-	3.4	9.9	13.7	-	27
DH-17	82.112	17.459	191	HA	35	14.8	63.9	1664	-	1.9	9.3	41.4	-	52.6
DH-18	82.146	17.463	169	A	12.4	32.7	2203	-	-	3.5	21.5	-	-	25
DH-19	82.145	17.46	167	A	6	49.8	360	-	-	3.5	8	-	-	11.5
DH-20	82.006	17.476	210	HA	168	88.5	269	13629	-	1	3.4	25.2	-	29.6
DH-21	82.006	17.475	213	H	129	143	239	-	-	2.8	10.2	-	-	13
DH-22	82.007	17.476	208	HA	88	53	252	1419	-	0.9	2.9	55	-	58.8
DH-23	82.191	17.482	189	AA	4.1	11.6	329	1500	-	2.8	6.2	6.6	-	15.6

DH-24	82.033	17.429	152	HAA	14.6	9.1	11.8	77.8	350	1	3.9	19.5	45.7	70
DH-25	82.007	17.587	325	A	16.7	27.2	448	-	-	3.2	10.5	-	-	13.7
DH-26	82.056	17.572	323	QH	468	175	101	281	-	3.2	17.6	32.1	-	52.9
DH-27	82.056	17.573	323	HA	160	38.6	70.3	900	-	1	1.7	5.4	-	8.1
DH-28	82.182	17.587	230	HA	26.9	10.8	149	1872	-	1.1	12.9	25	-	39
DH-29	82.181	17.587	230	AA	15.4	29.8	121	1200	-	3.4	6.9	29.4	-	39.7
DH-30	82.074	17.381	125	A	9	58.6	446	-	-	3	12.5	-	-	15.5
DH-31	82.073	17.38	123	A	9.7	16.9	3954	-	-	3.9	3.7	-	-	7.6
DH-32	82.071	17.384	128	AA	10	27	86.9	834	-	6	5.1	21.4	-	32.5
DH-33	82.068	17.384	127	AA	22.1	27.9	63.3	284	-	3.5	6.7	24.7	-	34.9
DH-34	82.07	17.382	125	AA	9	27.9	75	296	-	1.5	8.9	37	-	47.4
DH-35	82.071	17.38	123	HA	42.5	18.3	102	507	-	2.6	6.8	32.8	-	42.2
DH-36	82.133	17.345	140	KH	121	210	43	4087	-	1.9	3.5	29.1	-	34.5
DH-37	82.134	17.344	148	KH	132	332	50	197	-	1.9	2.9	9.5	-	14.3
DH-38	82.099	17.373	110	HA	72.1	15.7	36.3	135	-	1.7	2.8	11.1	-	15.6
DH-39	82.1	17.373	113	HA	32	8.99	49	1023	-	2.2	4.2	12	-	18.4
DH-40	82.116	17.378	142	QH	25.1	11.4	6.3	129	4173	0.7	9.5	9.3	10	29.5
DH-41	82.021	17.534	314	A	12.1	45.5	4462	-	-	2.6	12.6	-	-	15.2
DH-42	82.065	17.363	105	H	12.2	6.4	98.9	-	-	1.5	11.8	-	-	13.3
DH-43	82.066	17.363	105	A	20.9	56.8	730	-	-	2.6	18.8	-	-	21.4
DH-44	82.088	17.444	186	AA	9.9	16.8	74.2	1207	-	1	2.4	8.4	-	11.8
DH-45	82.089	17.444	185	A	20.3	25.1	117	-	-	3.4	8.4	-	-	11.8
DH-46	82.123	17.379	160	HA	29	14	144	364	-	1.3	14.6	24.8	-	40.7
DH-47	82.122	17.38	160	QHA	34.5	19.2	7.6	120	862	1.3	2.7	23.9	10.7	38.6
DH-48	82.093	17.448	167	A	8.9	34.5	186	-	-	2.5	10.7	-	-	13.2
DH-49	82.094	17.448	172	A	8.7	37.3	564	-	-	4.2	6.2	-	-	10.4
DH-50	82.146	17.563	295	HA	36	22	59.2	2275	-	1.1	5.9	22.4	-	29.4
DH-51	82.147	17.563	296	A	15.1	124	865	-	-	1	10.2	-	-	11.2
DH-52	82.186	17.552	207	A	6.9	30.7	437	-	-	3.4	8.4	-	-	11.8
DH-53	82.188	17.555	205	A	9.6	23.6	190	-	-	3.5	8.4	-	-	11.9
DH-54	82.181	17.588	231	AA	6.9	37.6	463	13199	-	4.8	12.2	12.1	-	29.1
DH-55	82.182	17.588	231	HA	35.5	19.4	209	776	-	1.3	9.7	33.1	-	44.1
DH-56	82.23	17.524	217	A	27.7	110	1264	-	-	6.4	12.3	-	-	18.7
DH-57	82.231	17.616	272	H	49.7	13.2	172	-	-	1.5	12.9	-	-	14.4
DH-58	82.232	17.616	271	A	28.7	11.6	1149	-	-	1.4	4.3	-	-	5.7
DH-59	82.232	17.617	272	A	8.5	21.3	467	-	-	1.7	6	-	-	7.6
DH-60	82.243	17.604	265	AA	6.3	9	40.7	62.3	-	1	2.1	5.4	-	8.5
DH-61	82.199	17.493	207	A	14.3	26.6	316	-	-	1	3.8	-	-	4.8
DH-62	82.199	17.494	208	AA	6.8	14.7	340	2824	-	3	7.5	5.5	-	16
DH-63	82.191	17.391	205	AA	20.8	43.9	1148	8230	-	3.7	7.4	5.8	-	16.9
DH-64	82.19	17.391	205	A	28.4	34	895	-	-	1	6.6	-	-	7.6
DH-65	82.206	17.4	255	H	47.1	13.9	132	-	-	1.2	5.9	-	-	7.1
DH-66	82.204	17.399	251	AA	14.2	19.1	413	5648	-	4.3	5.9	5.3	-	15.5
DH-67	82.18	17.452	198	HA	30.1	9.5	45.2	846	-	0.8	9.2	15.5	-	25.5
DH-68	82.181	17.451	198	HA	71.9	8.6	21.4	222	-	0.8	0.4	12.1	-	13.3
DH-69	82.247	17.543	210	HA	22.6	10.1	128	480	-	0.8	4.4	56.5	-	61.7
DH-70	82.244	17.541	205	HA	39.7	10.2	141	223	-	2	4.8	41.7	-	48.5

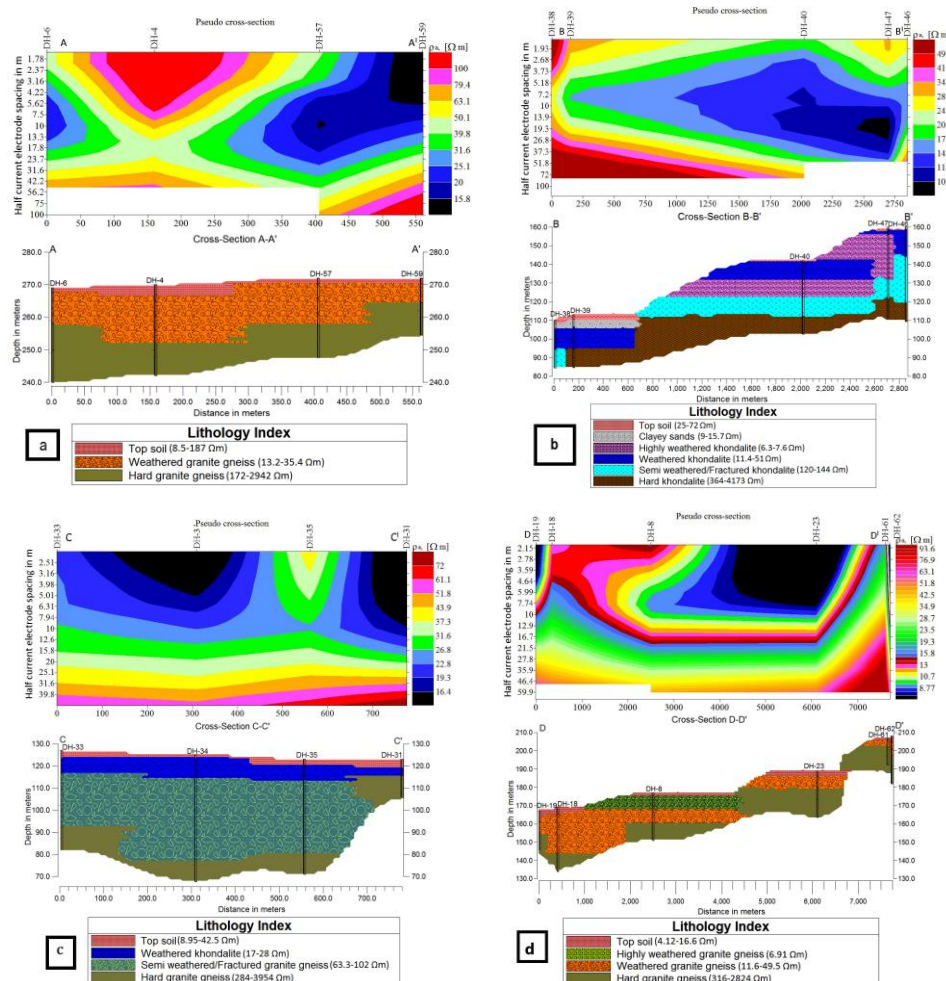
Table 2. Resistivity range of subsurface layers

S.No.	Resistivity in Ωm	Formation
1	<10	Clayey sands/Highly weathered formation
2	10-60	Weathered formations
3	61-150	Lateritic gravel/Semi weathered/Fractured formation
4	>150	Hard rock

The results of majority of sounding curves (Table 1) reveal that the resistivity of the first layer varies in the range 10 ohm-meters (Ωm) to 150 Ωm with a thickness between 0.5 to 5 meters. The NW part of the study area covered by migmatites is characterized by high resistivities of the order of 239-13629 Ωm . Second layer resistivity varies mostly between 5-50 Ωm with thickness in the range of 2-20 m, where as third layer up to 30m depth, comprises of semi fractured/fractured rock (50-150 Ωm). The fourth layer between the depths of 8-30 m forms the basement with a very high resistivity ($>150 \Omega\text{m}$). Most of the central part of the study area revealed weathered rock and high density of lineaments (Figure 1). The resistivity of this zone is less than 60 Ωm , which could be the

source for water though the thickness of the aquifer is less than 20 m and depth to the water table is less than 5 m.

The pseudo-sections (apparent resistivity cross section) and inferred lithology sections (interpreted from the VES data are drawn by connecting the soundings located along straight lines AA', BB', CC', DD', EE', FF' (Figure 1), are shown in figure 3. Fence diagrams for five regions (Figure 1) reveal the three dimensional view of the lithology of the study area. The first three fence diagrams (Fence-1, 2, 3) are drawn based on six VES points and fences 4 and 5 are based on eight VES locations (Figure 1).



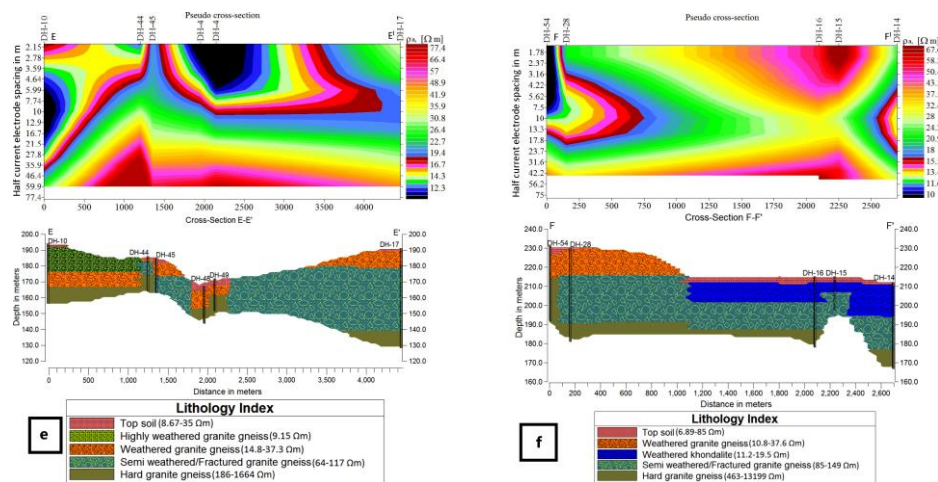


Figure 3. Pseudo-sections (apparent resistivity cross section) (Top) and lithology (bottom) sections along (a) AA`, (b) BB`, (c) CC`, (a) DD`, (e) EE` and (f) FF`. Lithology sections are drawn from the interpreted results of VES points and lithology of the nearby observation wells. Vertical scale in meters is above mean sea level (MSL) and positive upwards for lithology section.

(i) Section AA`

Along this 560 m long NW-SE profile, pseudo-section and lithology sections are plotted (Figure 3a). The topography of this section varies between 269 and 272m above mean sea level (amsl) (Figure 3a). The aquifer resistivity varies between 13.2 to 35.4 Ωm while the hard rock resistivity is more than 240 Ωm. The combined analysis indicates shallow water table at 1 to 4 m depth with aquifer thickness varying between 6 and 15 m which is underlain by hard rock. The scope for groundwater potential is less since this area is covered by migmatitic rocks which are a poor aquifer, and further due to the less weathered zone thickness.

(ii) Section BB`

This section passes through the VES points DH-38, DH-39, DH-40, DH-47 and DH-46 and runs along a steep gradient with a length of 2.8 km and runs along W-E direction with the surface topography from 110 m amsl on the western side (B) and 160 m amsl on the eastern side (B`)

(Figure 3b). Three layers corresponding to highly weathered, weathered and semi weathered Khondalite are inferred along this section above hard basement of khondalite rocks. Towards the downhill side (DH-38, DH-39), the water table is shallow (<5m) and extends up to a depth of 18 m. Towards the other end of the section (B`), the thickness of the aquifer is about 30 m and surprisingly, the water table is shallow (<2 m) in spite of a higher elevation at this point. Fractured/Semi-fractured rock is dominant source of water here.

(iii) Section CC`

This section of about 780 m length runs in NW-SE direction with a gentle slope from 127 to 123 m (Figure 3c). The weathered khondalite formation with resistivity range from 16.9 to 27.9 Ωm extends all along the section with varying thickness from 3.7 to 9 m. Another layer showing a resistivity of 63.3 to 102 Ωm extends up to about 600 m from point C to DH-35 may represent the semi weathered/fractured granite gneiss underlain by granite gneiss of high resistivity (>250 Ωm).

(iv) Section DD`

The dominant formation along this section is weathered granite gneiss showing resistivity from 11.6 to 49.8 Ωm covering the entire length of the section of 765 m (Figure 3d). The thickness of this layer is varying from 3.8 m at DH-61 to 21.5 m at DH-18. The gradient along this section is gradually increasing from D (168 m) to D` (208m). Since the locations of DH-23, DH-61 and DH-62 are close to hillock, hard rock of high resistivity (316-340 Ωm) is encountered at shallow depth of 5-10 m. The thickness of the weathered zone is 24 m (32.7 Ωm) at DH-18 and about 14 m at DH-8 as inferred from lithology of the nearby well at Jaddangi.

(v) Section EE`

The length of this NE-SW section is about 4.8 km (Figure 3e). Litholog from the well at Bornagudem is taken as a base to infer the geology of the area. The aquifer of this section is weathered granite gneiss of resistivity ranging from 14.8 to 37.3 Ωm all along the section. The thickness of this layer is varying from 2.5 to 11 m at DH-17, DH-44 and DH-45, which is underlain by semi weathered/fractured granite gneiss with resistivity ranging from 64-117 Ωm . A layer with resistivity of 64 $\Omega\text{ m}$ inferred below weathered granite gneiss at DH-17 with a thickness of 41 m could be a potential zone in this section.

(vi) Section FF`

The topography of this section varies between 215 m and 230 m amsl (Figure 3f). The litholog of the soundings at DH-54 and DH-28 are inferred based on the lithology of the well at Kindra. Weathered granite gneiss which forms the aquifer along this section with a thickness of 12 m (10.8-37.6 Ωm) is revealed at DH-54 and DH-28 while at DH-14, DH-15 & DH-16, weathered khondalite of resistivity ranging from 11 to 20 Ωm with varying

thickness from 5 to 16 m forms the aquifer. This aquifer is underlain by semi weathered/fractured granite gneiss of resistivity ranging from 84.9 to 149 Ωm with a thickness from 14 to 25 m. Since the sounding DH-54 was carried out near hill, the hard rock basement is encountered at shallow depth 17 m.

(vii) Fence Diagrams

To view the aquifer in three dimensions, fence diagrams at possible locations have been generated based on the VES results and lithologs of wells occurring near sounding points. The locations of these fence diagrams are shown in figure 1. The fence diagrams are shown in figure 4. Fence-1 covers an area of 0.14 sqkm including six soundings (DH-4, 5, 6, 57, 58 and 59) in the NE part of study area (Figure 4a). In this region, lithologs are available for the wells at Appannapalem and Sarabhavaram (two wells) villages (Figure 2). In this region, lithology section along AA` is also shown in figure 3a. It is clear that weathered granite gneiss up to a maximum depth of 18 m forms the major aquifer in this region underlain by hard granite gneiss.

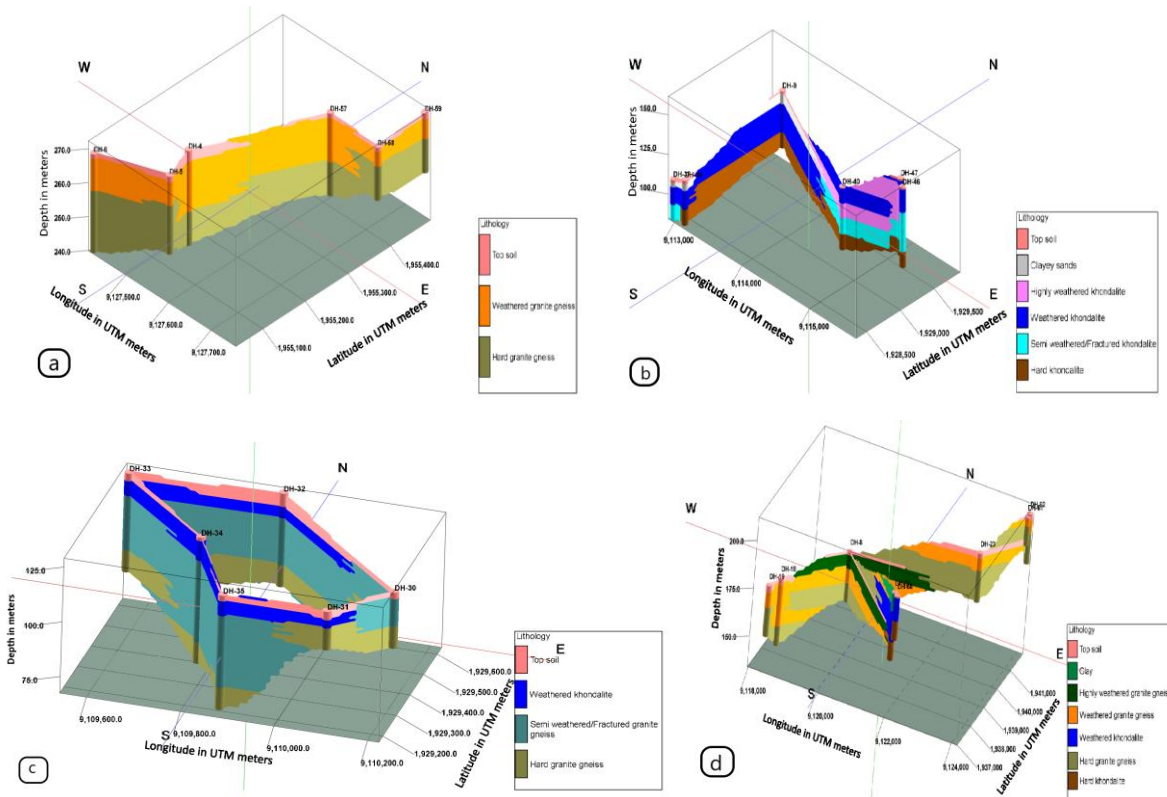
Fences 2 and 3 are located in the southern part of study area. Fence-2 is based on six sounding points DH-9, 38, 39, 40, 46 and 47 covering an area of 3.2 sqkm (Figure 4b). Lithology section along BB` (Figure 3b) of this region shows weathered khondalite as the major aquifer in addition to highly weathered khondalite zone, as observed at DH-40, 46 and 47. Semi weathered khondalite, with a thickness in the range of 10 to 20 m forms the major source for storing groundwater.

Fence-3 diagram (Figure 4c) is drawn connecting VES locations DH-30, 31, 32, 33, 34 and 35 and it covers an area of 0.28 sqkm. The lithology of a well in Thimmapuram village (Figure 2) is taken as basis to infer the geology of the region.

Lithology section along CC` shows that, the weathered layer thickness of this area is less than 8 m.

The major source of groundwater in the region is semi-weathered/fractured rock of about 22-30 m thickness with a resistivity between 60 to 100 Ω m covering the VES locations DH-32, 33, 34 and 35. However, at locations DH-30 and 31, the hard rock/basement is encountered at a very shallow depth of 7.5 – 15m. Fence-4 is based on eight soundings DH-8, 18, 19, 23, 61, 62, 67 and 68, covering an area of 19.186 sqkm (Figure 4d) with varying topography between 168 and 208 m amsl. Based on the Lithology section along DD` and lithologs at the wells in Jaddangi, Vanakarayi and Yerrampadu, weathered granite gneiss is the major aquifer with a maximum thickness of the aquifer is about 24 m at DH-18. At other locations, the water table is very shallow (0.75-3 m) and thickness of this aquifer layer is also less than 10 m. However, at locations DH-67, the weathered rock

(Resistivity 45 Ω m) shows a considerable thickness of 15 m below the highly weathered granite rock. Granite formations are inferred at Jaddangi and Yerrampadu, while khondalite formations are inferred at Vanakarayi. Weathered formations of both these rock types may form the groundwater potential zones of this region. Fence-5 shows very steep topography with elevation varying from 325m (DH-25) to 208m (DH-22), covering eight soundings (DH-7, 20, 21, 22, 25, 26, 27 and 41) (Figure 4e) over an area of 47.12sqkm. The lithology of the six wells at Addateegala (4 wells), Nimmalapalem and Vedhunagaram villages is taken as base to infer the geology of the area. Weathered khondalite could be the source of aquifer (DH-25 and 27) in elevated region of this fence while the weathered granite gneiss followed by semi weathered/fractured granite gneiss form the major aquifers with less thickness (5.35 m) in low-lying portion.



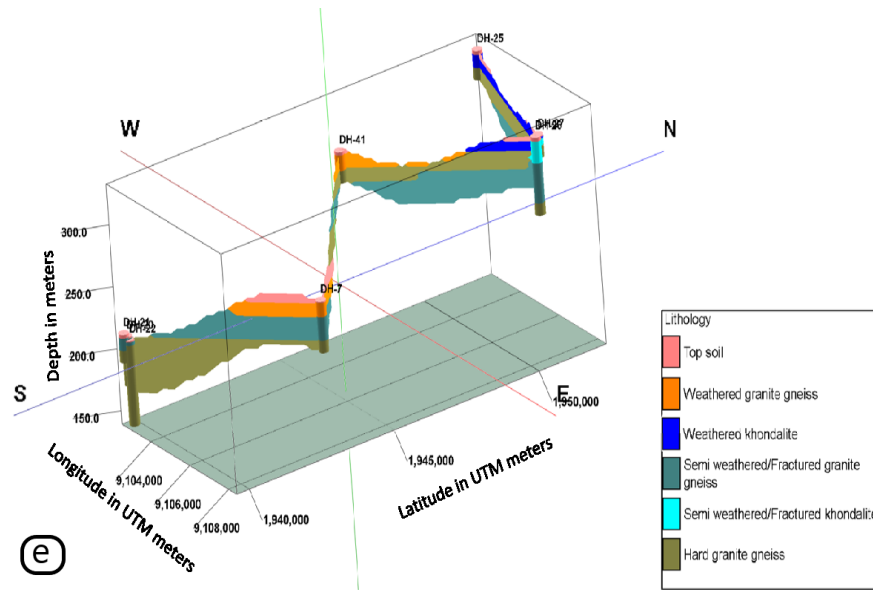


Figure 4. Fence diagrams for the regions showed in study area map (a) Fence 1 (b) Fence 2 (c) Fence 3 (d) Fence 4 and (e) Fence 5. Vertical scale in meters is with reference to mean sea level (MSL) and positive upwards.

About 33 sounding points could not be included in the geoelectric or fence diagram analysis, as they are not in proximity to these regions. From these 33 locations, 11 locations (DH-1, 2, 3, 7, 24, 29, 36, 43, 50, 69, and 70) may prove to be the good potential zones as revealed by the resistivities in the range of 12-141 Ωm and thickness above 19m (Table 1). DH-1, 2 and 24 show both weathered (9-20 m) and semi weathered layers (20-50 m). At DH-36, about 29 m of weathered khondalite is inferred as third layer. At 7 locations (DH-29, 42, 43, 50, 56, 69 and 70), the thickness of the semi weathered layer varies in the range of 12 to 50 m.

SUMMARY AND CONCLUSIONS

Analysis of the VES data at 70 locations in terms of pseudo and lithology along six sections (2D) and five fence diagrams (3D), revealed the zones of weathered and semi weathered layers, where in the former contains groundwater potential zones with thickness of around 10 to 15 m, with the exception of area of fence-3 where the aquifer thickness is about 30 m in an area of 0.245sqkm. It is inferred from this analysis that the zone with

resistivity less than 60 Ωm is a good source for exploration of ground water. Contour map of figure 5a shows the spatial distribution of weathered formation/highly fractured (resistivity less than 60 Ωm) of varying thickness. It can be inferred from density of lineaments in the study area (Figure 5a and b) and from spatial distribution of weathered zone; about 308 sqkm of central part of the study area with an average thickness of 15 m is the better source of aquifer. About 120 sqkm in the NW and eastern parts of the study area shows a weathered layer with an average thickness of 7 m. It can easily be observed that depth to the weathered layer is less than 6 m in the entire area (Figure 5b) with a thickness of about 6-20m. Below this weathered zones, semi weathered zone is present in regions of fence-2 and 3 which is also a good source of aquifer. Thus, the study has clearly shown its efficacy in revealing the influence of lineaments on the thickness of weathered zones and delineation of the potential zones of groundwater in the central part of the study area compared to the other parts.

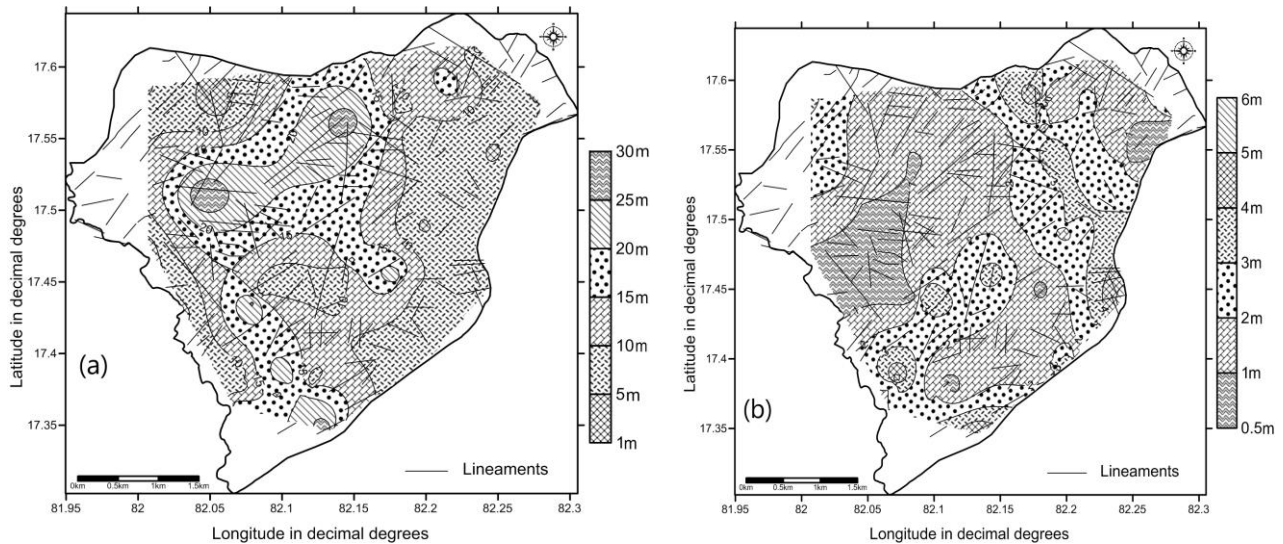


Figure 5. Spatial distribution maps of (a) aquifer thickness (Resistivity of aquifer is less than $60 \Omega\text{m}$) (b) Over burden (resistivity is more than $60 \Omega\text{m}$) thickness above the aquifer in (a). (Solid lines indicate lineaments)

ACKNOWLEDGEMENT

The first author acknowledges the financial support from UGC through Rajiv Gandhi National Fellowship, New Delhi. Anonymous reviewer's suggestions are gratefully acknowledged.

Compliance with Ethical Standards

The authors declare that they have no conflict of interest and adhere to copyright norms.

REFERENCES

Bobachev, A.A., Modin, I.N. and Shevnin, V.A., 1990-2002. Moscow State University Geophysical faculty, Department of Geophysics developed IPI2Win with copyright to authors and distributed by Geo Scan-M Ltd, Moscow, Russia. (<http://geophys.geol.msu.ru/ipi2win.htm>)

Ashraf, M.A.M., Yusoh, R., Sazalil, M.A. and Abidin, M.H.Z., 2018. Aquifer characterization and groundwater potential evaluation in sedimentary rock formation. IOP Conf. Series: J. Phys., Conf. Series 995 (2018) 012106. doi:10.1088/1742-6596/995/1/012106.

Bhimasankaran, V.L.S. and Gaur, V.K., (eds) 1977. Lectures on exploration geophysics for geologists and engineers. Assoc. Expl. Geophys., Centre of Exploration Geophysics, Hyderabad, India.

Keller, G.V. and Frischknecht, F.C., 1966. Electrical methods in geophysical prospecting. Pergamon, London, pp. 517.

Orellana, E. and Mooney, H.M., 1966. Master tables and curves for vertical electrical sounding over layered structures. Interciencia, Madrid, Spain, pp: 150.

Prasanna, M.V., Chidambaram, S., Shahul Hameed, A. and Srinivasamoorthy, K., 2009. Study of evaluation of groundwater in Gadilam basin using hydrogeochemical and isotope data. J. Environ. Monit. Assess., 168, 63-90. doi: 10.1007/s10661-009-1092-5.

Syedmohammadi, J., Esmaelnejad, L. and Shabanpour, M., 2016. Spatial variation modeling of groundwater electrical conductivity using geo-statistics and GIS. Model. Earth Syst. Environ. 2(4), 169 (Chicago).

- Srinivasamoorthy, K., Vasanthavigar, M., Vijayaraghavan, K., Sarathidasan, J. and Gopinath, S., 2013. Hydrochemistry of groundwater in a coastal region of Cuddalore district, Tamilnadu, India: implication for quality assessment. *Arab. J. Geosci.*, 6(2), 441–454.
- Srivastava, P.K. and Bhattacharya, A.K., 2006. Groundwater assessment through an integrated approach using remote sensing, GIS and resistivity techniques: a case study from a hard rock terrain. *Inter. J. Remote Sens.*, 27(20), 4599–4620.
- Subrahmanyam, M. and Venkateswara Rao, P., 2017. Delineation of groundwater potential zones using geo-electrical surveys in SSW part of Yeleru river basin, East Godavari District, Andhra Pradesh. *J. Ind. Geophys. Union*, 21(6), 465-473.
- Vasantrao, B.M., Bhaskarrao, P.J., Mukund, B.A., Baburao, G.R. and Narayan, P.S., 2017. Comparative study of Wenner and Schlumberger electrical resistivity method for groundwater investigation: a case study from Dhule district (M.S.), India. *Appl. Water Sci.*, 7(8), 4321–4340.
- Venkateswara Rao, P., Subrahmanyam, M. and Ratnakar, D., 2019. Performance evaluation of different interpretation techniques of vertical electrical sounding data. *J. Ind. Geophys. Union.*, 23(1), 55-68.
- Zohdy, A.A.R., 1989. A new method for automatic interpretation of Schlumberger and Wenner sounding curves. *Geophysics*, 54(2), 245–253.

Received on: 13.5.19; Revised on: 23.7.19; Accepted on: 1.8.19

Structural Interpretation and Automated Extraction of the Digital Terrain Model of a Rock Mass by an Irregular Triangulated Network: A Case Study from Boboyo (Cameroon)

Jean Jacques Nguimbous-Kouoh^{1,2}, Thomas D'Aquin Biyindi² and Eliezer Manguelle-Dicoum³

¹Department of Mines, Petroleum, Gas and Water Resources Exploration, Faculty of Mines and Petroleum Industries, University of Maroua, Kaele, Cameroon.

²Department of Mines and petroleum, University of Science and technology of ethics, Yaounde, Yaounde, Cameroon

³Department of Physics, Faculty of Science, University of Yaoundé I, Yaoundé, Cameroon.

*Corresponding author: nguimbouskouoh@yahoo.fr

ABSTRACT

Isolated rock masses in the far north-Cameroon are the place of rock-falls and landslides that threaten the lives of local residents. The description of their rock matrices and the discontinuities observed is an essential phase in their understanding for further future exploitation. The main aims of this study are: the petrographic, geotechnical and structural characterization of the Boboyo rock-mass (Cameroon); the mapping of the fracture network of the site using satellite data SRTM; and the morpho-surface evaluation of the rock-mass. The field campaigns were carried out on a scale between 1/100 and 1/1000. They enabled to identify the occurrence of plagioclase, microcline, biotite and oxides distributed on the site, confirming the granitic nature of the rock-mass. The classification of the samples by the geotechnical tests, took into account the five-point compensation rule, introduced by the NFP18-545 standard. Thus the Los-Angeles and Micro-Deval tests gave respective values of 31.8% and 10.3%. The samples showed a resistance to dynamic fragmentation of 23.10%. The Digital Terrain Model (DTM) was obtained from a triangulated irregular network (TIN). It allowed modeling, analyzing and visualizing the phenomena related to the topographic surface. The map of the lineaments showed on the structural plane, 162 lineaments distributed in a principal direction N-S and two preferential directions N-S and E-W, which represent the set of brittle structures (fracture, diacalse, vein, paraclase) attributed to a phase of intense deformation of the rock-mass. The total length of the lineaments is 11279.83 m, with maximum length of a lineament at 1443.5 m, and mean length of lineament about 352.49 m. The morpho-surface automatic extraction enabled to estimate the area of the already exploited rock-mass at approximately 23730.774 m² and the unexploited area at approximately 271317.655 m².

Keywords: Rock-mass, Petrography, Geotechnical testing, MNT, TIN. Boboyo, Cameroon

INTRODUCTION

The rock-mass often result from a long, complex geological history, which includes a phase of material formation by deposition and consolidation in the case of a sedimentary rock and crystallization in the case of a magmatic rock (Coggan et al.1998). They can also result from one or more phases of tectonic deformation with formation of folds and faults or metamorphic transformations (foliation, recrystallization), and finally from a period of meteoric weathering for the parts close to the surface (Coggan et al., 1998; El-Naqaand Kuisi, 2002; Lemy et al., 2003; Sen

and Sadagah, 2003; Singh and Rao, 2005; Zhang, 2005; Tomás et al., 2007). Rock-mass are very complex structures, formed by a juxtaposition of heterogeneous materials. They are likened to an assemblage of blocks called rock matrix that are delimited by discontinuities consisting of cracks, fractures or faults. To know their components and structures, there are several methods, conventional as well as advanced (Coggan et al., 1998; Lemyet al., 2003; Singh and Rao, 2005; Tomás et al., 2007; Aksoy, 2008; Lato et al., 2009; Zhang, 2010; Tomás et al., 2012; Akin, 2013; BertuSzzi et al., 2016; Kunui-Hong et al., 2017; Vitthaland

Arup, 2018) that include sampling, laboratory testing and field testing, etc. The study of a rock-mass comprises at least one of the following phases: a global geological characterization of the deposit, a geostructural characterization of the mass and the geomechanical characterization of the rock matrix. These different characterizations can allow on the one hand, to qualify the fragility of the rock versus to an explosive constraint and on the other hand, to qualify the mechanical characteristics of the materials that will be slaughtered, these materials being used in the context of embankment projects or in the production of aggregates.

The problem of the rock-mass of the extreme north-Cameroon is that they are abandoned and undergo a significant anthropogenic and physical degradation. They are the place of rock-falls and landslides that threaten the lives of local residents. This study is an attempt to allow a better knowledge of these aspects for future use of materials from these rock-mass in the construction of roads and other structures, such as bridges and dams. The aims of this study are to characterize rocks through petrographic, geotechnical and structural manner in order to propose a digital terrain model and a fracturing map that can model, analyze and visualize phenomena and discontinuities, related to the topographic surface of the rock-mass and to further evaluate morpho-surface evaluation of the rock-mass by TIN.

GEOLOGIC SETTING

The geological history of the Far North-Cameroon (Figure 1a) is closely related to that of the Lake Chad basin (Dumort and Péronne, 1966; Louis, 1970; Ewodo-Mboudou et al., 2017). In this region, deposits are dependent on a succession of regressions and transgressions, caused by the alternation of arid and rainy periods (Dumort and Péronne, 1966; Ewodo-Mboudou et al., 2017;

Ngounou-Ngatcha, 1993; Ngounou-Ngatcha et al., 2001; Ngako et al., 2003; Penaye et al., 2004). The major structural directions encountered in the far north (Ewodo-Mboudou et al., 2017; Ngounou-Ngatcha et al., 2001; Penaye et al., 2004; Tchameni et al., 2006; Penaye et al., 2006; Ngako et al., 2008; Njanko et al., 2010; Ganwa et al., 2011) are N12°E and N28°E: Cameroon volcanic line; N58°E: Somalia direction; N73°E: Adamawa line; and N117°E, N135°E to 142°E: Eritrean direction. These directions control the folding of crystallophyllian rocks, faults, the hydrographic network, the location of volcanic and subvolcanic centres, and post-tectonic intrusive massifs. Most of them are very old and have been reactivated during the local geological evolution, which are integrated with the structural framework of the Far North (Ewodo-Mboudou et al., 2017; Ngounou-Ngatcha et al., 2001; Penaye et al., 2004; Tchameni et al., 2006; Penaye et al., 2006; Ngako et al., 2008; Njanko et al., 2010; Ganwa et al., 2011).

The Far North (Figure 1a) is represented by sedimentary formations, Precambrian crystalline basement and volcanic formations (Dumort and Péronne, 1966; Louis, 1970; Ewodo-Mboudou et al., 2017). In this region, sedimentary formations extend from the bottom of the Mandara Mountains to the eastern Diamare plain. The thickness of the sedimentary cover varies from a few meters at the foothills to several tens of meters at Lake Chad (Dumort and Péronne, 1966; Louis, 1970; Ewodo-Mboudou et al., 2017). These include alluvia from Logone and Mandara Mountains, lacustrine clay and ancient sands. The Precambrian crystalline basement outcrops continuously in the western mountainous areas, the Southeast peneplain and sporadically in inselberg in the central zone (Dumort and Péronne, 1966; Louis, 1970; Ewodo-Mboudou et al., 2017). The basement (Dumort and Péronne, 1966; Ewodo-Mboudou et al., 2017;

Ngounou-Ngatcha et al., 2001; Penaye et al., 2004; Tchameni et al., 2006; Penaye et al., 2006; Ngako et al., 2008; Njanko et al., 2010; Ganwa et al., 2011) consists of an epi-metamorphic complex covering about 100% of its surface and forming a band north of Maroua; a migmatitic meso-metamorphic ensemble covering about 50% of the basement surface and forming with the granites in all of the Mandara Mountains; a non-migmatitic meso-metamorphic ensemble covering 10% of the surface of the basement outcrop in the Kaele peneplain and Moutourwa (Figure 1a).

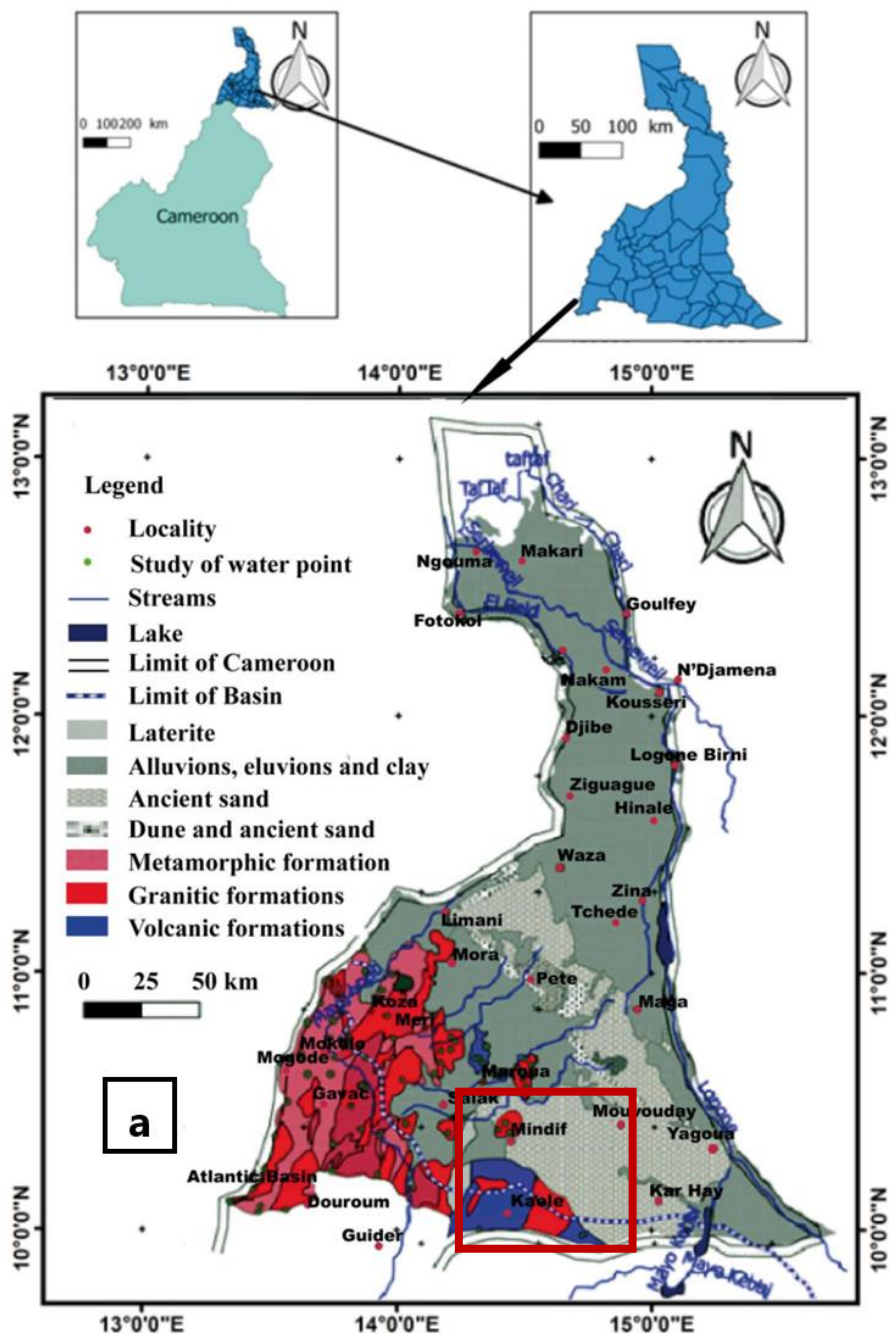
Further, the sedimentary rocks such as alluvium, clay, limestone and sandstone constitute most of the geology of the Far North (Dumort and Péronne, 1966; Ewodo-Mboudou et al., 2017; Ngounou-Ngatcha et al., 2001; Ganwa et al., 2011; Moussa, 2011; Kouske et al., 2012; Moussa et al., 2012). These deposits follow the rivers of the province, such as Logone and Mayo Tsanaga, which flow into Lake Chad in the north. In the south of the province, a strip of granite separates the sedimentary zone from an area of metamorphic rock located to the southwest. The latter region includes deposits of gneisses, mica and shale (Figure 1a). The Rhumsiki Valley, a mountainous field littered with extinct volcano cores, is a small area of volcanic rock, such as trachyte and rhyolite. Soils in the far north are a bit more complex. Much of the province is made up of young soils, rich in raw minerals. This is the case for much of the land south of Lake Chad and the Mandara Mountains on the western border with Nigeria (Penaye et al., 2004; Tchameni et al., 2006; Penaye et al., 2006; Ngako et al., 2008; Njanko et al., 2010; Ganwa et al., 2011; Moussa, 2011; Kouske et al., 2012; Moussa et al., 2012). Here, the soil is made of black clay (alluvial soil). The seasonal floods of the Logone River give rise to a north-south band of hydromorphic soils on the Chadian border. The rest of the territory, the plain

of Diamare and the valley of the river El Beïd, consists of ferruginous soils. Seasonal wet/dry variations in the province create relatively shallow, ferrous or lateritic soils (Penaye et al., 2004; Tchameni et al., 2006; Penaye et al., 2006; Ngako et al., 2008; Njanko et al., 2010; Ganwa et al., 2011; Moussa, 2011; Kouske et al., 2012; Moussa et al., 2012).

In terms of relief, most of the far north has a relatively low altitude. This lower part is part of the Chad plain and its gentle slope varies from about 500 meters southwest to 200 meters at the edge of the Logone. The average elevation of this basin is 280 meters (Figure 1a). The Diamare plain occupies the lower third of the Chadian plain and is characterized by a number of isolated inselbergs. The Mandara Mountains on the southwestern border with Nigeria, form the highest point, between 500 and 1000 meters above sea level, with an average of about 900 meters (Penaye et al., 2004; Tchameni et al., 2006; Penaye et al., 2006; Ngako et al., 2008; Njanko et al., 2010; Ganwa et al., 2011; Moussa, 2011; Kouske et al., 2012; Moussa et al., 2012) Mount Tourou is the highest point at 1442 meters. These mountains are formed probably due to the same tectonic activity that caused the Benue depression in the Northern Province. The area was once volcanically active, as evidenced by a number of trachyte and rhyolite necks of extinct volcanoes. The most spectacular of them is in the valley near the tourist village of Rhumsiki. The part of the chain located in the far north is on a medium plateau, located between 800 and 900 meters. Isolated mountains continue in the Diamare plain, at Mindif, Boboyo, Kaele and Lara. The northern extent of these mountains is dissected by several rivers (Penaye et al., 2004; Tchameni et al., 2006; Penaye et al., 2006; Ngako et al., 2008; Njanko et al., 2010; Ganwa et al., 2011; Moussa, 2011; Kouske et al., 2012; Moussa et al., 2012).

The Mayo-Kani region (Figure 1b) is covered with sedimentary formations and magmatic formations represented by a set of isolated and chaotic rock masses. The generally recorded geological formations are (Wambara et al., 2017), granites, sandy clay, micaschists, clay sands, laterite, basalts and rhyolites. On the study site,

the major geological formation encountered is granite. This formation is in the form of a slab at the top and a block on the hillsides. The massif thus leaves a chaotic appearance in the environment. This massif is bounded by a mountain range whose average altitude varies between 400 and 460 m (Wambara et al., 2017).



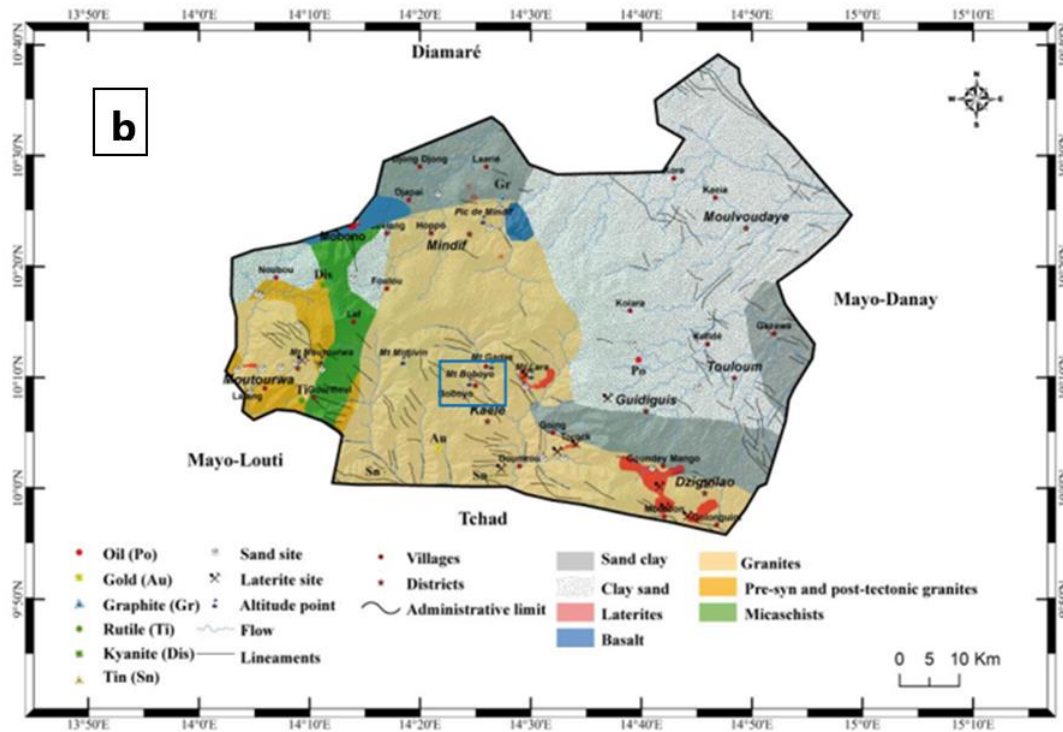


Figure 1. (a) Geological map of the Far-north of Cameroon (from Dumort and Péronne, 1966; Louis, 1970; Ewodo-Mboudou et al., 2017), with the red frame denoting Mayo-Kani zone. (b) Geological map of Mayo-Kani (from Wambara et al., 2017), the study site is framed in blue.

METHODOLOGY

A field campaign was mounted to collect geological, geometric and GPS data, in order to identify the type of rock mass, the different facies and the outcrop mode. The equipment used in the field and in the laboratory consisted of a GPS receiver and a topographic map for the geographical location of the site, a laptop for data processing, a digital camera for taking pictures, a hammer for taking samples, a graduated seal to assess the density of the samples and an electron microscope for the observation of thin sections. Cartographic data processing was carried out by GIS software's (basecamp v.4.2.1; google earth pro v.7; global mapper v.17; surfer v.14; argisv.10.4; adobe illustrator (cs4) v.14).

Methods of characterizing the rock-mass

The recognition of the rock mass consisted identifying the materials present, taking samples

for laboratory study, identifying discontinuities on site, their characteristics and density. The geological survey was conducted at a scale of 1/100 to 1/1000, to locate the main outcrops and associated observations.

Petrography

Petrography describes the rocks from a structural, textural, mineralogical and chemical point of view. The observations were made using a scanning electronic microscope. We made sure that the samples used are representative of the training; the glass slides used have perfect flatness to be glued together with the resin layer as thin as possible. The procedure was to gradually reduce the thickness of the blade until it became transparent. For this, a grinder was used with a diamond abrasive device. All this has allowed to gradually reducing the rock in steps of 5 to 10 micrometers. Once the rock has reached a thickness of 60 to 80 micrometers, a lapse on

lapidary is again performed, to lower the thickness of the rock to 30 microns (less than a third of the thickness of a hair). With silicon carbide abrasive powders, the thickness of the rock has been reduced very slowly, frequently checking the progress of the running-in process (Wambara et al., 2017).

Geotechnical tests

The Los-Angeles test was used to measure the combined resistance of shock fragmentation and mutual friction wear of aggregate elements. It applies to aggregates used for the construction of the roadbed, including wearing courses. The material evolves during the test, on the one hand as a result of the impact of the pellets on the aggregate (brittle fracture of the elements), on the other hand by friction of the elements on each other, on the cylinder of the machine and on the balls (Vavrek, 2004; Thuro et al., 2006; Nilsen et al., 2007; Yarali et al., 2008; Brandes and Robinson, 2006). The test consists of measuring the quantity of elements less than 1.6 mm, produced by subjecting the material to the impact of standardized balls and mutual friction in the Los-Angeles machine. The granularity of the material under test is selected from six standard granularities, of the granular class 4/6.3 mm, 6.3/10 mm, 10/14 mm, 10/25 mm, 16/31.5 mm and 25/50 mm, getting as close as possible to the granularity of the material as it will be implemented. The weight of the ball charge, varied depending on the type of granularity. If P is the material under test, p the weight of the elements less than 1.6 mm produced during the test, the combined resistance to shock fragmentation and reciprocal abrasive wear is expressed in the quantity (Vavrek, 2004; Thuro et al., 2006; Nilsen et al., 2007; Yarali et al., 2008; Brandes and Robinson, 2006): $C_{LA} = 100 p/P$: this

dimensionless quantity is called the Los-Angeles coefficient of the material. With $p = P - P'$, where P' is the result of the weight of refusal-weigh.

Similarly, the Micro-Deval test was used which enables to determine the resistance to wear, by mutual friction of the elements of an aggregate. The material evolves during the test by friction of the elements on each other, on the cylinder of the machine in rotation and on the balls (abrasive load) dry or in the presence of water. The granularity of the material under test is selected from the granular classes: 4-6.3 mm, 6.3-10 mm, 10-14 mm and 25-50 mm. For tests carried out on chippings between 4 and 14 mm, an abrasive load is used. If M is the mass of the material under test, m the mass of the elements below 1.6 mm produced during the test, the wear resistance is expressed by the Micro-Deval coefficient which is written (Kline et al., 2007) as $C_{MD} = 100 m/M$, with M mass of the sample between 500 to 10000g according to the chosen class; m the sieve mass of 1.6 mm and the mass of refusal-weigh. At the end, the result will be rounded to the unit and the measured coefficient will be in percentage of wear. The smaller it is, the greater the wear resistance will be.

Method of Extracting the DTM and Surface of the Site

Data Collection

The adaptive sampling method was used to collect longitude, latitude, and elevation data on Google Earth, and then combined with GPS field data. All of this data has been imported into GIS to create a digital terrain model (DTM) across a TIN and plot the mass points of the previously exploited and untapped areas of the site. The GML data format was used to make the data interoperable (Wambara et al., 2017).

Triangulated Irregular network method

To obtain the DTM and evaluate the surface of the rock mass, the triangulated irregular network method (TIN) was carried out. A TIN is a topological data structure that manages information about the nodes constituting each triangle and the neighbors of each triangle. Figure 2 shows the topology of a simple TIN. A TIN can conveniently be stored in a database file or table with other topological data structures. The data structure of the TIN includes, the number of the triangle, the number of each adjacent triangle, the three nodes defining the triangle, the coordinates (x, y) of each node, the area and the z value of each node. The effectiveness of the triangulation algorithm depends on the generator of the triangular mesh. Triangulation includes two main techniques for generating a TIN (Wambara et al., 2017; Tsai, 1993; Zhang and Montgomery, 1994; Jones et al., 1994; Williams et al., 2000; Tucker et al., 2001b; Jingsong and Kevin Amaratunga, 2003; Jim-casaer et al., 2010):(i)The selection of mass points and their triangular facet connection. It consists of manually selecting points and links that create the triangular network and (ii)The automatic point selection during which more nodes must be stored to resolve uncertainty issues. It allows having better results because its algorithm is effective. The process remains under the control of the human operator.

Delaunay's triangulation dictates that when a circle is generated by three nodes around a triangle, there is no longer another node within that circle. Considering Figure 3 we can start from a set (S) of non-collinear points in the plane (Tsai, 1993; Zhang and Montgomery, 1994; Jones et al., 1994; Williams et al., 2000; Tucker et al., 2001b; Jingsong and Kevin Amaratunga, 2003; Jim-casaer et al., 2010). The triangulation $T(s)$ consists of dividing the plane into a maximum set

of triangles with the restriction that each edge of the triangle, with the exception of those defining the convex hull of (S), be shared by two adjacent triangles. The triangulation $T(s)$ of Delaunay is a unique triangulation built on (S) so that any arbitrary circle of triangles contains no other point of (S). This condition, often also considered an empty circle property, optimizes the triangulation based on the minimum internal angle of the triangles. Triangles of the Delaunay triangulation $T(s)$ are considered Delaunay triangles (or legal triangles) and their surroundings as Delaunay circles (Tsai, 1993; Zhang and Montgomery, 1994; Jones et al., 1994; Williams et al., 2000; Tucker et al., 2001b; Jingsong and Kevin Amaratunga, 2003; Jim-casaer et al., 2010). For example in Figure 2, in the triangle T1, the nodes p1, p2, p6 are surrounded by the circle c1 (blue circle) and no other node is located inside this circle. Similarly, in the triangle T2, the nodes p2, p3, p6 are surrounded by the circle c2 (green circle) and no other node is inside this circle and in the triangle T3, the nodes p3, p4, p5 are surrounded by the circle c3 (red circle) and no other node is inside this circle. The condition for Delaunay's triangle is fulfilled.

Nodes, edges and triangles are the major components of a TIN; the other components are hulls, fracture lines and defects. In this article, we consider only the main components.

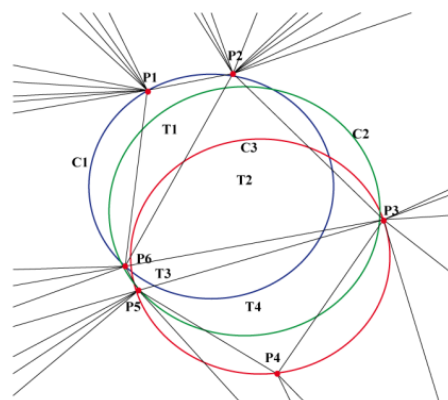


Figure 2. The topology of a TIN with Delaunay's.

RESULTS AND DISCUSSION

Photo-interpretation

The use of photo-interpretation often enables to significantly improve the results of research in the field of engineering geology, by allowing to better situate the problems, to integrate them into the environment, and to optimize the results. More detailed research leading to a better exploitation of a site (Penaye et al., 2004; Tchameni et al., 2006; Penaye et al., 2006; Ngako et al., 2008; Njanko et

al., 2010; Ganwa et al., 2011; Moussa, 2011; Kouske et al., 2012; Moussa et al., 2012). Photo-interpretation helps to better define the study site; to have a good approach to topographical, geological, surface water circulation and vegetation problems; and guide the field study. Figure 3 shows the morphological configuration of the site consisting of block-rocks (plate A), slabs (plate B), frontage (plate C) and the various artisanal exploitation sites (plate D).



Figure 3. A: Block-rock; B: Slab, C: frontage and D: Collection of aggregates at the Boboyo site.

Petrographic results

The petrographic description consists of determining the nature of the different minerals, their relative abundance, their degree of alteration, their size and their arrangement, as well as the possible existence of pores (Penaye et al., 2004;

Tchameni et al., 2006; Penaye et al., 2006; Ngako et al., 2008; Njanko et al., 2010; Ganwa et al., 2011; Moussa, 2011; Kouske et al., 2012; Moussa et al., 2012). Figure 4 shows the thin plate of the rock observed under an optical microscope. The granite samples used in this study come from the

boboyo site. The microscopic observation enables to highlight the predominance of plagioclase and microcline, phenocrysts and in microcrystals, the rock has a grainy texture. The presence of all these

minerals (plagioclase, microcline, biotite, oxides) distributed on the deposit confirms the granitic nature of the rock. Table 1 summarizes microscopic observations of thin-plate images

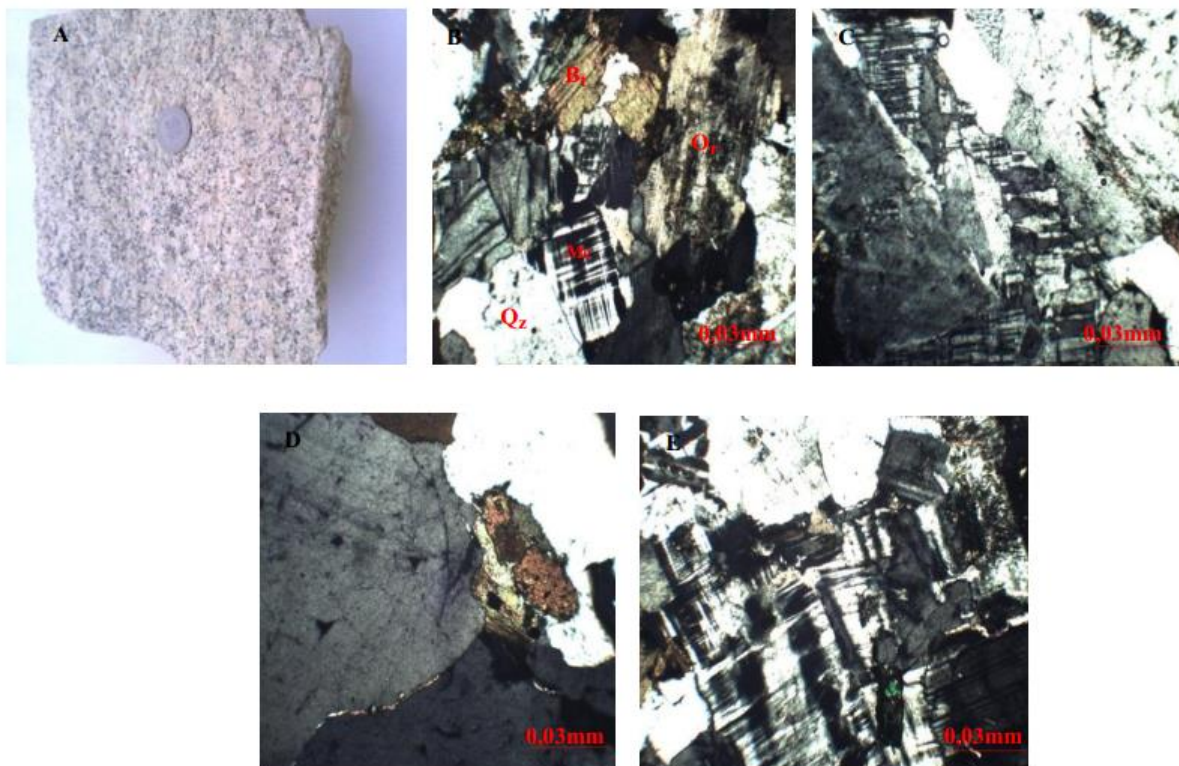


Figure 4. A. photo of the granite sample. B-C-D-E are the photomicrographs of the thin sections processed at the Kolbisson-Cameroon Geological and Mining Research Institute (GMRI).

Table 1. Summary of microscopic observations of granite.

Minerals		Quartz (Q _z)	Orthoclase (O _r)	biotite (B _t)	Microcline (M _c)	Oxide
Observations		45%	30%	10%	12%	2%
LPA	Polarization tint	Gray and white of the first order	Gray and white of the first order	Hue: second and third in longitudinal sections	First order white gray	Off
	Macles	-	Carlsbad	-	Albite and microcline	-
	Zoning	-	Present	-	Present	-
	Extinction	Rolling	-	Right	-	-

Geotechnical tests

The Los-Angeles and Micro-Deval tests were performed according to the specifications of the respective standards NFP18-573 and NFP18-572. The classification of our sample took into account

the five-point compensation rule introduced by standard NFP18-545. Thus we measured (Table 2): a LA equal to 31.8% (LA <40%) and an MDE of 10.3% (MDE <15%). What it implies is that, the material coming from the site can be used for

bituminous concrete, concrete floor for roadway layer, in aggregate for superficial armatures, which can support traffic on the axle of 13 tons. In other words, products from a quarry of this massif can be used for the construction of buildings, artworks such as roads, airports, bridges and viaducts, etc. Samples received at the laboratory

have been subjected to other tests such as density determination tests (MVR, MVA), water absorption (WA₂₄), and dynamic fragmentation resistance (DF). The measurements made on the samples (Table 2) show a material, whose average densities vary between 2.50 and 1.43 T/m³ and can withstand significant seismic velocities.

Table 2. Values obtained from the undergone tests on granites of the studied site

Testing	LA (%)	MDE (%)	MVR (T/m ³)	MVA (T/m ³)	WA ₂₄ (%)	FD (%)
Values	31.8	10.3	2.50	1.43	2.50	23.10

The digital terrain model

A Digital Terrain Model (DTM) is a digital representation of the terrain of a geographic area. There are several techniques for generating a digital terrain model (Zhang and Montgomery, 1994; Chile's and De Marsily, 1993; Chaabouni et al., 2012; Akame et al., 2013), the digitization and interpolation of level lines of topographic maps, the triangulation and interpolation of topographic surveys and the photogrammetric restitution from stereoscopic images. As part of this study, we triangulated and interpolated SRTM and GPS

topographic surveys. The digital terrain model was generated with Surfer software from four successive stages: (i) image calibration, (ii) absolute control point collection, (iii) collection of relative control points and (iv) extraction of the DTM. Figure 5 shows the obtained block diagram. It highlights a pit for the part already exploited ten years ago by the company Duclaire-Colasse and a part that shows the remaining massif outcrops. The lake is approximately 50 m deep and has a stepped structure. The GPS altitudes obtained on the site vary between 403 m and 414 m.

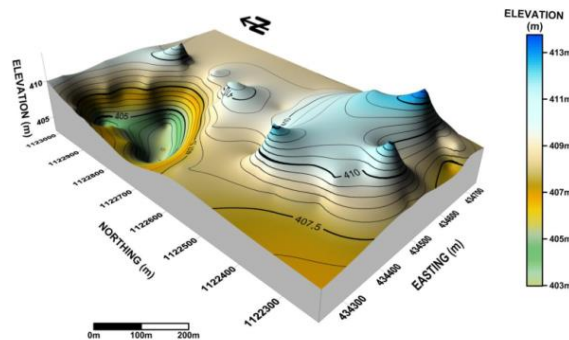


Figure 5. 3D Digital terrain model showing the location of the study site extracted from the SRTM satellite image. The projection system: WGS 84 UTM 33N; Spatial accuracy 30 m.

Geomorphological profile of the site

The geomorphological characteristics of the study area are presented by the longitudinal profile (Figure 6). The profile is NW-SE with a length of about 950 m. The maximum height is 414 m. The relief has undulations in the form of hollows and

bumps. Structurally, surface and depth rocks are hard (compressive strength > 80 MPa) consistent, compact, extremely strong, very rough and incompetent. Geotechnical tests carried out in the IRGM laboratory have revealed that the rock has a porosity of 0.01%. The lithology shows granitic

facies rocks with thicknesses varying between 50 m for deep rocks and 6 m for surface rocks.

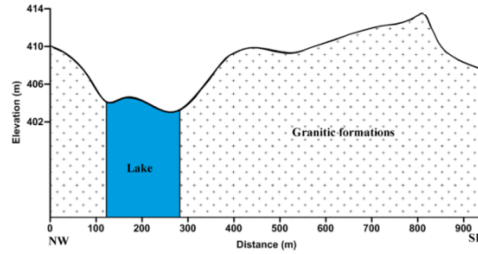


Figure 6. Geomorphologic profile of the Boboyo site. The rock matrix is defined as an intact rock volume that has homogeneous properties and is uncut by discontinuities.

The fracture map

To apprehend the fracturing of the site, the fracture representation at the site scale was carried out. This map (Figure 7) allows to have a better idea of the site and to observe the spatial arrangement of the different fractures, their hierarchization, and to fix the chronology of their appearance (Chile's and De Marsily, 1993; Chaabouni et al., 2012; Akame et al., 2013). The lineaments we observe are probably related to the gradual decompression of the rock-mass due to thermal alteration. They can also be the result of one or more mechanical actions that the massif has undergone during its tectonic history that relates to the tectonic episodes undergone by of extreme

north-Cameroon. The validation of these different linear structures was made on the basis of the geological map and field knowledge. The directional rose diagram, which is the distribution of the fracture orientation of the study site, allows us to observe the different fracturing directions. The map of lineaments thus obtained, shows on the structural case, 162 lineaments arranged in a main direction N-S; and two preferential directions N-S and E-W, which probably represent all the brittle structures (fracture, diacalse, lode, paraclase) attributed to intense deformation phase. The total length of the lineaments is 11279.83 m, maximum length of a lineament 1443.53 m while an average length of lineament is found to be about 352.49 m.

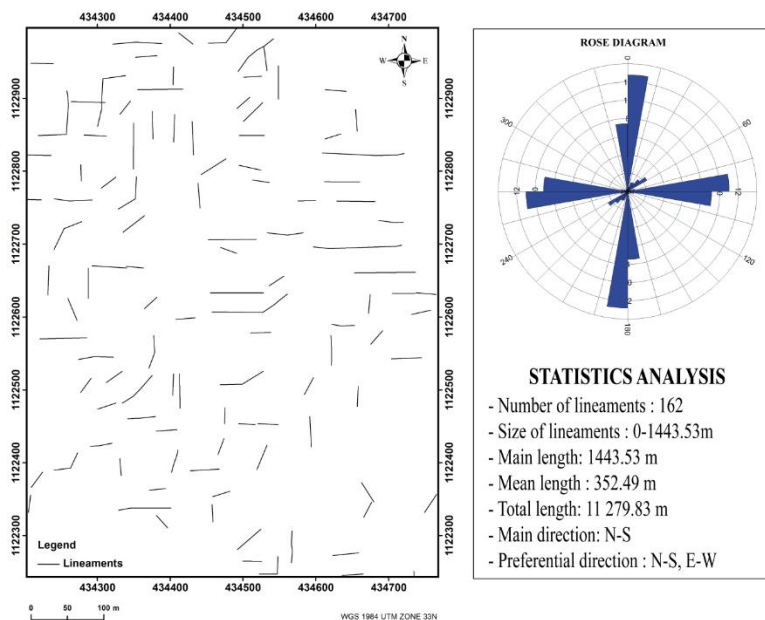


Figure 7. Map of the site lineaments and families of fractures generated by tectonics.

The TIN and calculated surfaces

The interpolation method used to form the triangles of the TIN is that of the Delaunay triangulation, which ensures that no vertex is within the circles in which the triangles of the lattice are circumscribed. To determine the areas of the logged and undeveloped portion of the rock-

mass, the mass points were carefully selected to accurately model the surfaces. Figure 8a shows the map of the mass points choice associated with different altitudes, while Figure 8b shows the total area of the deposit as well as that of the portion exploited by the Duclaire-Colasse company ($23\,730.774\text{ m}^2$) and also the undeveloped portion ($271\,317.655\text{ m}^2$).

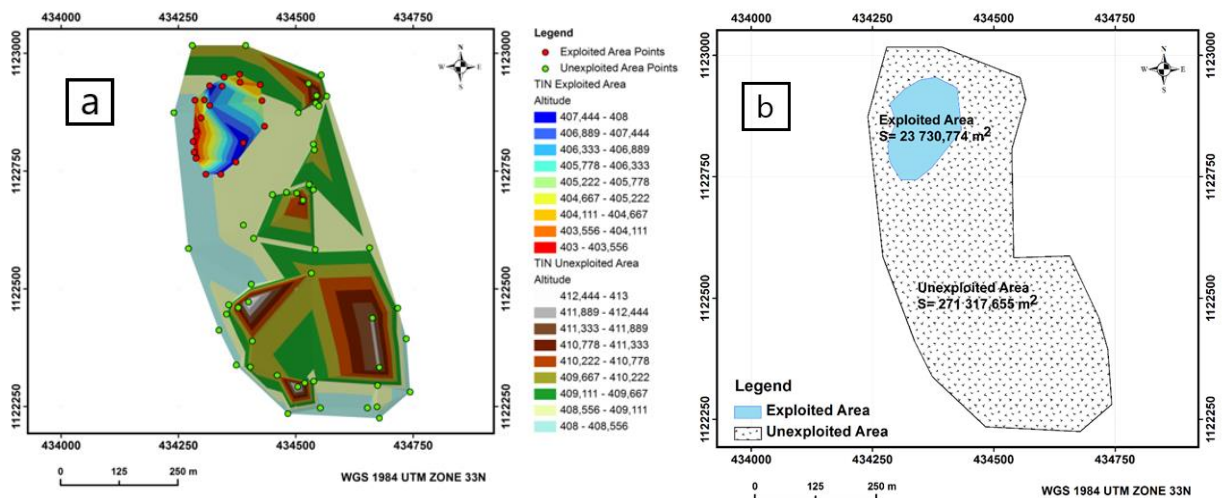


Figure 8. (a) Map of the mass point's choice associated with the different altitudes of the site, and (b) Representation of the site surface: exploited area in blue and unexploited hatched.

CONCLUSION

The precise description of a rock-mass depends on the knowledge of the rocks that constitute the matrix and the discontinuities that cross it. This description can be an essential phase for its understanding and its future exploitation. The main objectives of this study were, the petrographic, geotechnical and structural characterization of the Boboyo rock massif (Cameroon), the mapping of the fracture network of the site using satellite data SRTM and the morpho-surface evaluation of the rock-mass. It enables to highlight the existence of plagioclases, microcline, biotite, oxides in the rock-mass. The geotechnical tests gave the values of 31.8% for the Los-Angeles test and 10.3% for the Micro-Deval test. Rock samples showed a resistance to dynamic fragmentation of 23.10%. The Digital Terrain

Model (DTM) was obtained from an irregular array of triangles (TIN). The morpho-surface automatic extraction allowed estimating the surface of the already exploited rock-mass and its unexploited surface. In the end, in a fissured rock massif, it is very difficult to build structures without having first made a study of its fracturing and its mechanical and hydraulic behavior.

ACKNOWLEDGMENTS

The authors' thankful FMIP for providing the necessary facilities to carry out this work and the reviewers for their comments that improved the quality of this paper.

Compliance with Ethical Standards

The authors declare that they have no conflict of interest and adhere to copyright norms.

REFERENCES

- Akame, J.M., Mvondo-ondoa, J., Olinga, J.B., Essono, J. and Mbih, P.K., 2013. Application of (MNT) SRTM numeric field models for mapping structural lineaments: application to the Mezesse Archean, East of Sangme´ lima (South Cameroon). *Geo-Eco-Trop*, 37, 71–80.
- Akin, M., 2013. Slope stability problems and back analysis in heavily jointed rock mass: a case study from Manisa, Turkey. *Rock Mech. Rock Eng.*, 46(2), 359-371.
- Aksoy, C., 2008. Review of rock mass rating classification, historical developments, applications, and restrictions. *J. Mining Sci.*, 44(1), 51-63.
- Bertuzzi, R., Douglas K. and Mostyn, G., 2016. Comparison of quantified and chart GSI for four rock masses. *Eng. Geol.*, 202, 24-35.
- Brandes, H.G. and Robinson, C.E., 2006. Correlation of Aggregate Test Parameters to Hot Mix Asphalt Pavement Performance in Hawaii. *J. Transportation Eng.*, 132(1).
- Chaabouni, R., Bouaziz, S., Peresson, H. and Wolfgang, J., 2012. Lineament analysis of South Jenein Area (Southern Tunisia) using remote sensing data and geographic information system. *Egypt. J. Remote Sens. Space Sci.*, 15, 197–206.
- Chile's, J.P. and De Marsily, G., 1993. Stochastic models of fracture systems and their use in flow and transport modeling. In: Bear, J., de Marsily, G., Tsang, C.F. (Eds.), *Flow and Contaminant Transport in Fractured Rock*. Academic Press, San Diego, California, 169–236.
- Coggan, J.S., Stead, D. and Eyre, J.M., 1998. Evaluation of techniques for quarry slope stability assessment. *Transactions of the Institutions of Mining and Metallurgy, Section B: Appl. Earth Sci.*, 107.
- Dumort, J.C. and Péronne, Y., 1966. Explanatory note on the sheet of Maroua. 67p.
- El-Naqa, A. and Kuisi, M.A., 2002. Engineering geological characterisation of the rock masses at Tannur Dam site, South Jordan. *Environ. Geol.*, 42(7), 817-826.
- Ewodo-Mboudou, G., Bon, A.F., Bineli E., Ntep, F. and Ombolo, A., 2017. Characterization of the productivity of basement aquifers in the Far-North region, Cameroon. *J. Cameroon academy of sci.*, 14(1).
- Ganwa, A.A, Siebel, W., Frisch, W. and Shang, C.K., 2011. Geochemistry of magmatic rocks and time constraints on deformational phases and shear zone slip in the Méiganga area, central Cameroon. *Int. Geol. Rev.*, 53, 759-784.
- Jim-casaer., Martin-hermy., Pol-coppin, and Ron-verhagen., 2010. Analysing space use patterns by Thiessen polygon and triangulated irregular network interpolation: a non-parametric method for processing telemetric animal fixes. *Int. J. Geograph. Inform. Sci.*, 13(5).
- Jingsong, Wu, and Kevin, Amaratunga., 2003. Wavelet triangulated irregular networks. *Int. J. Geograph. Inform. Sci.*, 17(3).
- Jones, C.B., Kidner, D.B. and Ware, J.M., 1994. The Implicit Triangulated Irregular Network and Multiscale Spatial Databases. *The Computer J.*, 37(1), 43–57.
- Kline, S.W., Phiukhao, W., Griffin, M.L. and Miller, J.W., 2007. Evaluation of the sodium sulfate soundness test for qualifying dolomites of northern Arkansas for construction aggregate. In Shaffer, N.R., and DeChurch, D.A., eds, *Proceedings of the 40th Forum on the Geology of Industrial Minerals, 2004: Indiana Geological Survey Occasional Paper, 67*, 2007.
- Kouske, A.P., Suh, C.E, Ghogomu, R.T. and Ngako, V., 2012. Na-Metasomatism and Uranium Mineralization during a Two-Stage Albitization at Kitongo, Northern Cameroon: Structural and geochemical evidence. *Int. J. Geosci.*, 3, 258-279.

- Kunui, Hong., Eunchol, Han. and Kwangsong, Kang., 2017. Determination of geological strength index of jointed rock mass based on image processing, *J. Rock Mech. Geotech. Eng.*, 9, 702-708.
- Lato, M., Diederichs, M.S., Hutchinson, D.J. and Harrap, R., 2009. Optimization of LiDAR scanning and processing for automated structural evaluation of discontinuities in rock masses. *Int. J. Rock Mech. and Mining Sci.*, 46(1), 194-199.
- Lemy, F., Hadji. and Georgiou, J., 2003. Discontinuity trace map construction using photographs of rock exposures. *Int. J. Rock Mech. and Mining Sci.*, 40(6), 903-917.
- Louis, P., 1970. Geophysical contribution to the geological knowledge of the Lake Chad Basin. *bulletin ORSTOM*, 42.
- Moussa, I., 2011. Neoproterozoic crustal growth and differentiation: example of the Mayo-Kebbi pan-African domain in southwestern Chad. University Henri Poincaré, Nancy, France, pp. 339, Ph.D. Thesis.
- Moussa, I., André-Mayer, A.S., Vanderhaeghe, O., Barbey, P. and Deloule, E., 2012. A-type granites from the Pan-African orogenic belt in south-western Chad constrained using geochemistry, Sr–Nd isotopes and U–Pb geochronology. *Lithos*, 153, 39–52.
- Ngako, V., Affaton, P., Nnange, J.M. and Njanko, T., 2003. Pan-African tectonic evolution in central and southern Cameroon: transpression and transtension during sinistral shear movements. *J. Afr. Earth Sci.*, 36, 207–214.
- Ngako, V., Affaton, P. and Njonfang, E., 2008. Pan-African tectonics in northwestern Cameroon: implication for the history of western Gondwana. *Gondwana Res.*, 14, 509–522.
- Njanko, T., Nédélec, A., Kwékam, M., Siqueira, R. and Esteban, L., 2010. Emplacement and deformation of the Fomopéa pluton: implication for the Pan-African history of Western Cameroon. *J. Struc. Geol.*, 32, 306–320.
- Ngounou-Ngatcha, B., 1993. Hydrogeology of complex aquifers in semi-arid zone. Quaternary aquifers of Grand Yaere (Northern Cameroon). PhD, Univ. from Grenoble I, 357p.
- Ngounou-Ngatcha, B., Mudry J., Wakponou, A., Ekodeck, G.E. and SarrotReynauld, J., 2001. The Limani-Yagoua sandy belt (North Cameroon) and its hydraulic role. *J. Afr. Earth Sci.*, 32, 307-316.
- Nilsen, B., Dahl, F., Holzhäuser, J. and Raleigh, P., 2007. New test methodology for estimating the abrasiveness of soils for TBM tunnelling. In: 2007 RETC Proceedings (ed. Traylor, M. T., Townsend, J.W.), Society for Mining Metallurgy and Exploration, ISBN: 0873352564, EAN: 9780873352567, 104-116.
- Penaye, J., Toteu, S.F., Tchameni, R., Van Schmus, W.R., Tchakounté, J., Ganwa, A., Minyem, D. and Nsifa, E.N., 2004. The 2.1 Ga West Central African belt in Cameroon. *J. Afr. Earth Sci.*, 39, 159–164.
- Penaye, J., Kröner, A., Toteu, S.F., Van Schmus, W.R. and Doumnang, J.C., 2006. Evolution of the Mayo-Kebbi region as revealed by zircon dating: an early (ca. 740 Ma) PanAfrican magmatic arc in southwestern Chad. *J. Afr. Earth Sci.*, 44, 530–542.
- Sen, Z. and Sadagah, B.H., 2003. Modified rock mass classification system by continuous rating. *Engineering Geology*, 67(3-4), 269-280.
- Singh, M. and Rao, K.S., 2005. Empirical methods to estimate the strength of jointed rock masses. *Eng. Geol.*, 77(1-2), 127-137.
- Tchameni, R., Pouclet, A., Penaye, J., Ganwa, A.A. and Toteu, S.F., 2006. Petrography and geochemistry of the Ngaoundéré Pan-African granitoids in Central North Cameroon: Implications for their sources and geological setting. *J. Afr. Earth Sci.*, 44(4-5), 511-529.

- Thuro, K., Singer, J., K., Käsling, H. and Bauer, M., 2006. Soil abrasivity assessment using the LCPC testing device. In: *Felsbau* 24(6), ISSN 0174-6979, VGE Verlag GmbH, Essen, 37-45.
- Tomás, R., Delgado, J. and Serón, J.B., 2007. Modification of slope mass rating (SMR) by continuous functions. *Int. J. Rock Mech. Mining Sci.*, 44, 1062-1069.
- Tomás, R., Cuenca, A., Cano, M. and García-Barbra, J.A., 2012. Graphical approach for slope mass rating (SMR). *Eng. Geol.*, 124(4), 67-76.
- Tsai, V.J.D., 1993. Delaunay triangulations in TIN creation: An overview and a linear-time algorithm. *Int. J. Geograph. Inf. Sci.*, 7(6), 501–524.
- Tucker, G.E., Lancaster, S.T., Gasparini, N.M., Bras, R.L. and Rybarczyk, S.M., 2001b. An object-oriented framework for distributed hydrologic and geomorphologic modeling using triangulated irregular networks. *Comput. Geosci.*, 27(8), 959–973.
- Vavrek, P., 2004. Rock abrasivity from the exploration gallery for Višňové tunnel in Slovakia, In: *Rock Engineering, Theory and Praxis, Proc. ISRM Symp. Salzburg* (ed. W. Schubert), ISBN 3-7739-5995-8, 649-653.
- Vitthal, M., Khatik and Arup, Kr. Nandi, 2018. A generic method for rock mass classification. *J. Rock Mech. Geotech. Eng.*, (10), 102-116.
- Wambara, B., Wapouo, R. and Djimeli, A., 2017. Geological mapping of the Mayo-Kani department. Academic Internship Report 60p.
- Williams, W.A., Jensen, M.E., Winne, J.C. and Redmond, R.L., 2000. An automated technique for delineating and characterizing valley-bottom settings. *Environ. Monit. Assess.*, 64, 105–114.
- Yarali, O., Yaşar, E., Bacak, G. and Ranjith, P.G., 2008. A study of rock abrasivity and tool wear in Coal Measures Rocks, In: *Int. J. Coal Geol.*, 74, ISSN 0166-5162, Elsevier, Amsterdam, 53-66.
- Zhang, L., 2005. *Engineering properties of rocks*. Amsterdam: Elsevier Ltd.
- Zhang, L., 2010. Estimating the strength of jointed rock masses. *Rock Mech. and Rock Eng.*, 43(4), 391-402.
- Zhang, W. and Montgomery, D.R., 1994. “Digital elevation model grid size, landscape resolution, and hydrologic simulations.” *Water Resource Res.*, 30(4), 1019–1028.

Received on: 17.12.18; Revised on: 16.7.19; Accepted on: 1.8.19

Integration of probabilistic and knowledge driven models for delineating groundwater potential zones: a study on Hinglo river basin, Eastern India

Jagabandhu Roy*and Sunil Saha

Dept. of Geography, University of GourBanga, Malda- 732103, West Bengal

*Corresponding author: jagabandhuroy1991@gmail.com

ABSTRACT

Groundwater is an important natural resource, which controls the hydrological cycle. To identify the groundwater potentiality, the different geo-environmental factors such as geomorphology, geology, slope, land use/land cover, lineament density, and distance from river, pond frequency, rainfall, soil texture, relief, stream junction frequency and topographic wetness index (TWI) have been used. Groundwater potential map has been prepared using frequency ratio (FR), Shannon's entropy (SE) and analytical hierarchical process (AHP) models in GIS environment. For the calculation of frequency ratio (FR) and Shannon's entropy models, 224 wells have selected randomly in the study area. The AHP is another important method that has also been used to determine the weights of various thematic layers on basis of relative importance scale of Saaty's for the identification of groundwater potential zone. Besides, the weighted overlay method has been applied to generate a single layer of the groundwater potential index (GWPI). GPWI of these three models has been categorized into four distinct classes, namely 'low', 'moderate', 'good' and 'excellent'. Excellent groundwater potential zones based on these models covers an area of about 11.68%, 10.44% and 10.05% of total basin respectively. Afterwards, composite groundwater potential zone (CGWPZ) has been prepared based on GWPI of FR, Shannon's entropy and AHP models. For the validation of the results from all these models, the receiver operating characteristic (ROC) curve has drawn using the yield data of 60 pumping wells of this study area. The validated results show that the FR, Shannon's entropy and AHP models have achieved very good accuracy (AUC, What is AUC, spell in full=86.6% for FR model, AUC= 80.8% for Shannon's entropy model and AUC= 80.2% for AHP model), while CGWPZ has an excellent accuracy of AUC, 91%).

Keywords: Frequency Ratio (FR), Shannon's entropy (SE), Analytical Hierarchical Process (AHP); Composite Groundwater Potential Zone (CGWPZ); Receiver Operating Characteristic (ROC); Hinglo river basin

INTRODUCTION

Groundwater is an important natural resource that is used as drinking water in both urban and rural environment. Hence, it plays a vital role to sustain the human well-being, as well as aquatic and terrestrial ecosystems. Now-a-days, groundwater provides fresh water resource of about 34% of the total water supply. So, groundwater potentiality assessment is enormously important for the sustainable management of groundwater. The modern techniques like geographical information system (GIS) and remote sensing (RS) have been utilized for the purpose of natural resources management (Dar et al., 2010; Kumar et al., 2011;

Magesh et al., 2011). Generally, the traditional method is time dependent, economically costly and sometimes they fail (Todd and Mays, 2005; Jha et al., 2010). So, groundwater prospect or potentiality is defined as the amount of groundwater available in an area. The groundwater potentiality has been recognized using RS and GIS technique with the function of several hydrological factors (Jha et al., 2010). In absence of hydrological factors, the climatic, topographical, drainage factors have been used to delineate the probability of the occurrence of groundwater prospect zones (Greenbaum, 1992; Mukherjee, 1996; Oh and lee, 2010, Oh et al., 2011).

The methodology adopted in the literature to recognise the groundwater potential zones have been numerous (Chi and lee, 1994; Krishnamurthy and Srinivas, 1995; Kamaraju et al., 1996; Krishnamurthy et al., 1996; Sander et al., 1996; Edet et al., 1998; Saraf and Choudhury, 1998; Jaiswal et al., 2003; Rao and Jugran, 2003; Sikdar et al., 2004; Sener et al., 2005; Ravi Shankar and Mohan, 2006; Solomon and Quiel, 2006; Madrucci et al., 2008; Ganapuram et al., 2009; Suja Rose and Krishnan, 2009; PradeepKumar et al., 2010; Chowdhury et al., 2010; Jha et al., 2010; Machiwal et al., 2010; Dar et al., 2010; Manap et al., 2011; Khodaei and Nassery, 2011; Sahu and Sikdar, 2010; Abdalla, 2012; Pandey et al., 2013; Gumma and Pavelic, 2012; Al-Abadi, 2015; Rahmati et al., 2014; Chen et al., 2014; Prasad et al., 2007). Groundwater potentiality is accomplished by considering the thematic layers to generate a single layer of groundwater productivity index (GWPI). Generally, the GWPI is computed, using the weighted linear combination technique (Malczewski, 1999). The multi-criteria decision-making approach (MCDM) such as analytical hierarchy process (AHP) is also a vital method that is used to assign appropriate weightage to integrate the thematic layers in GIS environment. The AHP method is well-defined, efficient, flexible and accurate, which provides the meaningful results to solve the complicated problems (Satty, 1980). Different methods such as frequency ratio, weight of evidence, and logistic regression have also been used for the groundwater potentiality mapping (Ozdemir, 2011a, b). Similarly, Saha (2017) has applied the AHP method for groundwater potentiality mapping and Roy and Saha (2018) used the AHP method for land suitability analysis of paddy cultivation.

Among the different methods, the frequency ratio method is one of the important methods that are

used to calculate the probabilistic relationship between the dependent and independent variable of the different multi-classified maps. For the assessment of landslide susceptibility mapping, the frequency ratio (FR) model has been successfully applied (Lee and Pradhan, 2006; Akgün et al., 2008; Yilmaz, 2009; Mohammady et al., 2012; Regmi et al., 2013; Jaafari et al., 2014). It has also been applied for the forest fire identification (Pradhan et al., 2007). Presently, several researchers such as Ozdemir (2011a), Manap et al. (2012), Moghaddam et al. (2013) and Pourtaghi and Pourghasemi (2014) have used frequency ratio approach for groundwater prospect mapping based on GIS environment. Ozdemir (2011a) has been applied the frequency ratio and weights of evidence models in groundwater spring potential mapping in the Sultan Mountains (Konya, Turkey). Manap et al. (2012) has used the frequency ratio model for groundwater potential mapping in the Langat basin (Malaysia). The results presented 84.74 % accuracies with standard error of 0.063 for the frequency ratio model, which is relatively satisfactory. The Shannon's entropy is the important model that is used for landslide susceptibility mapping and groundwater potentiality mapping. There are several researchers who have successfully applied this method (Bednarik et al., 2010; Constantin et al., 2011; Pourghasemi et al., 2012a, b; Devkota et al., 2012; Jaafari et al., 2014).

The main objective of the present paper is to find out the groundwater potential zones, amalgamating probabilistic models (FR and Shannon's entropy) and knowledge driven model (AHP) in the Hinglo River basin of Eastern India.

DESCRIPTION OF THE STUDY AREA

Geographically, the study region covered an area of about 391.75 sq.km and lies between 23°42'7.09''N and 24°0'56.78''N latitude and

86°59'32.68''E and 87°23'31.91''E longitude in Eastern India (Figure 1). Hinglo River basin encompasses some portion of Jamtra district, Jharkhand and Birbhum district of West Bengal in Eastern India. It is the one of the major tributary of Ajay River. It originated from a spring at Fatafur block of Jamtra district and confluence with Ajay River at Palasdanga of Birbhum district. The total length of the main river course is 66 km. The Hinglo River consists of three hundred seventy-four 1st order stream, ninety-three 2nd order, twenty-four 3rd orders and five 4th order stream. The study area is situated under the influence of south-east Asian monsoon and is also influenced by the south-east and north-east Indian monsoon. Generally, the spatial distribution of average rainfall ranged from 1316mm to 1361mm respectively.

Physiographically, the regions belong to Chotonagpur plateau and Rarh plateau regions. Different geological segments are found in entire catchment area, namely granite-gneiss, Barker geological segment, ironstone shale, newer alluvium and quartzite (GSI, 1985). The thickness of the alluvium of eastern portion of the basin ranged from 12 to 20 m respectively (Ray and Shekhar, 2009). The depth of the ground water table fluctuated from 5 to 10 m.bgl of this region (Mukherjee et al., 2007). Pedologically, this region is composed of different type of soil textural classes such as sandy, clay, clay loam, sandy loam, loam, and fine loamy (NATMO, 2001). The elevation of this study area ranged from 60 m to 289 m from mean sea level. The northern and middle-western portion of this study area is threatened with highly soil erosion (Ghosh and Saha, 2015).

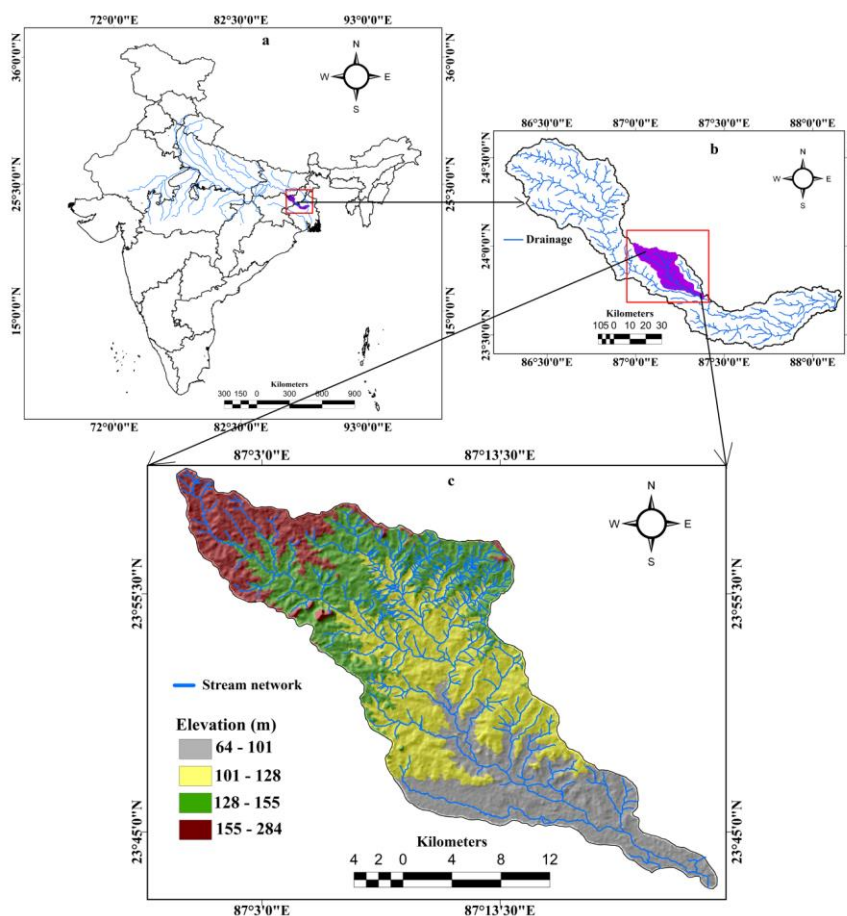


Figure 1. Location of the Study area. (a) India, (b) Ajay River Basin, (c) Hinglo River Basin

DATA and METHODOLOGY

Data sources and software

To complete the main targets of the present work, the different geo-environmental data like geomorphology, geology, slope, land use/land cover, lineament density, distance from river,

pond frequency, rainfall, soil textural, relief, stream junction frequency, topographic wetness index (TWI) have been used and mentioned the source table 1. The present work has been performed with the help of the different software like ARCGis10.10, ERDAS9.2, GEOMATICA, ENVI4.7, QGIS and SPSS17 softwares.

Table 1. Sources of Data Layers

Materials	Sources
Toposheets (No-73I/13,73I/16,73m/1, 73m/5,73m/6, 73p/4)	SOI,1974
Geological map no-73m	GSI,1985
Landsat 8OLI/TIRS	https://earthexplore.usgs.gov
ASTER DEM	https://earthexplore.usgs.gov
Soil Map	National Bureau of Soil Survey and Land Use Planning
Geomorphology	http://bhuvan5.nrsc.gov.in/bhuvan/wms
Rainfall	Indian Metrological Department

Generation of Thematic Layers of Selected Parameters to Determine the Groundwater Potentiality Zones

The rainfall data has been collected from Indian Metrological Department. The thematic layer of rainfall has been prepared by IDW method in GIS environment based on the last five years average rainfall data of different stations. The spatial distribution of rainfall of this study ranged from 1316mm to 1361 mm (Figure 3a). Geomorphological map of this study area has been prepared with help of digitization process in GIS which was collected from Bhuvan website. The entire study area is consisted of three board geomorphological regions namely the denudational origin, anthropogenic origin and fluvial origin (Figure 3b). The thematic layer of geology has been generated with the digitization process which was collected from geological survey of India. Geologically, the study area has been divided into five classes; granite gneiss, Newer alluvium, ironstone shale; black and grey

shale with ironstone bands and Barakar formation; sandstone, shale, coal and fire clay (Figure 3c).

In the Present study, the thematic layer of slope has been prepared from ASTER DEM imagery, using the spatial analysis tool in ArcGIS10. The spatial distribution of the basin ranged from 0 to 31 degrees (Figure 3d). The Landsat 8TM satellite image has been used to prepare the land use/land cover thematic layer with the help of maximum likelihood classification in GIS environment. The land use of this study area has been classified into five classes, namely agricultural land, natural vegetation, settlement, water bodies, and fallow land (Figure 3e). The thematic map of lineament density has been prepared from Landsat imagery with the help of GEOMATICA, ENVI 4.7 and ARCGIS 10.3.1 software. The spatial distribution of Lineament density of this study area ranged from 0 to 2.22 km² (Figure 3f). Drainage of the basin has been extracted from topographical map with the help of digitization process in GIS. So, the thematic layer of distance from river of this study area has been prepared with the help of

Euclidian distance tool of Arc GIS software. The spatial distribution of distance from river of this study area ranged from 0 to 2.08km (Figure 3g). The thematic layer of pond frequency has been generated based on the number of Pond per grid of topographical map with the help of IDW process in GIS environment in following equation 1.

$$P_f = \frac{\sum N_p}{A} \dots\dots\dots(1)$$

Where, P_f = Pond frequency, $\sum N_p$ =Total Number of Pond, A = per unit area,

The spatial distribution of pond frequency of this study area has ranged from 0 to 24 no. of pond per sq.km (Figure 3h). The thematic layer of soil texture has been generated from registered soil map with the help of digitization process in GIS environment. In the study area, seven types of soil textural classes have been found, namely sandy, sandy loam, loam, clay, clay loam, fine loamy mixed hyperthermic type haplustepts and paleustepts (Figure 3i). The relief map of this study area has been prepared from ASTER DEM imagery in GIS environment. The elevation of this study area ranged from 60 meters to 289 meters at the mean sea level (Figure 3j). The thematic layer of stream junction frequency has been prepared from topographical map based on the junction node of 1sq.km grid size with the help of IDW process in GIS environment in the following equation 2. It is defined by Ghosh and Saha (2015) as.

$$F_{sj} = \frac{\sum J}{A} \dots\dots\dots(2)$$

Where, F_{sj} = Frequency of stream junction, $\sum J$ = total number of stream node, A = per unit area,

The spatial distribution of stream junction frequency map ranged from 0 to 9.7 number of junction node per sq.km of this study area (Figure 3k). The thematic layer of TWI has been prepared from ASTER DEM imagery in GIS environment with the mention of following equation 3. It is defined by Moor et al. (1991) as

$$TWI = \ln\left(\frac{\alpha}{\tan \beta}\right) \dots\dots\dots(3)$$

Where, TWI= topographic wetness index, α is cumulative upslope area draining through a point (per unit contour length), β is the slope gradient (in degree). The spatial distribution of TWI of this study area ranged from 2.92 to 19.30 respectively (Figure 3l).

Multicollinearity Analysis

For the present study, the multicollinearity tests of selected variables have been done in SPSS software. The multicollinearity values are dependent on the variance inflation factors (VIF). The VIF and formal detection tolerance are adopted from equations 4 and 5.

$$Tolerance = 1 - R_j^2 \dots\dots\dots(4)$$

$$VIF = \left[\frac{1}{Tolerance} \right] \dots\dots\dots(5)$$

Where, R_j^2 is the coefficient of determination of a regression of explanatory j on all the other explanatory. A tolerance of less than 0.20 and 0.10 and variance inflation factors (VIF) 10 and above, indicates multicollinearity. (Saha 2017) has used this technique for the groundwater potentiality mapping. The present study has adopted the multicollinearity analysis using the following table 2.

Table 2. Collinearity statistics of groundwater potentiality determining parameters

Sl. No.	Parameters	Collinearity Statistics	
		Tolerance	VIF
1	Rainfall	0.226	4.435
2	Geomorphology	0.523	1.911
3	Geology	0.528	1.895
4	Slope	0.903	1.107
5	Land Use/ Land Cover	0.954	1.048
6	Lineament Density	0.986	1.014
7	River Distance	0.85	1.177
8	Pond Frequency	0.754	1.326
9	Soil texture	0.639	1.566
10	Relief	0.218	4.587
11	Stream Junction Frequency	0.766	1.305
12	Topographic wetness index	0.683	1.567

For the selection of the determining factor of ground water potentiality, collinearity test has been computed. VIF of all the selected parameters are

less than 10 percent, so there is no collinearity problem. The schematic diagram shows the methodological process in the figure 2.

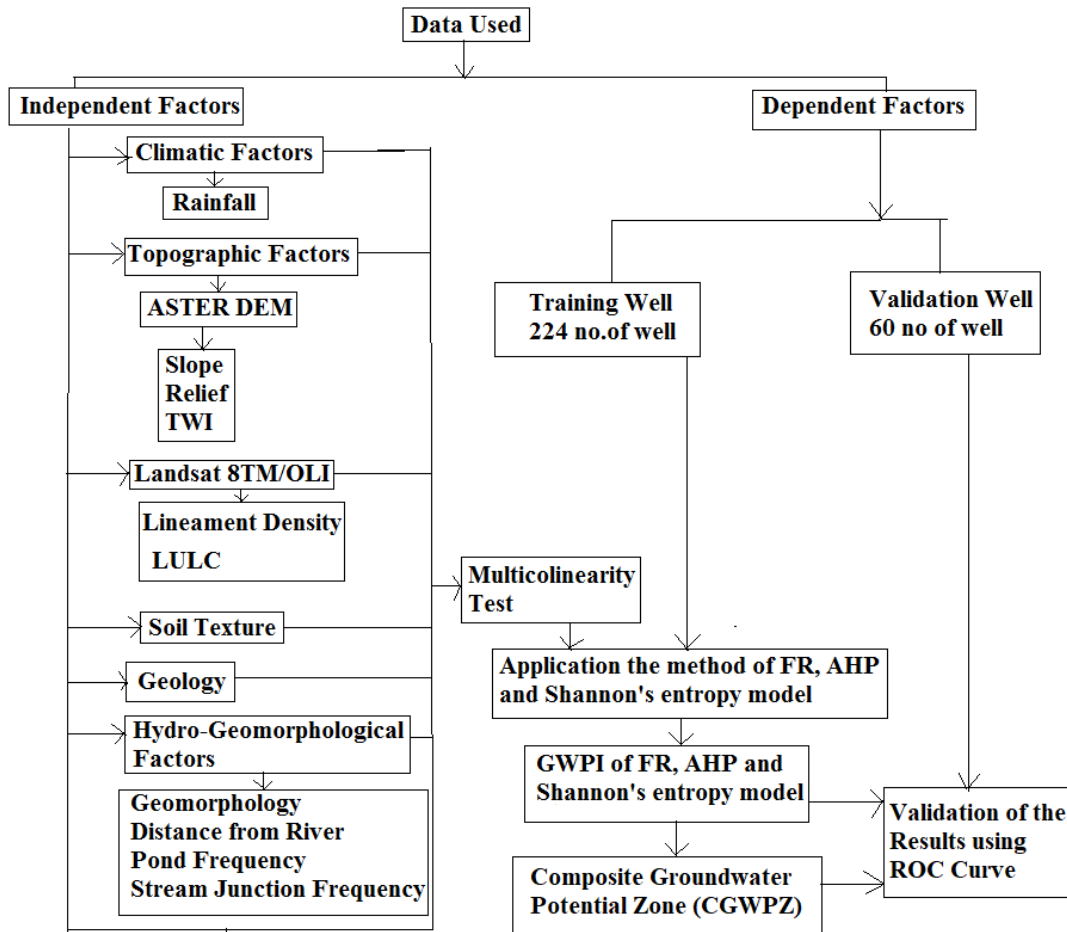
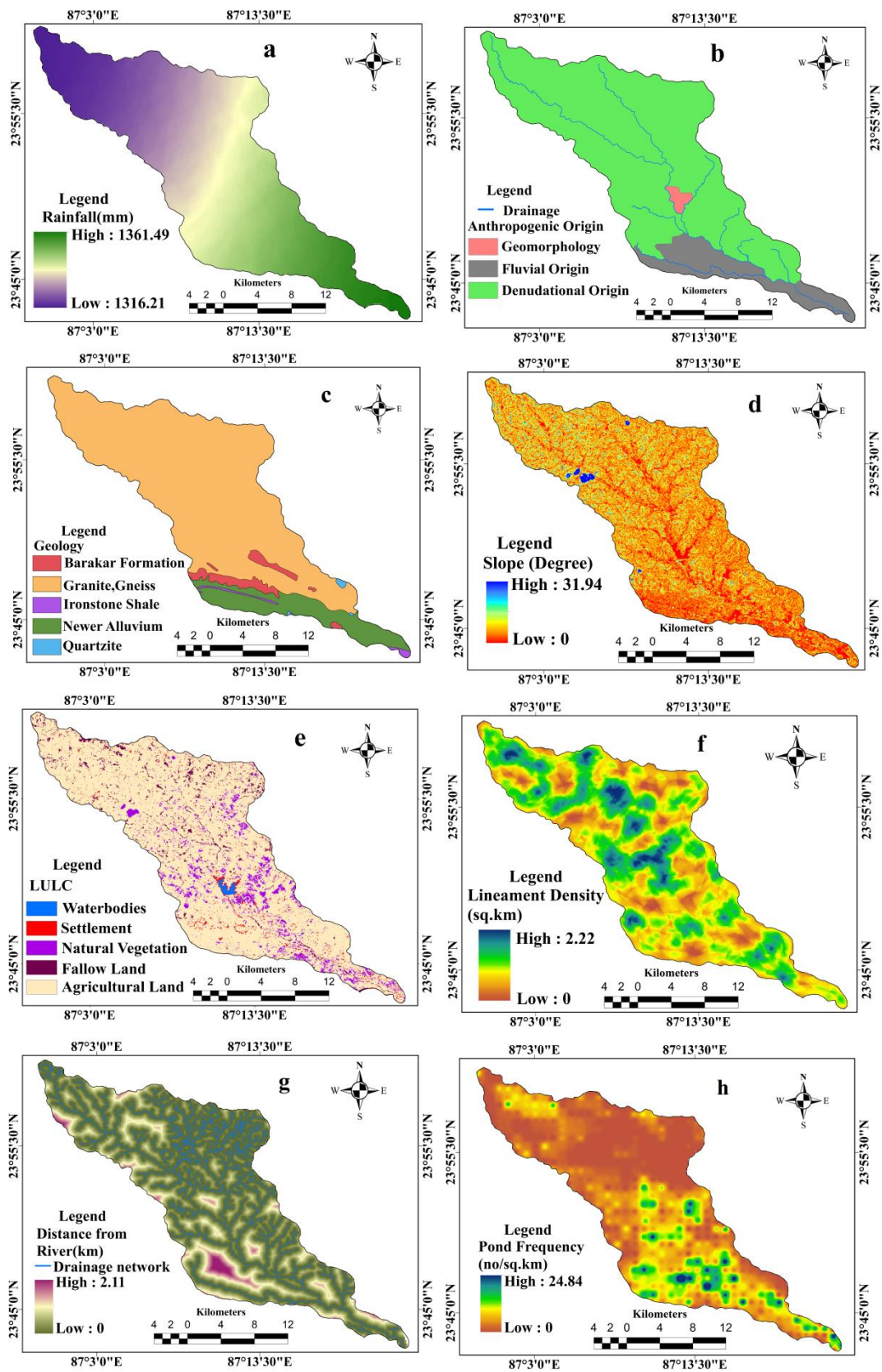


Figure 2. Schematic diagram representing the methodological procedure to determine the groundwater potentiality



Continue Fig. 3

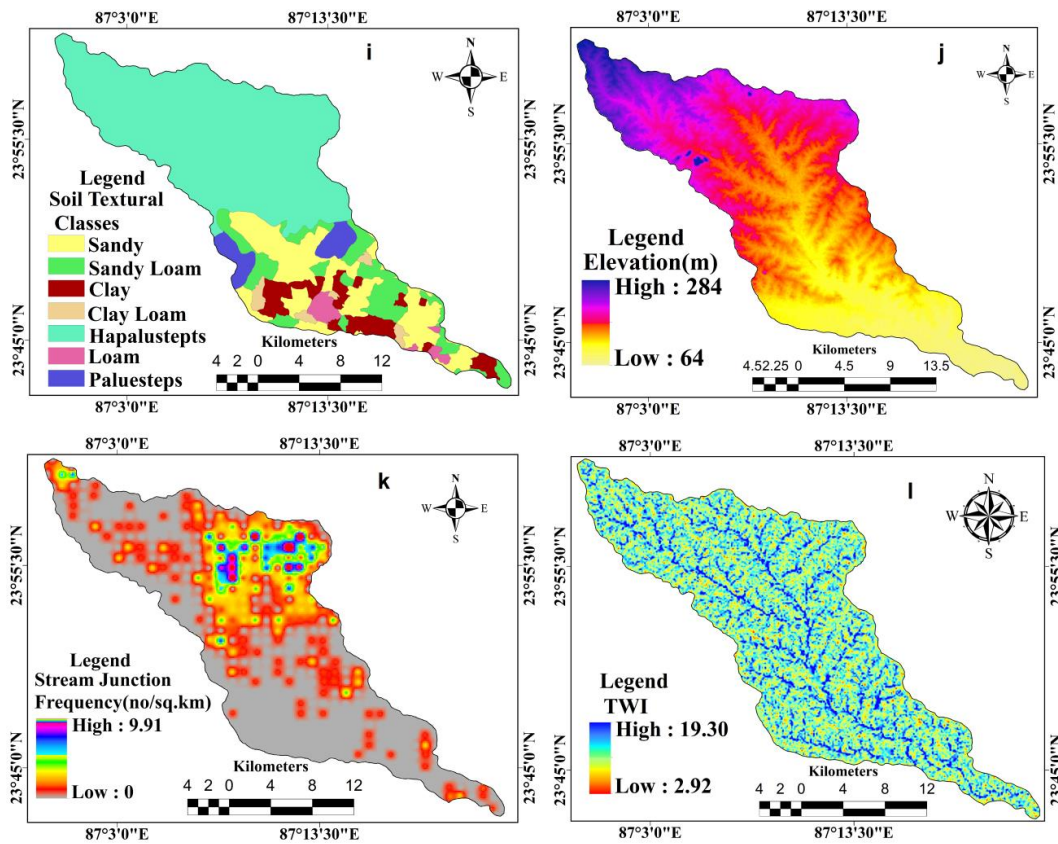


Figure 3. Thematic data layers representing groundwater potentiality determining factors - (a) rainfall, (b) geomorphology, (c) geology, (d) slope map, (e) land use/ land cover, (f) lineament density, (g) distance from river (h) pond frequency, (i) soil texture, (j) relief (k), stream junction frequency and (l) topographic wetness index (TWI).

Analytical Hierarchical Process (AHP)

Analytical hierarchical process has been used to assign the weightage of different thematic layers for the determination of the groundwater potential zone. In the present study, eigenvector method, which is most popular for calculating the weightage of the attribute from inconsistent matrices of pair-wise comparison (Saaty, 1990) has been used. The weightage value of each parameter has been calculated in each column of the pair wise comparison matrix and each cell value is divided by summed value of the same parameters. Primary eigenvector of the pair wise comparison matrix indicates the mean value of each row of the parameters. The consistency ratio (CR) may occur due to the randomly the matrix formed (Saaty, 1980, 1990, 1994). The consistency ratio is given by eq. 6.

$$CR = \frac{CI}{RI} \quad \dots\dots (6)$$

Where, CI is the consistency index and RI is the consistency index for a random square matrix of the same size. Consistency ratio (CR) should be lower than or equal 0 to 1. The CI can be calculated using the eq. 7.

$$CI = \frac{\lambda_{\max} - n}{n - 1} \quad \dots\dots (7)$$

Where λ_{\max} is the largest Eigen value of 'A' and 'n' is the order of the square matrix. If A is perfectly consistent, then λ_{\max} will be at a minimum and equal to n, producing a CI equal to zero. As inconsistency increases, λ_{\max} increases, producing a large value of CI.

As mentioned earlier, AHP process is the most reliable and accurate technique, which helps in identifying groundwater potential zone of an area (Wu and Wang, 2007; Youssef et al., 2011; Pourghasemi et al., 2012; Chandio et al., 2013;

Kaliraj et al., 2013; Althuwaynee et al., 2014; Fattahi et al., 2014; Navarro et al., 2014; Yang et al., 2014). The weightage by AHP of selected parameters, have been shown in the table 3.

Table 3. The selected parameters wise weights, matrix and consistency ratio by analytical hierarchical process (AHP)

Parameters	1	2	3	4	5	6	7	8	9	10	11	12	Weight
Rainfall	7	7	5	5	5	5	5	1	5	5	5	5	0.311
Geomorphology	1	2	0.33	2	0.33	0.5	0.2	0.14	0.5	1	0.5	1	0.042
Geology	0.5	1	0.5	1	0.33	0.5	0.2	0.14	0.5	1	0.5	0.33	0.032
Slope	3	2	1	2	1	1	0.5	0.2	1	1	1	1	0.068
Land use/Land Cover	0.5	1	0.5	1	0.5	0.5	0.5	0.2	1	1	1	0.5	0.043
Lineament Density	3	3	1	2	1	1	0.5	0.2	1	1	0.5	1	0.067
Distance from River	2	2	1	2	1	1	0.5	0.2	2	1	0.5	1	0.065
Pond Frequency	5	5	2	2	2	2	1	0.2	2	2	1	1	0.111
Soil Texture	2	2	1	1	1	0.5	0.5	0.2	1	1	0.5	1	0.055
Relief	1	1	1	1	1	1	0.5	0.2	1	1	0.5	1	0.052
Junction Frequency	2	2	1	1	2	2	1	0.2	2	2	1	2	0.09
Topographic Wetness Index	1	3	1	2	1	1	1	0.2	1	1	0.5	1	0.065

The selected parameters like rainfall, geomorphology, geology, slope, land use/ land cover, lineament density, distance from river, pond frequency, soil texture, relief, stream junction frequency, topographic wetness index have been assigned weightage based on the calculation of AHP process. AHP is the online priority raking calculator, which helps for priority ranking among the different parameters, based on the scale importance of Saaty's matrix. The consistency ratio is shown on the value of 0.033 among selected parameters. The rainfall is highly prioritized than another parameter, because the rainfall plays the vital role for the groundwater recharge.

The groundwater potential index (GWPI) is computed by the weighted linear combination method (Malczewski, 1999) using following equation

$$GWPI = \sum_{i=1}^n \sum_{j=1}^m [\alpha_i (\beta_{ij} x_{ij})] \dots\dots\dots(8)$$

Where β_{ij} = weight of the j th class of i th theme obtained by feature normalization and α_i = weight of the i th theme obtained by AHP, n = total number of thematic layers, and m = total number of classes in a thematic layer and x_{ij} is the pixel value of the j th class of the i th theme.

Frequency ratio (FR) model

According to (Bonham-Carter, 1994) the frequency ratio is defined as the ratio of the probability of an occurrence to the probability of a non-occurrence for given attributes. The method recognised the statistical correlation between well locations and the influencing groundwater occurrence factors. The calculation of FR has been done (Ozdemir, 2011b) using following equation.

$$FR = \frac{A/B}{C/D} = \frac{b}{a} \quad \dots\dots\dots (9)$$

where A is the number of pixels with well for each factor; B is the number of total well in study area; C is the number of pixels in the class area of the factor; D is the number of total pixels in the study area; b is the percentage for area with respect to a class for the factor and a is the percentage for the entire domain. The larger FR, the stronger the relationship between groundwater production and the given factor's attribute. To recognise the groundwater potential index, the obtaining value of FR has been summed as (Ozdemir, 2011b; Jaafari et al., 2014; Naghibi et al., 2014):

$$GWPI = \sum_{i=1}^n FR_i \quad \dots\dots\dots (10)$$

Where FR_i is the frequency ratio for 'a' factor and 'n' is the total number of used factors. This mathematical calculation technique has been applied for identifying groundwater prospect zone by Lee et al., (2006).

Shannon's entropy model

Entropy is defined as a measure of changeable in a random variable in information theory (Ihara, 1993). The entropy is also defined as the scope of the unpredictability, complaint, inequity, and randomness of a system (Yufeng and Fengxiang, 2009). More exactly, Shannon entropy is the average changeableness in a random variable that

is equal to its information content. The entropy of groundwater well yield signifies to the range that the several groundwater controlling factors impacts on the groundwater potentiality. Several groundwater determining factors carry additional entropy into the index system. So, the entropy value has been incorporated to compute objective weights of the index system (Jaafari et al., 2013). The information coefficient W_j value has been computed using following equations (Bednarik et al., 2010; Constantin et al., 2011; Jaafari et al., 2013)

$$P_{ij} = FR = \frac{b}{a} \quad \dots\dots\dots (11)$$

$$(P_{ij}) = \frac{P_{ij}}{\sum_{j=1}^{S_j} P_{ij}} \quad \dots\dots\dots (12)$$

$$H_j = -\sum_{j=1}^{S_j} (P_{ij}) \log_2 (P_{ij}) \quad \dots\dots\dots (13)$$

$$H_{jmax} = \log_2 S_j \quad \dots\dots\dots (14)$$

$$I_j = \frac{H_{jmax} - H_j}{H_{jmax}} \quad \dots\dots\dots (15)$$

$$W_j = I_j P_{ij} \quad \dots\dots\dots (16)$$

Where, FR = frequency ratio, P_{ij} = probability density, H_j and H_{jmax} = entropy values, S_j = number of classes, I_j = information coefficient, and W_j = the weight value for the factor as a whole. The value of W_j ranged between 0 and 1. The groundwater productivity index (GWPI) has been done (Devkota et al., 2012; Jaafari et al., 2014) using following equation.

$$y = \sum_{i=1}^n \frac{Z}{m_i} \times C \times W_j \quad \dots\dots\dots (17)$$

Where, y = sum of all the classes; i = the number of particular factor map; z = the number of classes within factor map with the greatest number of classes; m_i = the number of classes within

particular factor map; C = the value of the class after secondary classification; and W_j = the weight of a factor (Bednarik et al., 2010).

Table 4. Frequency ratio and information coefficient values of the selected Parameters

Rainfall	Area (pixel)	Area of % (a)	No of Well	% of Well (b)	FR (b/a)	P_{ij}	H_j	H_{jmax}	I_j	W_j
Very low(1316-1326mm)	5264	21.350	36	16.071	0.753	0.144	2.235	2.322	0.037	0.007
low(1326-1327mm)	4796	19.452	38	16.964	0.872	0.167				
Medium (1327-1348mm)	6043	24.509	43	19.196	0.783	0.150				
High(1348-1360mm)	4610	18.697	43	19.196	1.027	0.197				
Very high(1360-1372mm)	3943	15.992	64	28.571	1.787	0.342				
Geomorphology										
Fluvial Origin	294	1.192	3	1.339	1.123	0.347	1.581	1.585	0.002	0.001
Anthropogenic Origin	3566	14.463	37	16.518	1.142	0.353				
Denudational Origin	20796	84.345	184	82.143	0.974	0.301				
Geology										
Barakar formation	822	3.334	15	6.696	2.009	0.473	1.514	2.322	0.348	0.070
Ironstone Shale	153	0.621	0	0.000	0.000	0.000				
Quartzite	59	0.239	0	0.000	0.000	0.000				
Granite	20771	84.243	175	78.125	0.927	0.218				
Newer Alluvium	2851	11.563	34	15.179	1.313	0.309				
Slope(degree)										
Very low (0-1.5)	12680	51.428	88	39.286	0.764	0.208	1.529	2.000	0.235	0.059
low (1.5-3.5)	7048	28.585	94	41.964	1.468	0.399				
Medium (3.5-11.2)	3203	12.991	42	18.750	1.443	0.393				
High (11.2-31.9)	1725	6.996	0	0.000	0.000	0.000				
Land use /land cover										
Water bodies	482	1.955	2	0.893	0.457	0.126	2.207	2.322	0.050	0.010
Settlement	1057	4.287	10	4.464	1.041	0.288				
Natural Vegetation	2483	10.071	14	6.250	0.621	0.172				
Fallow land	1080	4.380	4	1.786	0.408	0.113				
Agricultural land	19554	79.307	194	86.607	1.092	0.302				
Lineament Density										
Very low (0-0.23 km ²)	3097	12.561	28	12.5	0.995	0.198	2.292	2.322	0.013	0.003
Low (0.23-0.65 km ²)	6087	24.688	46	20.536	0.832	0.165				
Medium (0.65-1.01 km ²)	6330	25.673	59	26.339	1.026	0.204				
High (1.01-1.41 km ²)	4689	19.018	59	26.339	1.385	0.275				
Very high (1.41-2.22 km ²)	4453	18.061	32	14.286	0.791	0.157				
Distance from River										
Very low (0-0.18 km)	10853	44.018	29	12.946	0.294	0.041	2.106	2.322	0.093	0.019
Low (0.18-0.42 km)	7282	29.534	88	39.286	1.330	0.187				
Medium (0.42-0.72 km)	3962	16.069	76	33.929	2.111	0.296				
High (0.72-1.16 km)	2077	8.424	21	9.375	1.113	0.156				
Very high (1.16-2.08 km)	482	1.955	10	4.464	2.284	0.320				
Pond Frequency										
Very low (0-1no/km ²)	7752	31.441	38	16.964	0.540	0.044	1.787	2.322	0.231	0.046

Low (1-4 no/km ²)	10123	41.057	74	33.036	0.805	0.065				
Medium (4-8 no/km ²)	5432	22.031	74	33.036	1.500	0.122				
High (8-13 no/km ²)	1234	5.005	31	13.839	2.765	0.225				
Very high (13-24 no/km ²)	115	0.466	7	3.125	6.700	0.544				
Soil texture										
Sandy	1463	5.934	28	12.500	2.107	0.233	2.701	2.807	0.038	0.005
Sandy Loam	391	1.586	4	1.786	1.126	0.124				
Clay loam	15215	61.709	101	45.089	0.731	0.081				
Clay	444	1.801	7	3.125	1.735	0.192				
Loam	882	3.577	5	2.232	0.624	0.069				
Haplustepts	3693	14.978	50	22.321	1.490	0.165				
Paleustepts	2568	10.415	29	12.946	1.243	0.137				
Relief										
Very low(0-31m)	10832	43.933	101	45.089	1.026	0.269	1.965	2.322	0.154	0.031
Low (31-53 m)	8623	34.973	93	41.518	1.187	0.311				
Medium (53-74 m)	5074	20.579	29	12.946	0.629	0.165				
High (74-198 m)	113	0.458	1	0.446	0.974	0.255				
Very high (198-283 m)	14	0.057	0	0.000	0.000	0.000				
Junction Frequency										
Very Low (0-0.45 no/km ²)	14158	57.422	150	66.964	1.166	0.335	2.150	2.322	0.074	0.015
Low (0.45-1.39 no/km ²)	5871	23.812	49	21.875	0.919	0.264				
Medium (1.39-2.93 no/km ²)	2923	11.855	19	8.482	0.715	0.205				
High(2.93-5.08no/km ²)	1254	5.086	5	2.232	0.439	0.126				
Very high (5.08-9.7no/km ²)	450	1.825	1	0.446	0.245	0.070				
Topographic Wetness Index (TWI)										
very low (2.92-7.35)	4569	18.531	45	20.089	1.084	0.219	2.304	2.322	0.008	0.002
low (7.35-8.38)	9271	37.601	78	34.821	0.926	0.187				
medium (8.38-9.73)	7155	29.019	75	33.482	1.154	0.233				
high (9.73-11.85)	3039	12.326	20	8.929	0.724	0.146				
very high (11.85-19.30)	622	2.523	6	2.679	1.062	0.214				

Generation of composite groundwater potential one (CGWPZ)

Composite groundwater potential zone (CGWPZ) has been calculated with the help of the raster calculator in ArcGis 10.3.1 software using following equation.

$$CGWPZ = \sum GWPI \text{ of FR, AHP and Shannon's entropy models} \quad (18)$$

In the present study, three raster layers of GWPZ based on AHP, FR and Shannon's entropy models have been composited and generate a single layer of composite groundwater potential index (CGWPZ) in GIS environment.

RESULTS and DISCUSSION

Application of AHP Model

Rainfall is the major component of the hydrological cycle. It also determines the subsurface water availability through the infiltration process. In this connection, rainfall thematic layer has been classified into five categories, like very low (1316mm-1326mm), low (1326mm-1337mm), medium (1337mm-1348mm), high (1348mm-1360mm) and very high (1360mm-1372mm). Each sub-layer of this factor has been assigned weights by the procedure of AHP method. Very amount of rainfall of this study area has been assigned highly rating by AHP. With the help of AHP process, each sub-

layer of geomorphology has been assigned weightage based on the scale importance of the Saaty's matrix. The fluvial origin is the main source for the groundwater recharge of this study area. So, the large drainage system and fluvial origin has been assigned highly weightage by the AHP method. Different geological segments have been assigned weightage by the AHP process. Even though majority of the study area is covered by granite gneiss formation and lower part of the study area is covered with the newer alluvium formation. The middle part of the basin is covered with ironstone shale: black and grey shale with ironstone bands. Among the geological formations, the newer alluvium is highly favourable for the groundwater recharge. Slope is the boost component of environment to determine the groundwater potentiality.

To assign the weightage, the slope map of the study area has been divided into four classes: very low slope ($0-1.5^\circ$), low slope ($1.5-3.5^\circ$), medium slope ($3.5-11.2^\circ$) and high slope ($>11.2^\circ$) with the help of AHP process. The slope gradient directly influences the infiltration of rainfall. In the low slope area, the probability of groundwater recharge is very high, but it is reverse for the high slope area due to quick flow of water. Land use/land cover is one of the important parameter which influences the groundwater recharge through controlling the infiltration rate, surface runoff, and evapotranspiration. In the dense forest areas, the rate of infiltration is quite higher than the build-up areas (Waikar and Nilawar, 2014). Each sub-layer of land use types has been assigned weightage with the help of the AHP process. The natural vegetation and agricultural crops are supported to penetrate the water in sub-surface layer, but the built-up area, concrete road and rocky land use, also disturbed the recharge of ground water.

A lineament, which is defined as the joints, fractures and fault of the rocks, helps to make a suitable pathway for the movement of water into the subsurface. It has been categorized into five classes such as very low ($0-0.23 \text{ km}^2$), low ($0.23-0.65 \text{ km}^2$), medium ($0.65-1.01 \text{ km}^2$), high ($1.01-1.41 \text{ km}^2$) and very high ($1.41-2.22$). Each sub-layer has been assigned weighted by AHP method to determine the groundwater potential zones. In case of distance from river map, it has been classified into five sub-classes such as very low ($0-0.18\text{km}$), low ($0.18\text{km} -0.42\text{km}$), medium ($0.42\text{km}-0.72\text{km}$), high ($0.72\text{km} -1.16\text{km}$), very high ($1.16\text{km} -2.08\text{km}$). Sub-layer wise weightage helps to delineate the groundwater prospect zone.

The distance from river is significantly correlated with the groundwater recharge zone. The nearest area from river is more probable of groundwater recharge than another area which is located far from the river. So, very low distance from river sub-class has been assigned highly rating by AHP method. For the present study, the pond frequency map has been divided into five sub-classes such as very low ($0-1 \text{ no}/\text{km}^2$), low ($1-4 \text{ no}/\text{km}^2$), medium ($4-8 \text{ no}/\text{km}^2$), high ($8-13 \text{ no}/\text{km}^2$) and very high ($13-24 \text{ no}/ \text{sq.km}$). Generally, the availability of sub-surface water is depended on the large number of ponds, where water holding capacity is maximum than another area of the basin. Therefore, very high pond frequency sub-class is assigned highly weightage value with the help of AHP process. The groundwater prospect and movement is also dependant on the porosity and permeability of soil texture. Sub-layer wise weightage has been assigned by the AHP process. Clay soil type is highly prioritized due to its maximum water holding capacity than another soil texture types for the present study.

Altitude of the basin is a further important determining factor of groundwater recharge. Steep

slope of an area is always associated with the high relief, which is concerned with the quick flow of water. The elevation map has been classified into five sub-classes such as very low (0-31m), low (31-53 m), medium (53-74m), high (74-198 m) and very high (198-283m) with the help of the natural break classification method in GIS environment. AHP method helped to assign weightage each sub-class and supported to integrate in GIS environment. The very low elevation area is highly prioritized because it can hold the water and supplies into the subsurface of the basin. Similarly, the stream junction frequency map of this study area has been classified into five sub-classes such as very low (0-0.450 no/km²), low (0.45-1.39 no/km²), medium (1.39-2.93 no/km²), high (2.93-5.08 no/km²) and very high (5.08-9.7 no/km²). With the help of AHP technique, weight of each sub-layer has been assigned to detect the groundwater prospect. The very high concentration of stream junction node is representing the most groundwater prospect zone and it also highly prioritized by AHP method for the present study. TWI map has been divided into five sub-classes such as very low (2.92 -7.35), low (7.35-8.38), medium (8.38-9.73), high (9.73-11.85) and very high (11.85-19.30) topographic wetness index respectively. Each sub-layer of TWI has been assigned weightage by the AHP process. The raster format of TWI has been multiplied by each rating weight to integrate with the other rating factors in GIS for the determination of the groundwater potential zones. The very high value of TWI of this study area is highly prioritized by AHP process because it has more water retention than another sub-layer of TWI.

The GWPI of AHP model has been shown in figure 4e. As per results of AHP model, groundwater potential index values of this study area have been categorized into four groundwater

potential zones, like 'low', 'moderate', 'good' and 'excellent' zone with the help of the natural break classification method. Only 10.05% area is covered with excellent groundwater potential area. Another portion of the basin is covered with low (37.41%), moderate (40.50%), and good (12.02%) groundwater potential area (Table 5).

Application of FR Model

For the demarcation of groundwater potentiality, Frequency ratio (FR) model is related with the well and conditioning factors that is shown in table 4. Frequency ratio is defined as the ratio of the area where the total pixel value of well in each sub-class of conditioning factors is divided by the total pixel value of each sub-class of the conditioning factors for the identification of the groundwater probability. The value of 1 is shown as average value, indicating the average relationship. The high and low correlation is occurred when the value ranged from >1 and <1 FR value (Oh and Lee, 2010). The result of application of frequency model are summarised in table 5. With respect to the FR results in rainfall, the FR value for high (1342mm to 1351mm) and very high (1351mm to 1361mm) rainfall sub-classes are 1.027 and 1.787 respectively, applied for the high groundwater productivity of these class ranges. The FR ratios of other classes are low, representing the low probability of groundwater potentiality. Geomorphologically, the FR value of fluvial origin and anthropogenic origin are 1.123 and 1.142 respectively, detecting the high groundwater potentiality than other class.

As mentioned earlier, geologically this region consists five geological segments namely Barakar formation, ironstone shale, newer alluvium, granite-gneiss, and quartzite. The high FR ratio has been found on the Barakar formation and newer alluvium. The FR values of Barakar formation and newer alluvium is found the value

of 2.009 and 1.313 respectively, indicating the high groundwater prospect of these geological segments. The FR ratios of granite-gneiss, quartzite geological segments are less than 1 value, representing the low groundwater potentiality. The analysis of FR value of slope has been shown in table 4. The low (1.5 to 3.5 degree) and medium (3.5 to 11.2) slope is representing >1 FR ratio than another sub-class of slope. So, the high FR value indicates the more groundwater potentiality. In this study area, slope is increasing, and FR ratio is decreasing. In case of land use/cover factors, the agricultural land and settlement is attained the >1 FR value that indicates the high groundwater potentiality of these classes. To interpret the FR model, the lineament density is related to the groundwater productivity. The FR value of medium (0.05 to 1.01sq.km) and high (1.41 to 2.22sq.km) sub-class of lineament density are 1.026 and 1.385 respectively. So, these sub-classes have been highly prioritized for the high probability of groundwater potentiality. Another sub-classes of lineament density are ranged <1 FR value, that is less significant for the identification of groundwater prospect. To analysis of distance from river, the FR value of medium, very high distance is attained >1 value for suitable to recoinage the groundwater potentiality. To know the detail information of pond frequency factor for FR model, the very high, high, medium sub-class of pond frequency is attained the >1 FR value that indicates the high probability of groundwater potentiality among these sub-classes. In case of soil texture factors, the high FR value has been found on the sandy, clay, sandy loam soil texture, haplustepts, plustepts. These factors are influencing for the identification of groundwater prospect zone.

The altitude of the basin is related to the groundwater potentiality. The FR value of very low (0 to 312 m) and low (31 to 53m) sub-class of elevation are 1.026 and 1.187 respectively than another sub-classes of this factor. So, this sub-class is representing the high probability of groundwater potentiality due to its more water holding capacity. The stream junction frequency is the important factor of FR model to recognise the groundwater potentiality. The high FR value is found on the very low stream junction frequency sub-class that is indicating the high probability of groundwater potentiality. For the present study, the low, medium and very high sub-class of TWI is highly prioritized for the high probability of groundwater potentiality by the representing the >1 value of FR for these classes.

Based on the Frequency Ratio (FR) model, the final groundwater potential zone was calculated using the calculation (eq. 9, 10) and explained in a map (Figure 4a). The obtained GWPI was classified into four categories viz low, moderate, good, and excellent classes. Only 11.68% area is covered with excellent groundwater potential area of this study area. On the other hand, the low, moderate, good groundwater potential area is extended over an area of 48.89%, 24.02% and 15.41% respectively (Table 5).

Application of Shannon's entropy model

The application of Shannon's entropy explains the relationship between the well and groundwater-influencing factors that is shown in Table 4. As the results of Shannon's entropy model, Rainfall has been shown a weight of 0.007, while geomorphology has a weight of 0.001, and geology of 0.070 respectively. The TWI, lineament density and stream junction frequency have been represented the weight value of 0.002, 0.003, 0.015 respectively. The strong relationship

has been found on different parameters such as slope, land use/land cover, distance from river, pond frequency and relief. These parameters have shown the weight value of 0.059, 0.010, 0.019, 0.046, and 0.031 respectively. On the contrary, the weak importance has been found on the TWI, geomorphology, and lineament density factors. GWPI of Shannon's entropy model has been classified into four categories viz, low, moderate, good, excellent based on the natural break classification (Figure 4b). This technique represented that excellent groundwater potential zone extended over an area of about 10.44% area. The excellent groundwater potential area is consistent with the FR model and AHP model. Another portion of this study area, low, moderate, good groundwater potential zones are covered with an area about 46.92%, 27.27% and 15.36% area respectively.

Afterwards, the groundwater potential maps of FR, AHP and Shannon's entropy model have been divided in 30*30 grid cell size. The outcomes of FR, AHP models show that excellent groundwater potential zones of these three models are found on the lower portion, like Khyrasole, Panchra, Sabarganga, Bataspur, and Palasdanga of the study area. On the other hand, very low groundwater potential zones are found on western and north-western parts of the basin, because of the rugged topographic and presence of impermeable rocks. Geologically, western and north-western parts of this study area are covered with granite-gneiss formation, which cannot help to percolate the runoff water into the sub-surface layer. So, the lower catchment of this study area is also adopted with suitable criteria like clay type soil, high concentration pond frequency, maximum stream junction frequency and availability of newer alluvium geological segments.

Composite groundwater potential Zone (CGWPZ)

The CGWPZ map has been classified into four categories like low, moderate, good and excellent potential zone (Table 6) with the help of the natural break classification method in GIS environment as well as GWPZ of AHP, FR and Shannon's entropy models (Figure 5a). Only 8.48% area is excellent groundwater potential zone that is found in the lower catchment. The excellent potential area is comparatively least area than another excellent zone of GWPZ of AHP, FR and Shannon's entropy models. The CGWPZ has been validated by ROC curve which is representing the excellent results than AHP, FR and Shannon's entropy models.

Validation of models (ROC Curve)

Validation is the suitable technique of modelling for the justification and experiment to solve the problem (chung and Fabbri, 2003). Groundwater potential zones map of this study area has been validated through the ROC curve. Groundwater yield data of some randomly selected wells has been used for validating the present work. Receiver Operating Characteristic (ROC) curve has been used to evaluate the accuracy assessment of groundwater potential maps of this study area that means of validation of Frequency Ratio, Shannon's entropy and AHP model. ROC is the reliable, appropriate, accurate and well accepted technique to find out the diagnostics of the problems for the assessment and judgment (Pradhan 2009a, 2013b; Mohammady et al., 2012; Pourghasemi et al., 2014). The prediction accuracy value has been classified into different categories based on the area under curve (AUC) such as poor if AUC= 0.6–0.5; 0.7–0.6 =average; good=0.8–0.7; very good =0.8–0.9 and excellent =1–9 (Yesilnacar, 2005). In this basin area, about 226 training wells and 60 validation points has

been selected to generate the ROC curve. The ROC results of FR, Shannon's entropy and AHP models have been represented the very good

prediction accuracy value (86.3%, 80.8% and 80.2% respectively).

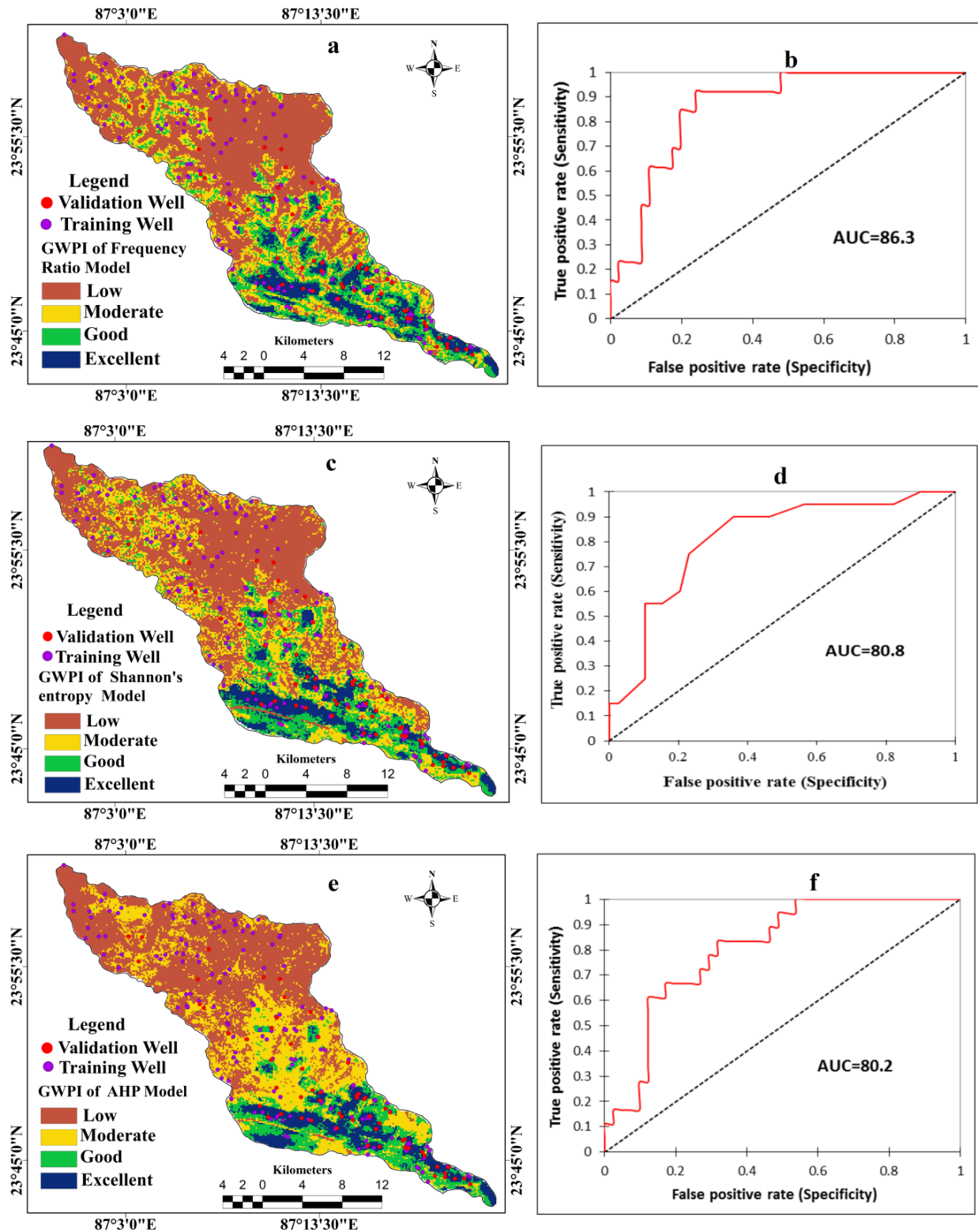


Figure 4. Thematic layers and graphs representing - a. GWPI by FR model, b. ROC for FR model, c. GWPI by Shannon's entropy model, d. ROC for Shannon's entropy model, e. GWPI by AHP model, f. ROC for AHP model.

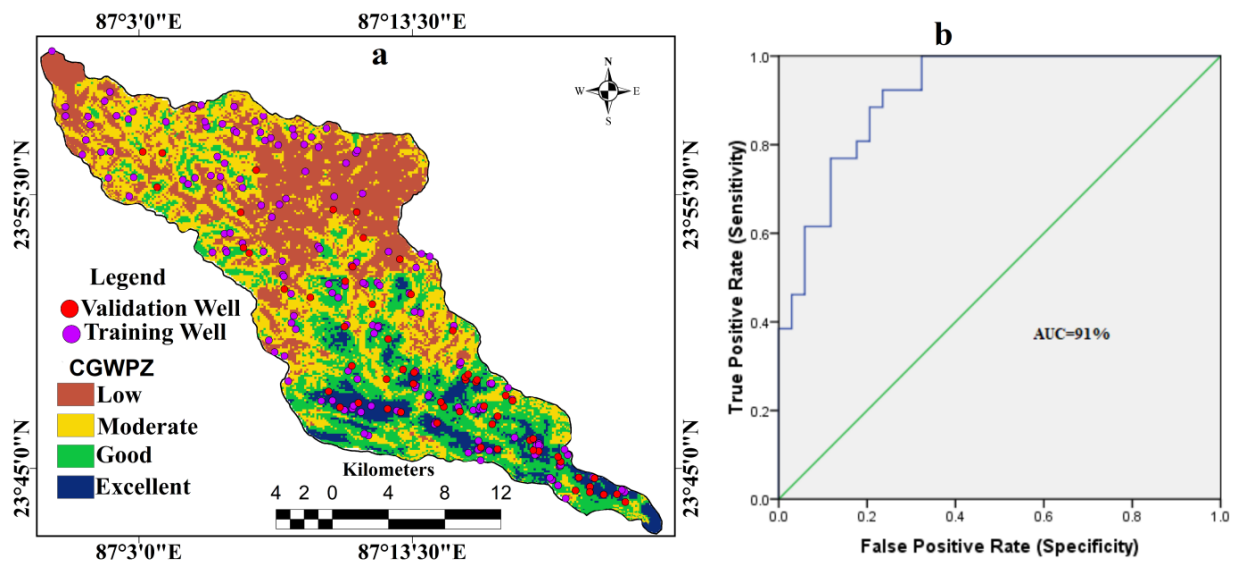


Figure 5. Thematic layer and graph representing- a. composite groundwater potential index (CGWPZ), b. ROC curve of CGWPZ.

Table 5. GWPI area distribution of AHP, FR and Shannon's entropy Models

Classified GWPI	AHP Model		FR Model		Shannon's entropy Model	
	Area in sq.km	% of Area	Area in sq.km	% of Area	Area in sq.km	% of Area
Low	146.563	37.412	191.510	48.890	183.820	46.920
Moderate	158.689	40.508	94.090	24.020	106.840	27.270
Good	47.112	12.026	60.370	15.410	60.180	15.360
Excellent	39.386	10.054	45.770	11.680	40.910	10.440

Table 6. Areal Distribution of Composite Groundwater Potential Zone (CGWPZ)

Classified CGWPZ	Area in sq.km	% of Area
Low	119.425	30.485
Moderate	139.593	35.633
Good	99.503	25.399
Excellent	33.226	8.481

CONCLUSION

Groundwater prospect zones have been demarcated in Hinglo river basin using geo-spatial technique. The results of FR, Shannon's entropy and AHP models can be considered to take decision for sustainable water resource management. GIS is the modern technology which solves the problem easily and helps to minimize the time, labour and money. The well location and

environmental factors (like rainfall, geomorphology, geology, lineament density, pond frequency, stream junction frequency, land use/cover, relief and TWI) can be correlated and considered as the suitable way for identification of groundwater potentiality zones. The groundwater potentiality zone (GWPZ) maps based on FR, Shannon's entropy and AHP models have been prepared and categorized into four classes, namely

low, moderate, good and excellent groundwater potentiality zones in GIS environment. The excellent groundwater potential zones of three models have been covered with an area of 11.68%, 10.44% and 10.05 % respectively. The areas under curve (AUC) of three models show very good accuracy. The FR model has provided the most suitable result compared to other models. According to the composite groundwater potential zone (CGWPZ) map, only 8.48% of the total basin area has excellent groundwater potentiality. Comparatively, CGWPZ is most suitable for identification of groundwater potentiality according to the area under value (AUC=91%) than other models (FR, Shannon's entropy and AHP). As per results of GWPZ and CGWPZ, The lower catchment is more prospective of groundwater potentiality in the whole part of the basin. The results of the present study may be used as guidelines for planning of future artificial recharge projects in the study area to confirm supportable groundwater exploitation.

ACKNOWLEDGEMENT

Authors would like to thank the inhabitants of Hinglo River Basin because they were helped and provided valuable information during our field visit. The authors would like to give special thanks to the reviewers for their constructive and useful comments during the review process. At last, authors would like to acknowledge all of the agencies specially, Survey of India (SOI), Geological Survey of India (GSI), Indian Meteorological Department (IMD) and USGS for providing the necessary data and maps for the study.

Compliance with Ethical Standards

The authors declare that they have no conflict of interest and adhere to copyright norms.

REFERENCES

- Abdalla, F., 2012. Mapping of groundwater prospective zones using remote sensing and GIS techniques: A case study from the Central Eastern Desert, Egypt. *J. African Earth Sci.*, 70, 8-17. doi:10.1016/j.jafrearsci.2012.05.003.
- Akgün, A., Dag, S. and Bulut, F. 2008. Landslide susceptibility mapping for a landslide prone area (Findikli, NE of Turkey) by likelihood frequency Ratio and weighted linear combination models. *Environ. Geol.*, 54(6), 1127–1143.
- Al-Abadi, A.M., 2015. Groundwater potential mapping at northeastern Wasit and Missan governorates, Iraq using a data-driven weights of evidence technique in framework of GIS. *Environ. Earth Sci.*, 74(2), 1109-1124. doi:10.1007/s12665-015-4097-0.
- Althuwaynee, O.F., Pradhan, B., Park, H. and Lee, J.H. 2014. A novel ensemble bivariate statistical evidential belief function with knowledge-based analytical hierarchy process and multivariate statistical logistic regression for landslide susceptibility mapping. *Catena*, 114, 21-36. doi:10.1016/j.catena.2013.10.011.
- Bednarik, M., Magulova, B., Matys, M. and Marschalko, M. 2010. Landslide susceptibility assessment of the Kralovany–Liptovsky´ Mikulaš railway case study. *Phys Chem Earth Parts A/B/C*, 35, 162–171.
- Bonham-Carter, G.F., 1994. *Geographic information systems for geoscientists: modeling with GIS*. Pergamon Press, Ottawa.
- Chandio, I.A., Matori, A.N.B., Wan Yusof, K.B., Talpur, M.A.H., Balogun, A.L. and Lawal, D.U. 2013. GIS based analytical hierarchy process as a multi-criteria decision analysis instrument: a review. *Arab. J. Geosci.*, 6(8), 3059-3066.
- Chen, J., Zhang, Y., Chen, Z. and Nie, Z. 2014. Improving assessment of groundwater sustainability with analytic hierarchy process and information entropy method: A case study of the

- Hohhot Plain, China. *Environ. Earth Sci.*, 73(5), 2353-2363. doi:10.1007/s12665-014-3583-0.
- Chi, K. and Lee, B.J. 1994. Extracting potential groundwater area using remotely sensed data and GIS techniques. In: Proceedings of the Arab J Geosci Author's personal copy Regional Seminar on Integrated Applications of Remote Sensing and GIS for Land and Water Resources Management. Bangkok (Bangkok: Economic and Social Commission for Asia and the Pacific), 64–69.
- Chowdhury, A., Jha, M.K. and Chowdary, V.M. 2010. Delineation of groundwater recharge zones and identification of artificial recharge sites in West Medinipur district, West Bengal, using RS, GIS and MCDM techniques. *Environ. Earth Sci.*, 59(6), 1209-1222. doi:10.1007/s12665-009-0110-9.
- Chung, C.F. and Fabbri, A.G. 2003. Validation of Spatial Prediction Models for Landslide Hazard Mapping. *Nat. Hazards.*, 30(3), 451-472. doi:10.1023/b:nhaz.0000007172.62651.2b
- Constantin, M., Bednarik, M., Jurchescu, M.C. and Vlaicu, M. 2011. Landslide susceptibility assessment using the bivariate statistical analysis and the index of entropy in the Sibiciu Basin (Romania). *Environ. Earth Sci.*, 63, 397–406.
- Dar, I.A., Sankar, K. and Dar, M.A. 2010. Deciphering groundwater potential zones in hard rock terrain using geospatial technology. *Environ. Monit. Assess.*, 173(1-4), 597-610. doi:10.1007/s10661-010-1407-6.
- Davoodi Moghaddam, D., Rezaei, M., Pourghasemi, H.R., Pourtaghi, Z.S. and Pradhan, B. 2013. Groundwater spring potential mapping using bivariate statistical model and GIS in the Taleghan watershed Iran. *Arab. J. Geosci.*, doi:10.1007/s12517-013-1161-5.
- Devkota, K.C., Regmi, A.D., Pourghasemi, H.R., Yoshida, K., Pradhan, B., Ryu, I.C. and Althuwaynee, O. F. 2012. Landslide susceptibility mapping using certainty factor, index of entropy and logistic regression models in GIS and their comparison at Mugling–Narayanghat road section in Nepal Himalaya. *Nat. Hazards.*, 65(1), 135-165. doi:10.1007/s11069-012-0347-6.
- Edet, A.E., Okereke, C.S., Teme, S.C. and Esu, E.O. 1998. Application of remote-sensing data to groundwater exploration: A case study of the Cross-River State, southeastern Nigeria. *Hydrogeo. J.*, 6(3), 394-404. doi:10.1007/s100400050162.
- Fattahi, H., Farsangi, M.A., Shojaee, S. and Mansouri, H. 2014. Selection of a suitable method for the assessment of excavation damage zone using fuzzy AHP in Aba Saleh Almahdi tunnel, Iran. *Arab. J. Geosci.*, 8(5), 2863-2877. doi:10.1007/s12517-014-1280-7.
- Ganapuram, S., Kumar, G.V., Krishna, I.M., Kahya, E. and Demirel, M.C. 2009. Mapping of groundwater potential zones in the Musi basin using remote sensing data and GIS. *Adv. Eng. Softw.*, 40(7), 506-518. doi:10.1016/j.advengsoft.2008.10.001.
- Ghosh, K.G. and Shah, S. 2015. Identification of soil erosion susceptible areas in Hinglo River Basin, Eastern India based on Geo-Statistics. *Uni. J. Environ. R. Techno.*, 5(3), 152-164.
- Greenbaum, D., 1992. Structural influences on the occurrence of groundwater in SE Zimbabwe. Geological Society, London, Special Publications, 66(1), 77-85. doi:10.1144/gsl.sp.1992.066.01.04.
- GSI. 1985. Geological quadrangle map, Bardhaman Quadrangle (73M), West Bengal Bihar. Geological Survey of India, Printing Div. Hyderabad, Govt. of India.
- Gumma, M.K. and Pavelic, P. 2012. Mapping of groundwater potential zones across Ghana using remote sensing, geographic information systems, and spatial modeling. *Environ. Monit. Assess.*, 185(4), 3561-3579. doi:10.1007/s10661-012-2810-y

- Ihara, S., 1993. Information theory for continuous systems. World Scientific Pub Co Inc, Hackensack.
- Jaafari, A., Najafi, A., Pourghasemi, H.R., Rezaeian, J. and Sattarian, A. 2014. GIS-based frequency ratio and index of entropy models for landslide susceptibility assessment in the Caspian forest, northern Iran. *Int. J. Environ. Sci. Technol.*, 11(4), 909-926. doi:10.1007/s13762-013-0464-0
- Jaiswal, R.K., Mukherjee, S., Krishnamurthy, J. and Saxena, R. 2003. Role of remote sensing and GIS techniques for generation of groundwater prospect zones towards rural development--an approach. *Int. J. Remote. Sens.*, 24(5), 993-1008. doi:10.1080/01431160210144543
- Jha, M.K., Chowdary, V.M. and Chowdhury, A. 2010. Groundwater assessment in Salboni Block, West Bengal (India) using remote sensing, geographical information system and multi-criteria decision analysis techniques. *Hydrogeo. J.*, 18(7), 1713-1728. doi:10.1007/s10040-010-0631-z
- Kaliraj, S., Chandrasekar, N. and Magesh, N.S. 2013. Identification of potential groundwater recharge zones in Vaigai upper basin, Tamil Nadu, using GIS-based analytical hierarchical process (AHP) technique. *Arab. J. Geosci.*, 7(4), 1385-1401. doi:10.1007/s12517-013-0849-x
- Kamaraju, M., Bhattacharya, A., Reddy, G.S., Rao, G.C., Murthy, G.S. and Rao, T.C. 1996. Ground-water potential evaluation of West Godavari District, Andhra Pradesh State, India-A GIS Approach. *Ground Water*, 34(2), 318-325. doi:10.1111/j.1745-6584.1996.tb01891.x
- Khodaei, K. and Nassery, H.R. 2011. Groundwater exploration using remote sensing and geographic information systems in a semi-arid area (Southwest of Urmieh, Northwest of Iran). *Arab. J. Geosci.*, 6(4), 1229-1240. doi:10.1007/s12517-011-0414-4
- Krishnamurthy, J. and Srinivas, G. 1995. Role of geological and geomorphological factors in ground water exploration: A study using IRS LISS data. *Int. J. Remote. Sens.*, 16(14), 2595-2618. doi:10.1080/01431169508954579
- Krishnamurthy, J., Kumar, N.V., Jayaraman, V. and Manivel, M. 1996. An approach to demarcate ground water potential zones through remote sensing and a geographical information system. *Int. J. Remote. Sens.*, 17(10), 1867-1884. doi:10.1080/01431169608948744
- Kumar, S.K., Chandrasekar, N., Seralathan, P., Godson, P.S. and Magesh, N.S. 2011. Hydrogeochemical study of shallow carbonate aquifers, Rameswaram Island, India. *Environ. Monit. Assess.*, 184(7), 4127-4138. doi:10.1007/s10661-011-2249-6
- Lee, S. and Pradhan, B. 2006. Landslide hazard mapping at Selangor, Malaysia using frequency ratio and logistic regression models. *Landslides.*, 4(1), 33-41. doi:10.1007/s10346-006-0047-y
- Lee, S., Oh, H. and Park, N. 2006. Mineral Potential Assessment of Sedimentary Deposit using Frequency Ratio and Logistic Regression of Gangreung Area, Korea. *IEEE International Symposium on Geoscience and Remote Sensing*, 1576-1579. doi:10.1109/igarss.2006.406
- Machiwal, D., Jha, M.K. and Mal, B.C. 2010. Assessment of Groundwater Potential in a Semi-Arid Region of India Using Remote Sensing, GIS and MCDM Techniques. *Water Resour. Manage.*, 25(5), 1359-1386. doi:10.1007/s11269-010-9749-y
- Madrucci, V., Taioli, F. and Araújo, C.C., 2008. Groundwater favorability map using GIS multi-criteria data analysis on crystalline terrain, São Paulo State, Brazil. *Hydrogeo. J.*, 357(3-4), 153-173. doi:10.1016/j.jhydrol.2008.03.026
- Magesh, N.S., Chandrasekar, N. and Soundranayagam, J.P. 2011. Morphometric evaluation of Papanasam and Manimuthar watersheds, parts of Western Ghats, Tirunelveli district, Tamil Nadu, India: A GIS approach.

- Environ. Earth Sci., 64(2), 373-381. doi:10.1007/s12665-010-0860-4
- Malczewski, J., 1999. GIS and multicriteria decision analysis (New York: John Wiley and Sons), 392 pp
- Manap, M.A., Nampak, H., Pradhan, B., Lee, S., Sulaiman, W.N. and Ramli, M.F. 2012. Application of probabilistic-based frequency ratio model in groundwater potential mapping using remote sensing data and GIS. Arab. J. Geosci., 7(2), 711-724. doi:10.1007/s12517-012-0795-z
- Manap, M.A., Sulaiman, W.N., Ramli, M.F., Pradhan, B. and Surip, N. 2011. A knowledge-driven GIS modeling technique for groundwater potential mapping at the Upper Langat Basin, Malaysia. Arab. J. Geosci., 6(5), 1621-1637. doi:10.1007/s12517-011-0469-2
- Moghaddam, D.D., Rezaei, M., Pourghasemi, H.R., Pourtaghie, Z.S. and Pradhan, B. 2013. Groundwater spring potential mapping using bivariate statistical model and GIS in the Taleghan Watershed, Iran. Arab. J. Geosci., 8(2), 913-929. doi:10.1007/s12517-013-1161-5
- Mohammady, M., Pourghasemi, H.R. and Pradhan, B. 2012. Landslide susceptibility mapping at Golestan Province, Iran: A comparison between frequency ratio, Dempster-Shafer, and weights-of-evidence models. J. Asian. Earth Sci., 61, 221-236. doi:10.1016/j.jseaes.2012.10.005
- Moore, I.D., Grayson, R.B. and Ladson, A.R. 1991. Digital terrain modelling: A review of hydrological, geomorphological, and biological applications. Hydro. Process., 5(1), 3-30. doi:10.1002/hyp.3360050103
- Mukherjee, A., Fryer, A.E. and Howell, P., 2007. Regional hydro-stratigraphy and ground water flow modeling of the arsenic contaminated aquifers of the western Bengal basin, West Bengal, India. Hydro. J., 15, 1397-1418. https://doi.org/10.1007/s10040-007-0208-7
- Mukherjee, S., 1996. Targeting saline aquifer by remote sensing and geophysical methods in a part of Hamirpur_Kanpur, India. Hydro. J., 19, 1867-1884.
- Naghibi, S.A., Pourghasemi, H.R., Pourtaghi, Z.S. and Rezaei, A., 2014. Groundwater qanat potential mapping using frequency ratio and Shannon's entropy models in the Moghan watershed, Iran. Earth Sci. Inform., 8(1), 171-186. doi:10.1007/s12145-014-0145-7.
- NATMO., 2001. National Atlas and Thematic Mapping Organization, District Planning Map Series (DST), Digital Mapping and Printed Division, Kolkata, Govt. of India.
- Navarro, E.M., Martinez-Perez, S., Sastre-Merlin, A. and Bienes-Allas, R., 2014. Catchment erosion and sediment delivery in a limno-reservoir basin using a simple methodology, Water Resour. Manag., doi:10.1007/s11269-014-0601-7
- Oh, H. and Lee, S., 2010. Assessment of ground subsidence using GIS and the weights-of-evidence model. Eng. Geol., 115(1-2), 36-48. doi:10.1016/j.enggeo.2010.06.015
- Oh, H., Kim, Y., Choi, J., Park, E. and Lee, S. 2011. GIS mapping of regional probabilistic groundwater potential in the area of Pohang City, Korea. J. Hydro., 399(3-4), 158-172. doi:10.1016/j.jhydrol.2010.12.027
- Ozdemir, A., 2011a. Using a binary logistic regression method and GIS for evaluating and mapping the groundwater spring potential in the Sultan Mountains (Aksehir, Turkey). J. Hydro., 405(1-2), 123-136. doi:10.1016/j.jhydrol.2011.05.015.
- Ozdemir, A., 2011b. GIS-based groundwater spring potential mapping in the Sultan Mountains (Konya, Turkey) using frequency ratio, weights of evidence and logistic regression methods and their comparison. J. Hydro., 411(3-4), 290-308. doi:10.1016/j.jhydrol.2011.10.010.

- Pandey, V.P., Shrestha, S. and Kazama, F. 2013. A GIS-based methodology to delineate potential areas for groundwater development: A case study from Kathmandu Valley, Nepal. *Appl. Water Sci.*, 3(2), 453-465. doi:10.1007/s13201-013-0094-1.
- Pourghasemi, H.R., Pradhan, B. and Gokceoglu, C. 2012a. Remote Sensing Data Derived Parameters and its Use in Landslide Susceptibility Assessment Using Shannon's Entropy and GIS. *Appl. Mech. Mater.*, 225, 486-491. doi:10.4028/www.scientific.net/amm.225.486.
- Pourghasemi, H.R., Mohammady, M. and Pradhan, B. 2012b. Landslide susceptibility mapping using index of entropy and conditional probability models in GIS: Safarood Basin, Iran. *Catena.*, 97, 71-84. doi:10.1016/j.catena.2012.05.005.
- Pourghasemi, H.R., Pradhan, B. and Gokceoglu, C. 2012. Application of fuzzy logic and analytical hierarchy process (AHP) to landslide susceptibility mapping at Haraz watershed, Iran. *Nat. Hazards*, 63(2): 965-996. doi:10.1007/s11069-012-0217-2.
- Pourtaghi, Z.S. and Pourghasemi, H.R., 2014. GIS-based groundwater spring potential assessment and mapping in the Birjand Township, southern Khorasan Province, Iran. *Hydrogeo. J.*, 22(3), 643-662. doi:10.1007/s10040-013-1089-6.
- Pradeep Kumar, G.N., Srinivas, P., Jaya Chandra, K. and Sujatha, P., 2010. Delineation of groundwater potential zones using remote sensing and GIS techniques: a case study of Kurmapalli Vagu basin in Andhra Pradesh, India. *Int. J. Water Resour. Environ. Eng.*, 2, 70-78.
- Pradhan, B., 2009a. Groundwater potential zonation for basaltic watersheds using satellite remote sensing data and GIS techniques. *Open Geosci.*, 1(1). Doi: 10.2478/v10085-009-0008-5.
- Pradhan, B., 2013b. A comparative study on the predictive ability of the decision tree, support vector machine and neuro-fuzzy models in landslide susceptibility mapping using GIS. *Comput. Geosci.*, 51, 350-365. doi:10.1016/j.cageo.2012.08.023.
- Pradhan, B., Suliman, M.D. and Awang, M.A., 2007. Forest fire susceptibility and risk mapping using remote sensing and geographical information systems (GIS). *Disaster Prevention and Management.*, 16(3), 344-352. doi: 10.1108/09653560710758297.
- Prasad, R.K., Mondal, N.C., Banerjee, p., Nandakumar, M.V. and Sing, V.S., 2007. Deciphering potential groundwater zone in hard rock through the application of GIS. *Eviron. Geol.*, 55(3), 467-475. Doi: 10.1007/s00254-007-0992-3.
- Rahmati, O., Samani, A.N., Mahdavi, M., Pourghasemi, H.R. and Zeinivand, H., 2014. Groundwater potential mapping at Kurdistan region of Iran using analytic hierarchy process and GIS. *Arab. J. Geosci.*, 8(9), 7059-7071. doi: 10.1007/s12517-014-1668-4.
- Rao, Y.S. and Jugran, D.K., 2003. Delineation of groundwater potential zones and zones of groundwater quality suitable for domestic purposes using remote sensing and GIS. *Hydro. Sci. J.*, 48(5), 821-833. doi:10.1623/hysj.48.5.821.51452.
- Ravi Shankar, M.N. and Mohan, G. 2006. Assessment of the groundwater potential and quality in Bhatsa and Kalu river basins of Thane district, western Deccan Volcanic Province of India. *Environ. Geol. J.*, 49, 990-998.
- Ray, A. and Shekhar, S., 2009. Ground water issues and development strategies in west Bengal. *Bhu Jal News.*, 24 (1), 1-17.
- Regmi, A.D., Devkota, K.C., Yoshida, K., Pradhan, B., Pourghasemi, H.R., Kumamoto, T. and Akgun, A., 2013. Application of frequency ratio, statistical index, and weights-of-evidence models and their comparison in landslide susceptibility mapping in Central Nepal Himalaya.

- Arab. J. Geosci., 7(2), 725-742. doi:10.1007/s12517-012-0807-z
- Roy, J. and Saha, S., 2018. Assessment of land suitability for the paddy cultivation using analytical hierarchical process (AHP): A study on Hinglo river basin, Eastern India. *Model. Earth Syst. Environ.*, 4(2), 601-618. doi:10.1007/s40808-018-0467-4
- Saaty, T.L., 1980. *The analytical hierarchy process*. McGraw Hill, New York, 350 pp
- Saaty, T.L., 1990. *The analytic hierarchy process: planning, priority setting, resource allocation*, 1st edn. RWS Publications, Pittsburgh, 502 pp
- Saaty, T.L., 1994. *Fundamentals of decision making and priority theory with analytic hierarchy process*, 1st edn. RWS Publications, Pittsburgh, 527 pp
- Saha, S., 2017. Groundwater potential mapping using analytical hierarchical process: A study on Md. Bazar Block of Birbhum District, West Bengal. *Spat. Inf. Res.*, 25(4), 615-626. doi:10.1007/s41324-017-0127-1
- Sahu, P. and Sikdar, P.K., 2010. Groundwater potential zoning of a peri-urban wetland of south Bengal Basin, India. *Environ. Monit. Assess.*, 174(1-4), 119-134. doi:10.1007/s10661-010-1443-2
- Sander, P., Chesley, M.M. and Minor, T.B., 1996. Groundwater Assessment Using Remote Sensing and GIS In A Rural Groundwater Project In Ghana: Lessons Learned. *Hydrogeo. J.*, 4(3), 40-49. doi:10.1007/s100400050086
- Saraf, A.K. and Choudhury, P.R., 1998. Integrated remote sensing and GIS for groundwater exploration and identification of artificial recharge sites. *Int. J. Remote Sens.*, 19(10), 1825-1841. doi:10.1080/014311698215018
- Sener, E., Davraz, A. and Ozcelik, M., 2005. An integration of GIS and remote sensing in groundwater investigations: A case study in Burdur, Turkey. *Hydrogeo. J.*, 13(5-6), 826-834. doi:10.1007/s10040-004-0378-5
- Solomon, S. and Quiel, F., 2006. Groundwater study using remote sensing and geographic information systems (GIS) in the central highlands of Eritrea. *Hydrogeo. J.*, 14(6), 1029-1041. doi:10.1007/s10040-006-0096-2
- Suja Rose, R.S. and Krishnan, N., 2009. Spatial analysis of groundwater potential using remote sensing and GIS in the Kanyakumari and Nambiyar basins, India. *J. Indian Soc. Remote Sens.*, 37, 681-692.
- Todd, D.K. and Mays, L.W., 2005. *Ground water hydrology*. Wiley, New York, 652 pp
- Waikar, M.L. and Aditya, P.N., 2014. Identification of Groundwater Potential Zone using Remote Sensing and GIS Technique, *Int. J. Int. Res. Scien. Engin. Techno.*, 3(5), 12163-12174.
- Wu, Q. And Wang, M., 2007. A framework for risk assessment on soil erosion by water using an integrated and systematic approach. *J. Hydro.*, 337(1-2), 11-21. doi:10.1016/j.jhydrol.2007.01.022.
- Yang, Q., Xie, Y., Li, W., Jiang, Z., Li, H. and Qin, X., 2013. Assessing soil erosion risk in karst area using fuzzy modeling and method of the analytical hierarchy process. *Environ. Earth Sci.*, 71(1), 287-292. doi:10.1007/s12665-013-2432-x
- Yesilnacar, E.K., 2005. *The application of computational intelligence to landslide susceptibility mapping in Turkey*. PhD Thesis. University of Melbourne, Australia, -423pp
- Yilmaz, I., 2009. Landslide susceptibility mapping using frequency ratio, logistic regression, artificial neural networks and their comparison: A case study from Kat landslides (Tokat—Turkey). *Comput. Geosci.*, 35(6), 1125-1138. doi:10.1016/j.cageo.2008.08.007

Youssef, A.M., Pradhan, B. and Tarabees, E., 2011. Integrated evaluation of urban development suitability based on remote sensing and GIS techniques: Contribution from the analytic hierarchy process. Arab. J. Geosci., 4(3-4), 463-473. Doi: 10.1007/s12517-009-0118-1

Yufeng, S. and Fengxiang, J., 2009. Landslide Stability Analysis Based on Generalized Information Entropy. 2009 International Conference on Environmental Science and Information Application Technology., doi:10.1109/esiat.2009.258

Received on: 21.2.19; Revised on: 28.5.19; Accepted on: 6.8.19

Validation of model-based techniques for characterization of surface sediments at Khadakwasala Lake using field Data

Jyoti Sadalage^{1*}, Rashmi Sharma², Arnab Das³, and Yashwant Joshi⁴

¹Department of Electronics and Telecommunication Engineering, VPKBIET, Baramati, Maharashtra, 413133, India

^{2,4} Department of Electronics and Telecommunication,

Shri Guru Gobind Singhaji Institute of Engineering & Technology, Nanded, 431606, Maharashtra, India

³ Maritime Research Center, Pune, Maharashtra, 411006, India

*Corresponding Author: jyoti.rangole@vpkbiet.org

ABSTRACT

Siltation is a major concern for the freshwater systems, located in the tropical region. The precise characterization of the sediment type is critical for initiating any de-siltation effort, or even to ascertain the siltation process for introducing any preventive measures. The sediment grain size determines the characteristics of the sediment composition at the surface, as well as the deep layers. In this work, we carried out surface sediment characterization at Khadakwasala Lake, using the analytical data, acquired by EdgeTech SB216S sub-bottom profiler. The experimental site is a freshwater lake, located at the Pune city in the state of Maharashtra, India, which is critical for the domestic water supply of the city. This paper presents validation of two model-based techniques viz. energy model and central frequency shift model, to characterize the surface sediment at Khadakwasala Lake. Energy model showed the reflection coefficients less than 0.2 over the most part of the survey area. The reflection coefficients calculated using energy model, are sensitive to the length of the window used for the signal energy calculation. An alternative model, based on the central frequency shift and relaxation time, is also used in this paper to cross-validate the results. The model showed a frequency shift of -3 Hz/m to -37Hz/m through the underlying sediment. The laboratory testing results of the acquired sediment samples at five different locations showed a good match with the central frequency shift model.

Keywords: Siltation, Acoustic technique, Model-Based methods, Surface sediment characterization, Khadakwasala Lake.

INTRODUCTION

The Indian sub-continent receives the majority of its freshwater during the monsoon season (almost 75%). Rest of the months are usually dry, which requires the utilization of groundwater or put away water during the monsoons. The sediments amassed during the supply, reduces the water stocking limit of the dam, which makes sedimentation a major issue for the water management (McCully and Books, 1996). To restore the limits of the reservoir storage capacity, de-siltation is required to be done at regular intervals. This requires detailed knowledge of the sediment topography and detailed information about the sediment composition, both at the surface

and at deeper layers of the selected site. The conventional method to ascertain the sediment composition is to grab the physical sediment samples, however, this method is costly and also tedious. Much compelling acoustic survey strategies utilize the dynamic sonar systems, like Multi-Beam Echo-Sounders (MBESs), Side-Scan Sonar (SSSs) and Sub-Bottom Profilers (SBPs) for sediment classification.

A few geo-acoustic models exist in the literature that effectively represent the propagation of sound in the sediment (LeBlanc et al., 1992; Stevenson et al., 2002; Etter, 2003; Saleh and Rabah, 2016). The type of sediments can be investigated by empirically relating geo-acoustic and geo-physical

properties of the sediments. The Biot-Stoll model has been widely used to relate sediment geoaoustic properties to geo-physical properties on the basis of physical principles. Sediment geophysical parameters can also be generated from bottom loss, using inverse technique (Etter, 2003). Leblanc et al. (1992) have discussed the standard methods for determination of sediment attenuation, including the rise time, the spectral ratio, spectrum modeling and wavelet modeling. LeBlanc et al. (1992) developed an attenuation-based sediment classification model, which measures the center frequency shift of the pulse spectrum, using an instantaneous frequency method to estimate the relaxation time. The relaxation-time model was used to study the dispersion and attenuation characteristics of the correlated chirp sonar pulse. A similar method was adopted by Stevenson et al. (2002) for chirp sub-bottom profiler data, where attenuation measurements were obtained for each stratigraphic unit within a complex, thinly interbedded sedimentary sequence. The physics based model (Walree and Ainslie, 2006) describes the received echo energy as a function of transmitted signal energy, water column losses, water depth and sediment reflection coefficient.

The proposed work presents the analysis of the reflection coefficients of the surface sediment at Khadakwasla Lake. The chirp sub-bottom profiler used in this study transmits Gaussian-shaped frequency modulated pulse, to obtain high resolution and enhanced sediment penetration. The chirp signal penetrates the sub-bottom layers, the received echoes reflected from the layered sediments give information about sediment layer structure and type. Since the geophysical and geoaoustic properties of sediment are correlated, the reflection coefficients are computed where there is high impedance contrast, and are then matched with the mean grain size of the sediment.

The energy model is used here to calculate the reflection coefficients, using the spherical spreading loss by considering variations in absorption coefficient (Walree and Ainslie, 2006). The calculated reflection coefficients are compared with Hamilton and Bachman's (1972) model for predicting the sediment type. In this paper, we also used the central frequency shift method to estimate surface sediment type. Besides, this paper also discusses, survey area, survey details, acoustic data interpretation, pre-processing, and the models used for sediment characterization, apart from simulation results.

METHODOLOGY

Study Area and Survey details

The Khadakwasla Lake is located at latitude and longitude of 18.4324°N and 73.7625°E respectively. The lake spans nearly 17 km length with width of about 250 m to 1000 m. The total catchment area is about 501 sq. km. The maximum depth of the lake is 36 m, as reported in the literature (National Defence Academy). The siltation rate of the lake is 23.920 ha-m/100 sq.km/yr. (<http://shodhganga.inflibnet.ac.in>). The data collection was undertaken on 11 Oct and 12 October 2017, over full day with a varying transmission pattern. The acoustic survey was carried out over a distance of ~4 km. The geographical location of the survey region is shown Figure 1a. The EdgeTech sub-bottom profiler SB216S was deployed along with MK III single-beam echo-sounder. The Gaussian chirp signal frequency was set at 2 kHz to 10 kHz, with pulse duration of 20 ms and the sampling frequency of 25 kHz. The transmitted signal power was set at 210 dB. We found the water depth over the survey track between 8 m and 15 m, whereas maximum penetration recorded was 3 m to 4 m below the top

layer of sediment. The acoustic survey was carried out at an approximate speed of 3-4 knot with ping frequency of 1 Hz. We collected surface sediment samples from locations G1 to G5 using the Van

Veen grabber, the locations could be seen on google earth (Figure 1b). The surface sediment samples were tested at Geo-tech Laboratory of Fugro India.

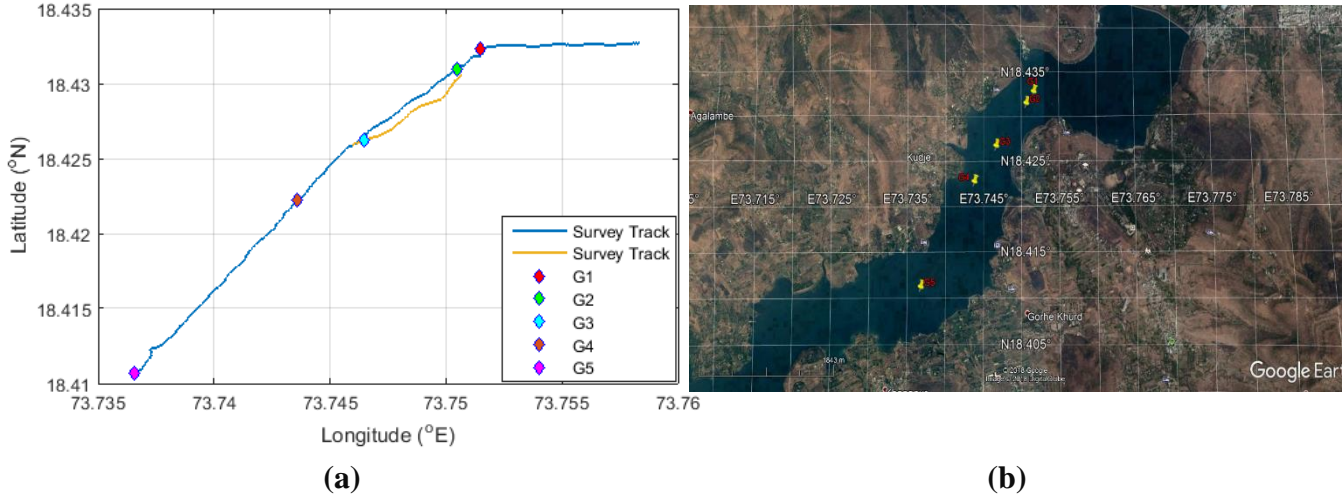


Figure 1. (a) Surveyed zone located in Khadakwasala Lake, (b) Grab locations on google earth

Acoustic Data and Pre-processing

Acoustic signals, recorded during the experiment were in complex analytical form as shown in the equation (1)

$$z(t) = s(t) + j \hat{s}(t) \quad (1)$$

where $s(t)$ is the real part of the analytical signal, while $\hat{s}(t)$ is the Hilbert transform of $s(t)$.

The analytical signal $z(t)$ can also be represented as follows,

$$z(t) = E(t) e^{j\phi(t)} \quad (2)$$

where $E(t)$ envelope is function and $\phi(t)$ is the phase. The real part of the analytical signal is used as the input to the pre-processing stage.

Band-pass filter

The transmitted signal gets influenced by many physical processes during propagation. In order to omit the presence of undesired frequencies, the signals are passed through a band-pass filter, which allows the frequencies within a certain band pass

through it, while frequencies outside that range are attenuated. We have used Butterworth band-pass filter with order 20, length of impulse response 154 and lower and upper cut-off frequency of 2 kHz and 10 kHz respectively.

Stack alignment and averaging

The data is heave-compensated by the heave sensor during the recording; still, there is some heave visible over consecutive pings. The returns from the same surface may appear different, this variability in data could influence the results. If the echo envelopes are averaged over some ensemble size, this effect could be reduced. The ensemble size is chosen based on the inter-ping variance. The averaging of samples is effective only when the samples are aligned, either with their peaks or the initial rise, prior to the averaging process.

Sample size selection

Calculation of reflection coefficients of a layer is valid only when reflections from other layers are not located within the sampling window of the first

arrival pulse. The spectral analysis of the signals in two consecutive windows could be used to analyse the variation or shift of the spectrum. The spectra are calculated over a window size of 0.5 ms, the assumption here is that the low power resulting from the second window is the sediment absorption influence on the transmitted signal within a homogeneous layer which indicated that we have the same layer and if the spectrum of the second window is wider than the prior one, it indicates that the secondary reflection is encountered which implies the presence of another layer.

Model-Based Techniques for Sediment Classification

Energy model

The received signals from a sub-bottom profiler consist of reflections from the surface as well as sediment layers. The energy model (Walree and Ainslie, 2006) predicts the reflection coefficients at the surface layer, which are further mapped to the corresponding mean grain size, using an empirical relationship. In shallow water channels, the transmission losses are dominant, which can be estimated by adding the effects of geometrical spreading, absorption and scattering (Lurton, X., 2002). To discriminate between the energy loss due to transmission, and attenuation, the energies are corrected for the spherical spreading and water absorption. The model basically computes received energy by squaring and integrating the echo envelope in the window by extracting the signals from recordings and finds the corresponding reflection coefficients (Snellen et al., 2011). The received echo energy E_{rx} at a given direction is related to the transmitted pulse E_{tx} through equation (3),

$$E_{rx} = \frac{e^{-2\alpha H}}{4H^2} R^2 E_{tx} \quad \dots \dots \quad (3)$$

Here, H denotes the distance between the echo sounder and the seafloor determined from the echo return time and the sound speed obtained from SBES and R is the reflection coefficient of the smooth surface. The received echo energy is corrected for spherical spreading by using correction value $1/4H^2$ in equation (3). The correction for the water absorption is $e^{-4\alpha H}$, the exponential form that computes the absorption rate proportional to water depth, where α is the water absorption coefficient estimated from Francois and Garrison (1982) model. The reflection coefficient can be easily estimated by using the equation (3). The modeled reflection coefficients corresponding to assumed sediment types can be described via the classic Rayleigh reflection law, which is a function of the impedance ratio between two mediums given by the equation (4),

$$R_{ws1} = \frac{Z_s - Z_w}{Z_s + Z_w} \quad \dots \dots \quad (4)$$

where Z_s and Z_w is the sediment impedance and the water impedance respectively. The acoustic impedance is a function of the water sound speed C_s and density ρ_s . The Bachman and Hamilton regression equations relate the sediment velocity and density to the mean grain size as shown in the equation (5) and (6) respectively,

$$C_s = 1952 - 86.3M_z + 4.41 M_z^2 \quad \dots \dots \quad (5)$$

$$\rho_s = 2380 - 172.5M_z + 6.89 M_z^2 \quad \dots \dots \quad (6)$$

where C_s is the sediment sound speed and ρ_s is the sediment density. The acoustic impedance of the sediment Z_s can be calculated from the equation (5) and (6) and is related as $Z_s = C_s \rho_s$.

Relaxation time model

The relaxation time is a measure of finite time needed to change the density by application of sudden pressure. The attenuation α (dB/m) and the

relaxation time τ (μs) are related as shown in the equation (7)

$$\alpha \approx \omega^2 \tau / 2v \quad \dots\dots (7)$$

where v is adiabatic sound speed, ω is the frequency in radians/sec. For lower frequencies, attenuation coefficient varies as the square of the frequency. The attenuation for different sediment types is calculated by using the equation (7). The frequency dependence of the attenuation for different sediment types including, sand ($\tau = 0.16 \mu\text{s}$), silt ($\tau = 0.06 \mu\text{s}$) and clay ($\tau = 0.02 \mu\text{s}$) is presented (Figure 2).

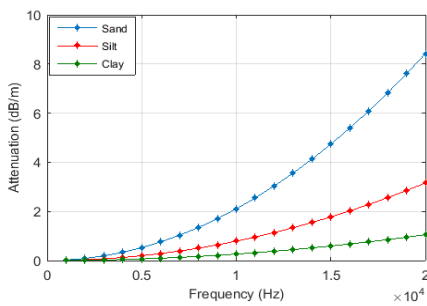


Figure 2. Sediment attenuation as a function of distance travelled for different sediment types

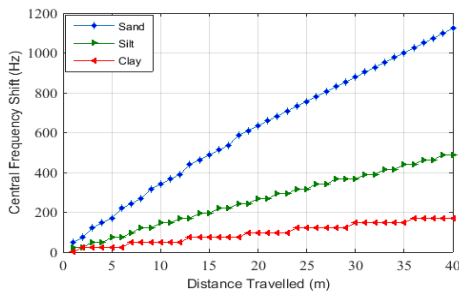


Figure 3. Central frequency shift as a function of frequency

The sound speed is set at a nominal value of 1500 m/s. Leblance et al.(1992) presented the regression model showing the relation between relaxation time τ and the grain size Φ as given by the equation (8),

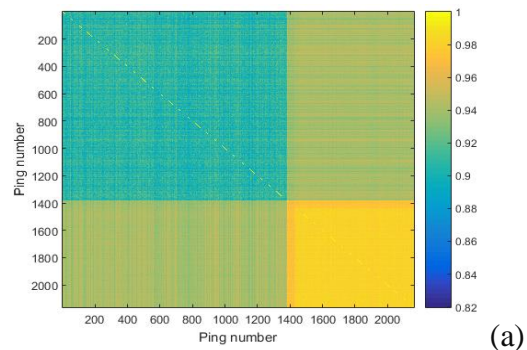
$$\tau = 0.0848(\phi - 0.415)e^{-0.0437(\phi-0.415)^2} \dots (8)$$

Leblance et al. (1992) also presented the use of the instantaneous frequency of the sub-bottom pings in sediment classification. The instantaneous

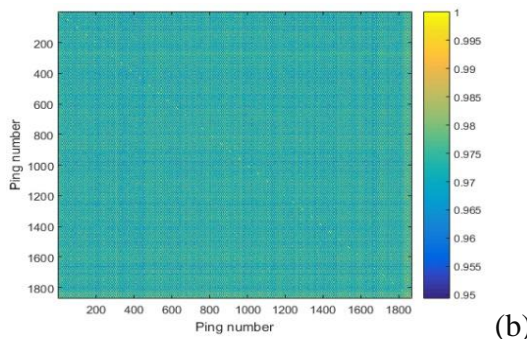
frequency of the analytical signal is given by equation (9),

$$f_i = \frac{1}{2\pi} \frac{\partial \phi}{\partial t} \quad \dots\dots (9)$$

The local mean value of the instantaneous frequency represents the central frequency of the spectrum of the sub-bottom pulse correlator output. The shift in the central frequency is a significant parameter that can be used for sediment classification. Figure 3 presents shift in the central frequency as a function of distance travelled for different sediment types.



(a)



(b)

Figure 4. Inter-ping correlation coefficient matrix at survey area

RESULTS AND DISCUSSION

The first step in pre-processing is the application of the bandpass filter to echo signals. The echo signal is filtered using the Butterworth band-pass filter with bandwidth 8 kHz. The next step is echo alignment and averaging. We have used the minimum threshold (10%) alignment technique for stacking the echo envelopes. Minimum threshold

alignment preserves the integrity of the echo's rising edge, which is more suitable for bottom echoes that have low stochastic variability and is less suitable for noisy signals or bottom echoes from rough sediments, whereas peak alignment is more suitable for bottom echoes that have high stochastic variability such as high noise or echoes from rough sediments. As the data we collected from the lake, has low stochastic variability we have chosen minimum (10%) threshold alignment. Echo signal alignment, stacking and averaging are done for treating the stochastic behavior of received signals, thus removing the effect of the transducer heave and variation of depth over consecutive pings (Sternlicht and Christian, 2003). Prior to the averaging process, the echoes with a chosen ensemble size are aligned in time. The ensemble

size is chosen based on the correlation of signals which is obtained by computing the correlation coefficient matrix of received filtered echoes. We found the inter-ping correlation coefficient values at location 1 higher than 0.9 and same is observed for location 2 pings, as shown in Figure 4a and Figure 4b. Thus, any stack size can safely be used in these two areas without influencing the signal properties. The ensemble size of 20 pings has been chosen for averaging. The time window of 0.5 ms has been chosen for the calculation of reflection coefficients based on the Welch spectrum analysis. Figure 4a and 4b shows data correlation coefficient matrix for echo signals at survey areas. The echo signal averaged over 20 pings is as shown in Figure 5a. The instantaneous frequency, calculated using the Hilbert transform is as shown Figure 5b.

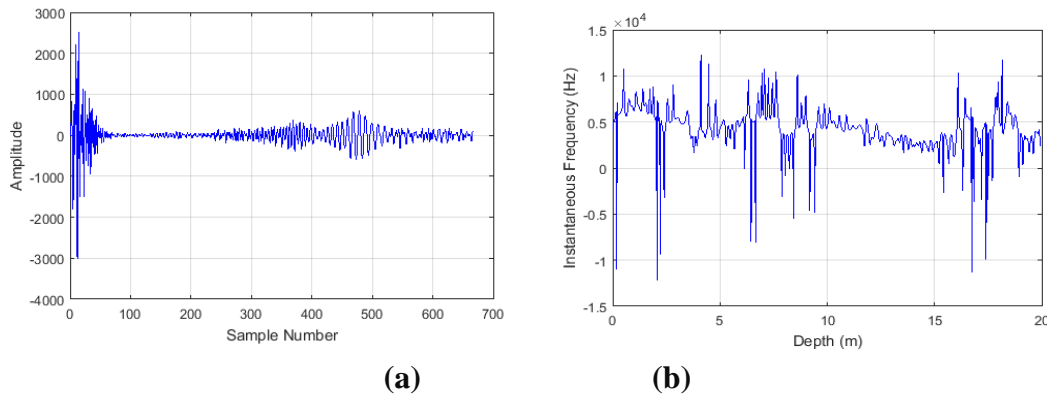


Figure 5. (a) Raw data averaged over 20 pings, (b) Instantaneous frequency as a function of depth

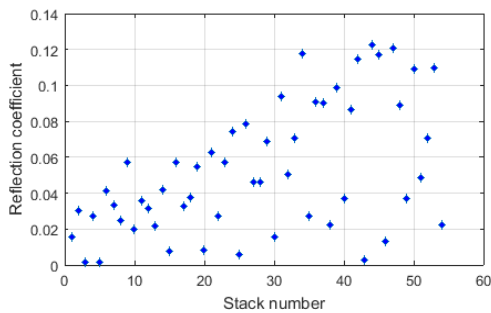


Figure 6. Estimated reflection coefficients in survey region

The x-axis represents the depth which is calculated by considering the time and a nominal sound speed 1500 m/s. The reflection from the water column and

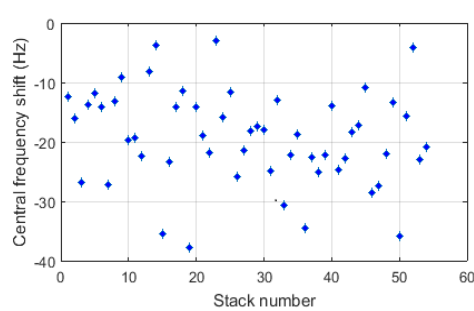


Figure 7. Estimated central frequency shift in survey region

the direct arrival could be observed up to 10 m depth. The depth from 10 m to 15 m shows a gradual decrease in instantaneous frequency. The shift in

central frequency per meter depth, can be used to predict the type of sediment. Similarly, the least square regression is carried out to find the rate of change of the instantaneous frequency with depth. The regression analysis is carried on the instantaneous frequency for the depth in the range 10 m to 15 m. The reflection coefficients of the surface sediment at the survey locations are shown in Figure 6. According to Hamilton's model, it could be predicted that the survey area is populated mostly with clay and the silty clay. The simulation result shown in Figure 7 indicates that the central frequency shift is in the range from -3 Hz/m to -37 Hz/m.

The central frequency shift model result showed that the surface sediment type at survey area could be clay or fine/coarse silt. The central frequency shift values

are further mapped to the grain size (Φ units). We used Wentworth scale (Poppe et al., 2000) for classifying and describing sediment type from the grain size.

As per on-boat visual inspection of grabber sample by the geologist, it was observed that the surface sediment type was laminated clay, coarse clay, and clay with laterite, one of the sample could be seen in Figure 8. The laboratory test results of particle size distribution at five different locations is given in Table 1. The particle size is expressed as diameter 'D' in mm. The laboratory results of sediment classification are based on the grain diameter as follows: Clay (< 0.002), Silt (0.002 to 0.075), Sand (0.075 to 4.75), Gravel (> 4.75).



Figure 8. Grabber sample collected during the survey

Table 1. Comparison of the model results with laboratory results

Sample number	Estimated sediment type using energy-model	Estimated sediment type using central frequency shift method	Particle size distribution (%) according to laboratory testing					
			Clay	Silt	Sand			Gravel
					Fine	Medium	Coarse	
1	Clay	Clay	48	50	2	0	0	0
2	Clay	Fine silt	64	36	0	0	0	0
3	Clay	Medium silt	59	41	0	0	0	0
4	Clay	Medium to fine silt	46	46	6	2	0	0
5	Clay	Clay	54	46	0	0	0	0

CONCLUSIONS

Remote sediment characterization is of great importance in the de-siltation effort. The proposed work presented a pilot experimental study, using acoustic technique for analysis of the surface sediment at Khadakwasala Lake, which would guide the policymakers during the de-siltation planning. The energy model used in this work takes care of losses in water, as well as spherical spreading incorporated during the propagation of sound. The results presented by using the energy model found to be sensitive to the window width over which the received energy is calculated. The central frequency shift model results showed good agreement with the visual perception, as well as the ground truth processed in the laboratory. The slight difference in the central frequency shift model results with the core, may be caused due to sediment disturbance during core collection, navigation errors and natural variability. The study showed that most of the survey area was populated with clay and silt.

Compliance with Ethical Standards

The authors declare that they have no conflict of interest and adhere to copyright norms.

ACKNOWLEDGEMENT

The authors would like to thank Maritime Research Center, Pune for technical guidance and financial support in planning and execution of the experiment. The project was partially financed by Board of College and University Development, Savitribai Phule Pune University.

REFERENCES

Complete information on fresh water resources of India, Available at: <http://www.presservearticles.com/2012021323179/complete-information-on-fresh-water-resources-of-india.html>.

Etter, P., 2003. Underwater acoustic modeling and simulation, 4th edition, Spon Press, Taylor and Francis Group, ISBN 0-203-41765-8.

Francois, R. and Garrison, G., 1982. Sound absorption based on ocean measurements: Part I: Pure water and magnesium sulfate contributions, *J. Acoustical Soc. America*, 72(3), 896-907.

LeBlanc, L., Panda, S. and Schock, S., 1992. Sonar attenuation modeling for classification of marine sediments, *J. Acoustical Soc. America*, 91(1), 116-126.

Lurton X., 2002. An introduction to underwater acoustics: Principles and application, 2nd edition, Springer New York, ISBN: 9783540784807, 3540784802.

McCully, P. and Books, Z., 1996. Sedimentation problems with dams excerpt from silenced rivers: The Ecology and Politics of Large Dams, Available at: <https://www.internationalrivers.org/sedimentation-problems-with-dams>.

National Defence Academy, Available at: <http://www.nda.nic.in>.

Poppe, L., Eliason, A., Fredericks, J., Rendigs, R., Blackwood, D. and Polloni, C., 2000. USGS east-coast sediment analysis-Procedures, database, and georeferenced displays, U.S. Geol. Survey Open File Rep. 00-358.

Sternlicht, D. and Christian, P., 2003. Time-dependent seafloor acoustic backscatter (10–100 kHz), *J. Acoustical Soc. America*, 114(5), 2709-2725.

Stevenson, I., McCann, C. and Runciman, P., 2002. An attenuation-based sediment classification technique using chirp sub-bottom profiler data and laboratory acoustic analysis, *Marine Geophys. Res.*, 23, 277-298.

Saleh, M. and Rabah, M., 2016. Seabed sub-bottom sediment classification using parametric sub-bottom profiler, *NRIAG J. Astronomy and Geophys.* 5(1), 87-95.

Snellen, M., Siemes, K. and Simons, D., 2011. Model-based sediment classification using single-

beam echo sounder signals, *J. Acoustical Soc. America*, 129(5), 2878-2888.

Walree, V. and Ainslie, P., 2006. Mean grain size mapping with single-beam echo sounders, *J. Acoustical Soc. America*, 120(5), 2555-2566.

Received on: 24.1.19; Revised on: 7.6.19; Accepted on: 17.7.19

Assessing groundwater potential zones using remote sensing, GIS and MIF techniques: Renigunta area, Andhra Pradesh

E. Balaji^{1*}, G. Veeraswamy¹, A. Narsimha², M. Rajasekhar³ and R. Siddi Raju³

¹Department of Geology, Sri Venkateswara University, Chandragiri Road, Tirupati, 517502, Andhra Pradesh, India

²School of Environmental Science and Engineering, Chang'an University, No. 126 Yanta Road, Xi'an, 710054, Shaanxi, P.R. China

³Department of Geology, Yogi Vemana University, Vemanapuram, Kadapa, 516003, Andhra Pradesh, India

*Corresponding author: balajiyvu@gmail.com

ABSTRACT

Groundwater potential zones of Renigunta area have been evaluated using an integration of remote sensing, GIS and MIF techniques. Survey of India (SOI) toposheets, IRS-R2 LISS-IV satellite imagery and supplementary datasets from various organizations were used to generate different thematic maps such as geology, geomorphology, drainage density, lineament density, soils, slope and land use/land cover. Then, each thematic map and their subclasses were assigned a weight and rating by using multi influencing factor (MIF) technique and integrated using the weighted overlay process in GIS. The study results into four categories viz., poor 46.46 km² (21.75%), moderate 109.99 km² (51.49%), good 51.62 km² (24.17%) and very good 5.53 km² (2.59%) groundwater potential zones. The final groundwater potential zones map may be useful for policymakers in planning and management scenario of groundwater resources of the study area.

Keywords: Groundwater potential zones, Remote Sensing, Geographic information system (GIS), multi- influencing factor (MIF), weighted overlay technique, Renigunta.

INTRODUCTION

In India, about 80-85% of the drinking water and about 60% of the agricultural needs are being met from the groundwater (The World Bank, 2010; Chaudhary and Kumar, 2018). The increased usage of groundwater than the rate of replenishment leads to exploitation of groundwater on a large scale which typically directs the water table to go down. This is a very common issue in arid and semi-arid regions. Therefore, proper tools in evaluating groundwater resources are required to overcome the difficulties in such terrains. Remote sensing and GIS have proved as reliable tools in conserving and evaluating water resources in a rapid and cost-effective manner.

So far, the researchers used various techniques to delineate groundwater potential zones for instance, fuzzy logic (Aouragh et al., 2016; Tiwari et al., 2017), multi influence factor (MIF) (Thapa et al., 2017; Nasir et al., 2018; Balaji et al., 2019a), statistics (Moghaddam et al., 2013; Arabameri et al., 2019), modelling (GhorbaniNejad et al., 2016; Sashikkumar et

al., 2017), analytical hierarchy process (AHP) (Shekhar and Pandey, 2015; Panahi et al., 2017; Mohammadi-Behzad et al., 2018) and electrical resistivity tomography (Rai and Thiagarajan, 2019). Among which, MIF is a simple, trustworthy and cost-effective, it is therefore adopted in the current research.

The major part of the study area Renigunta is occupied by a crystalline rock formation. Shales/phyllites and quartzites confined to northern portions, whereas the alluvium is restricted to small portions. Major part is occupied by a crystalline rock environment, which has negligible porosity values. The occurrence and movement of groundwater in such environments have been controlled by secondary porosity in the form of weathered zones, fractures, faults and fissures. The study area has a semi-arid climate, where the impact on groundwater linked to rainfall is prominently felt. Agriculture is the major land use practice in the study area and the water to be obtained by groundwater structures due to uncertainties in surface water. Being nearby pilgrim places the

demand for residential land has been accelerating at a constant rate. It is therefore proper awareness on the classification of areas in terms of groundwater potential zones is required. Hence, the tools such as RS, GIS and MIF were used in this investigation.

STUDY AREA

Renigunta area is to be found in between North latitudes 13°33' and 13°47' and East longitudes 79°24' and 79°34' (Figure 1). It is covered by the survey of India toposheets 57 O/5 57 O/6, 57 O/9 and 57 O/10. The study area is nearby the pilgrim places namely Srikalahasti and Tirupati, which has good road, rail and air connectivity as well. The altitude of the area varies between 50 to 500m from the mean sea level. Steep slopes confined to northern portions and southern parts have gentle slopes. Geology of the study area comprises of hornblende-biotite gneiss, granodiorite and granitoid gneiss of Archaean age, quartzites and shales/phyllites of middle Proterozoic age and recent alluvium deposits along the Swarnamukhi River course (Balaji et al., 2019b). The area experiences a semi-arid climate and the mean annual rainfall is around 943mm. The extent of the study area is 213.60 km². Groundwater level varied from 2 to 13m below ground level.

METHODOLOGY

Indian Remote Sensing satellite (IRS-R2 LISS-IV) imagery for the year 2012, toposheets from Survey of India (SOI) with numbers 57 O/5 57 O/6, 57 O/9 and 57 O/10 in 1,50,000 scale, ASTER DEM 30 m resolution and secondary data from various sources, have been used in this study. Drainage map was prepared from the toposheets and checked for spatial discrepancy using satellite image. Geology and soils maps were prepared using

maps published by Geological Survey of India (GSI) and field observations. Lineaments and slope maps were generated using ASTER DEM 30m resolution. The geomorphology and land use/land cover maps were prepared using satellite imagery and survey of India toposheets. Lineament density and drainage density maps were generated using the line density tool in GIS. Individual thematic map and their subclasses were given suitable weight and rating by using multi influence factor (MIF) technique and the integration process was performed using the weighted overlay process in GIS. A minor effect was given 0.5 weight and the major effect was given a weight of 1.0 (Table 1). Each thematic map, their subclasses, weights and scores were depicted in Table 2. Nasir et al., (2018) suggested a formula for the calculation of individual weight for thematic maps, as given below

The Individual Weight for a thematic unit

$$= \frac{(A + B)}{\sum(A + B)} \times 100$$

Where A is a major effect weight and B is a minor effect weight

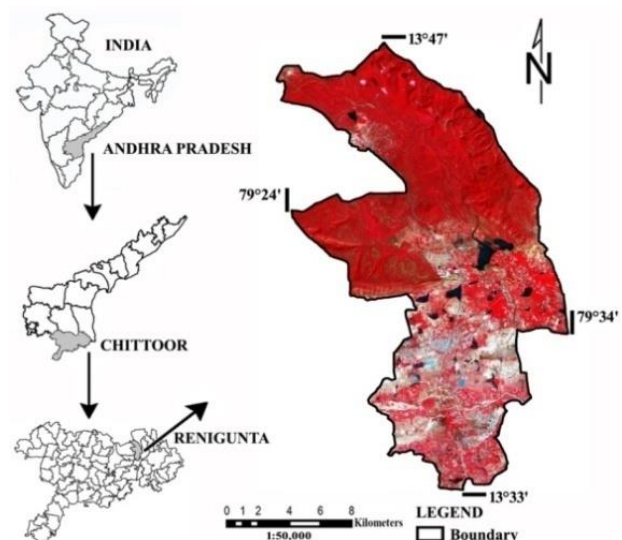


Figure 1. Location map of the study area

Table. 1 Major, minor effects and assigned weights for influential parameters

Influential parameters	Weight assigned for Major effect (A)	Weight assigned for Minor effect (B)	Total Weight (A+B)	Assigned weight for each influential parameter $100 \times \frac{A+B}{\sum(A+B)}$
Geology	4	0	4	26
Lineament density	3	0	3	19
Geomorphology	2	0	2	13
Land use/ land cover	1	0.5+0.5	2	13
Drainage density	2	0	2	13
Slope	1	0.5	1.5	10
Soil	1	0	1	6
Total			$\sum 15.5$	$\sum 100$

Table. 2 Weights and ratings for influential parameters and its subclasses

Factors	Subclasses	Weight	Rating
Geological units	River	26	26
	Granites/gneisses		12
	Shales/Phyllites		9
	Quartzites		7
Lineament density	High	19	19
	Medium		9
	Low		1
Geomorphology	Valley fill	13	13
	Bajada		13
	Channel bar		13
	Water bodies		13
	Pediplain deep weathered		12
	Pediplain moderate weathered		10
	Pediplain shallow weathered		7
	Piedmont slope		4
	Structural hills/ Residual hills/ Inselberg		1
	Pediments/ Escarpment slope		1
Land use/land cover	Water bodies	13	13
	Forest		11
	Agriculture		8
	Wastelands		4
	Settlements		1
Drainage density	High	13	1
	Medium		7
	Low		13
Slope	High	10	1
	Moderate		5
	Low		10
Soil	Dark reddish brown deep gravelly loam soils	6	6
	Red shallow gravelly loam soils		6
	Red shallow gravelly clay soils		4
	Dark brown deep clayey soils		2
	Red clay soils		2

The proposed methodology in this study is depicted in Figure 2, the major, minor effects and their relationship linked to its groundwater prospects is shown in Figure 3.

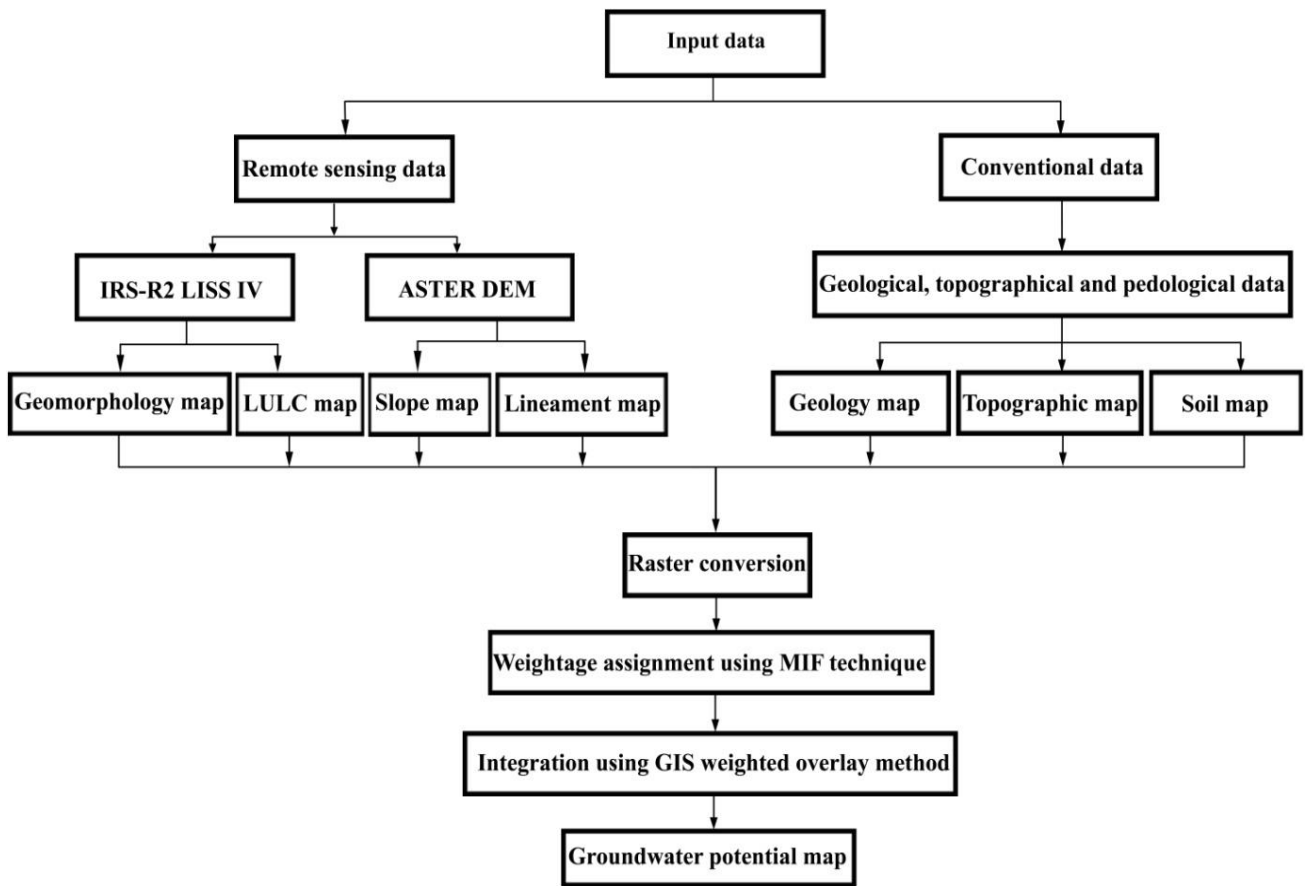


Figure 2. Schematic diagram of the methodology followed for groundwater potential zones

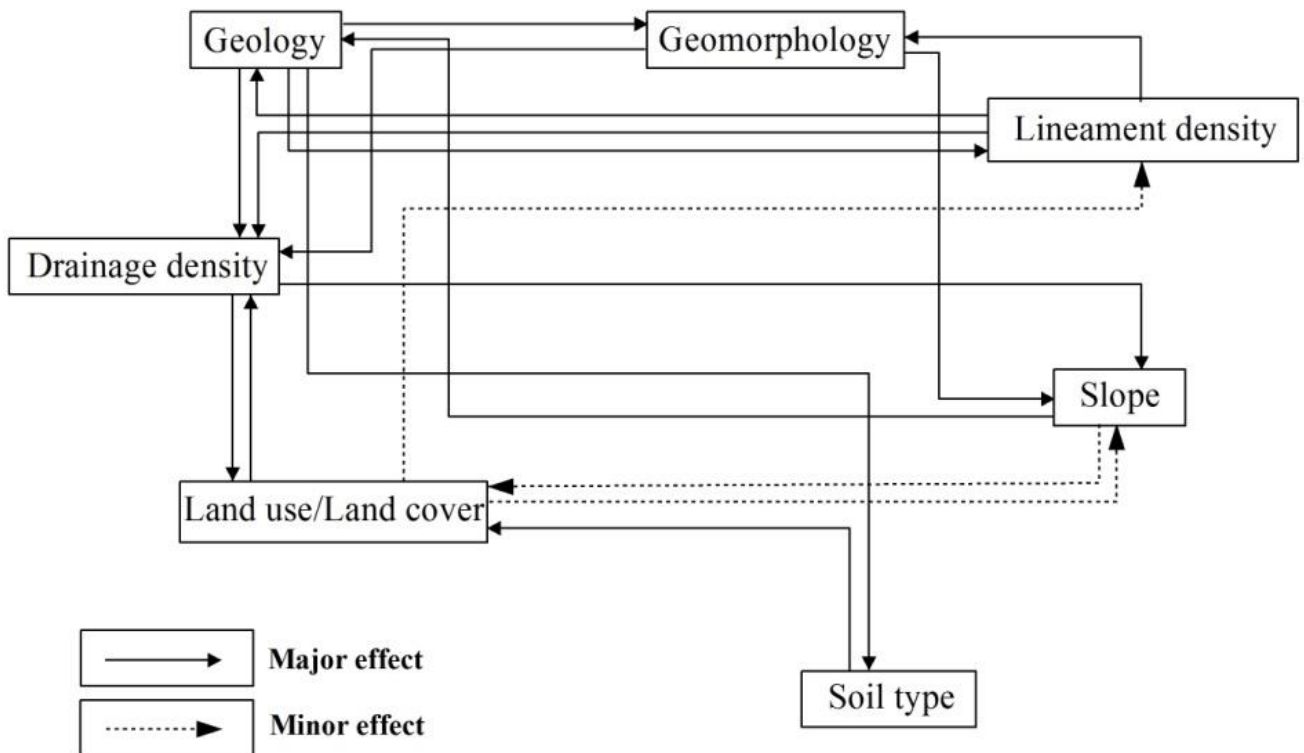


Figure 3. Schematic diagram of major and minor influence factors for groundwater potential zones

RESULTS AND DISCUSSION

The description of each thematic map and its relation to groundwater potentiality is discussed below.

Geology

Geology plays a vital role in the occurrence and movement of groundwater, especially in hard rock terrains. In general, the occurrence and movement of groundwater in such terrains are confined to weathered and fractured horizons which are essentially controlled by secondary porosity in terms of fractures, faults and fissures of underlying rocks (Chaudhary and Kumar 2018; Rai and Thiagarajan, 2019). Geologically, the study area consists mainly of Archaean- hornblende-biotite gneiss, granodiorite and granitoid gneiss, middle Proterozoic quartzites, shales and phyllites and recent alluvium deposits along the course of the Swarnamukhi River (Figure 4a). The River was assigned a higher weight, followed by granites, shales/phyllites, and quartzites respectively.

Lineament density

Lineaments are the major factors that influence the occurrence and movement of groundwater in an aquifer. These linear features act as conduits for groundwater movement, especially in hard rock terrain (Selvam et al., 2015). The lineament map was generated from ASTER DEM 30m resolution data. After field checks, the lineament density map was prepared using line density tool in GIS. The lineaments are oriented in ENE-WSW, followed by NNW-SSE and N-S direction. In the study area, three lineament density categories were identified viz. low, medium and high (Figure 4b). The high lineament density area has good

groundwater prospects while the low lineament density area has low groundwater prospects. Hence, a higher rating was assigned to high lineament density, followed by medium and low.

Geomorphology

Geomorphology plays an essential role in understanding the evolution of landforms and its control of groundwater occurrence and movement (Thapa et al., 2017). The geomorphology of the study area has been classified into structural hills (SH), followed by pediplain deep weathered (PPD), pediplain shallow weathered (PPS), pediplain moderate weathered (PPM), cuesta (C), piedmont slope (PS), pediment (PD), valley fill (VF), residual hill (RH), inselberg (I) and Bajada moderate (BJM) (Figure 4c). Structural hills, residual hills, cuesta, piedmont slope and pediment act, have poor groundwater prospects. Pediplain shallow has poor to moderate groundwater prospects. The pediplain moderate and pediplain deep, valley fills, and bajada moderate, have good groundwater prospects whereas, the alluvial plains have very good groundwater prospects. Accordingly, ratings are assigned.

Land use/Land cover (LULC)

The LULC has a significant impact on groundwater recharge (Shaban, 2006; Selvam et al., 2015). The major land use/land cover patterns in the study area are forest land, cropland, settlements, wastelands, and water bodies (Figure 4d). Because of its high groundwater recharge nature, high priority was given to forest land, cropland and water bodies. While low priority was given to settlements and wastelands due to their low groundwater recharge.

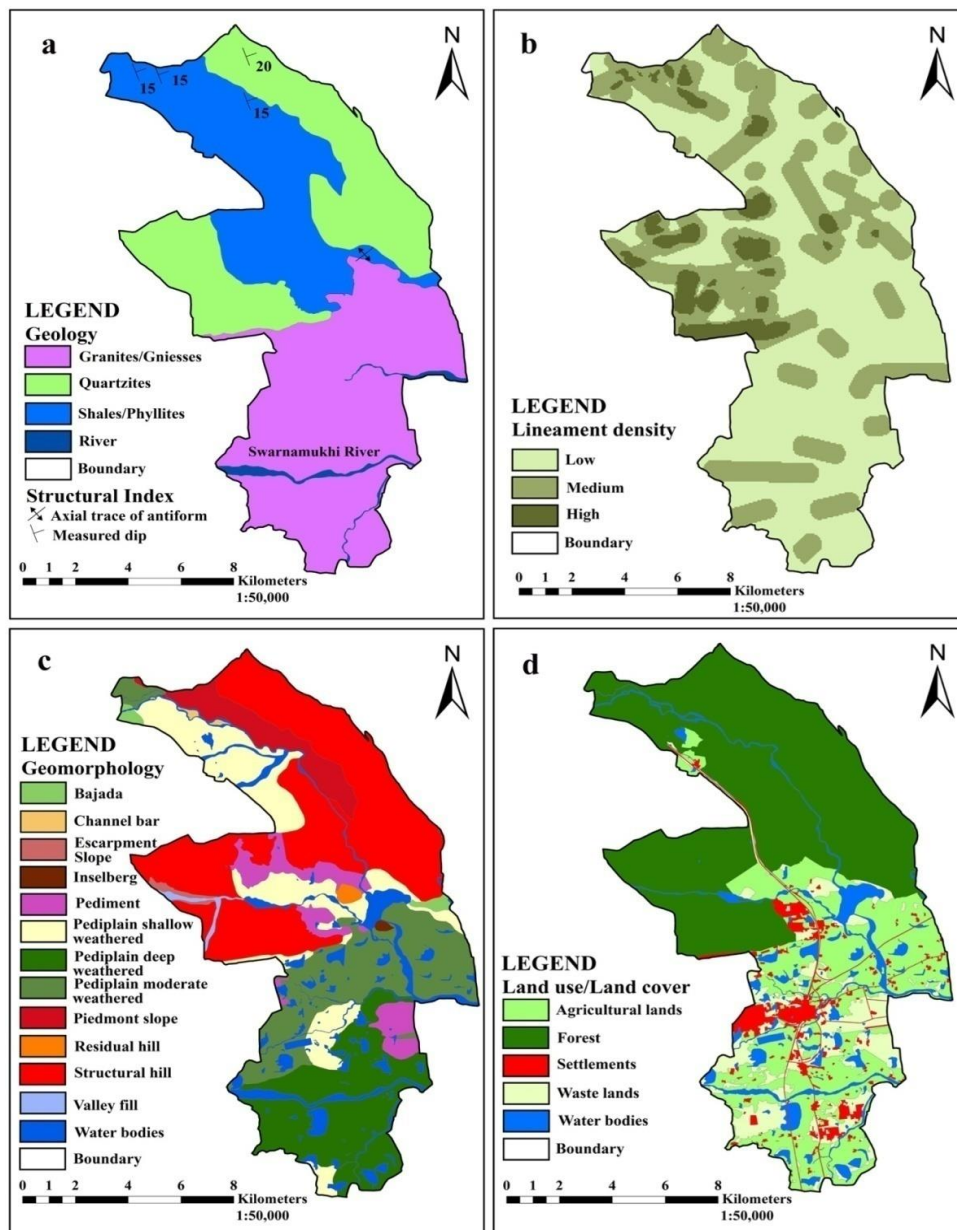


Figure 4. (a) Geology map, (b) Lineament density map, (c) Geomorphology map, and (d) Land use/Land cover map of the study area

Drainage density

Drainage density plays a crucial role in evaluating groundwater resources as the recharge rate is controlled by the drainage system. In general, the higher the drainage density, the lower the recharge rate will be (Singh et al., 2013; Rajaveni et al., 2015). The drainage map was prepared from toposheets and satellite imagery and the drainage density map was prepared using line density tool in GIS. The predominant drainage pattern is dendritic to a sub dendritic. Based on the results, three drainage density categories were identified in

the study area viz. low, medium and high (Figure 5a). The highest rating was allocated to low drainage density category followed by the medium and high drainage density categories respectively.

Soils

Soil plays a vital role in groundwater recharge by infiltration of water into the subsurface of the earth. The rate of infiltration depends mainly on the soil type and associated soil hydraulic characteristics (Das, 2017). The soil map was generated from district resources map. In the

study area, the predominant soil types are red shallow gravelly loam soils, red shallow gravelly clay soils, red shallow gravelly clay soils, red clay soils, brown clayey soils and brown gravelly loam soils (Figure 5b). Red shallow gravelly loam and brown gravelly loam soils were assigned a higher rating, followed by red shallow gravelly clay, brown clayey and red clay soils respectively.

Slope

Slope plays a crucial role in the infiltration of water into the subsurface layers of the earth. Steep slope faster the cumulative runoff of

surface water during high rainfall events, whereas the gentle slope lowers the surface runoff and percolates more water into the subsurface (Magesh et al., 2012; Selvam et al., 2015). The slope map was generated using ASTER DEM 30m resolution data. The northern parts have steep slopes, while the southern parts have gentle slopes (Figure 5c). Southern portions exhibit gentle slopes which significantly augment the infiltration of water into the subsurface of the earth and hence highest rating is given.

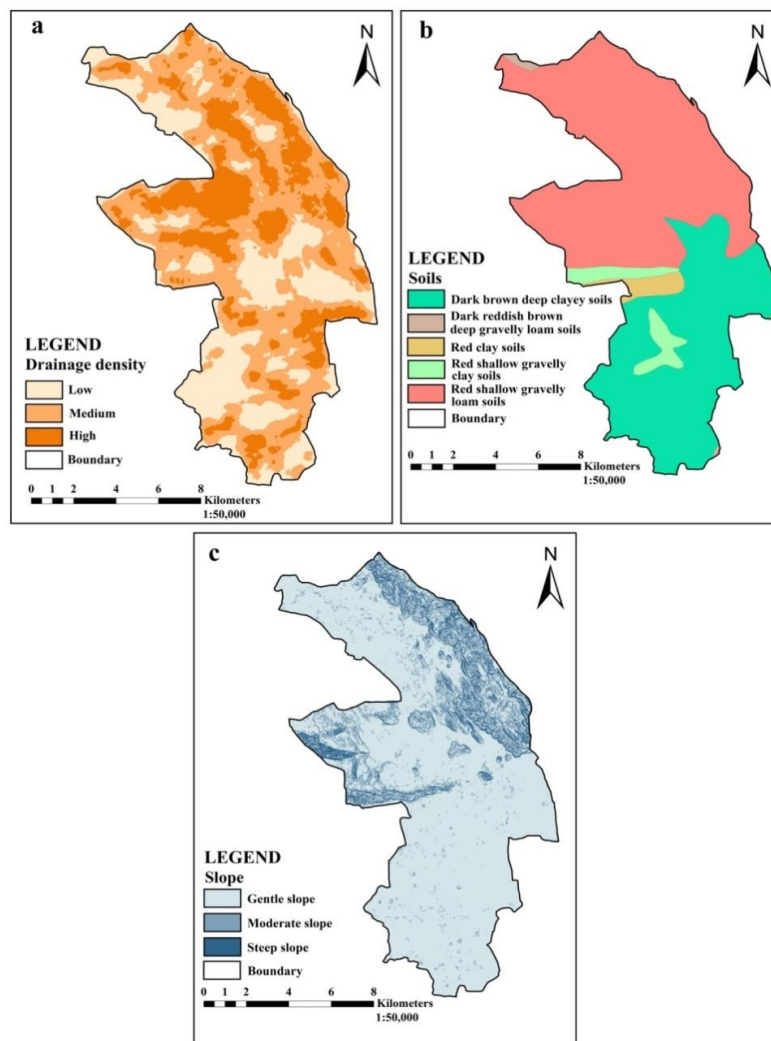


Figure 5. (a) Drainage density map, (b) Soil map, (c) Slope map of the study area

Groundwater potential zones

The final groundwater potential zones map using MIF technique and weighted overlay process results into four groundwater potential

zones viz., poor 46.46 km² (21.75%), moderate 109.99 km² (51.49%), good 51.62 km² (24.17%) and very good 5.53 km² (2.59%). From (Figure 6), it is found that about 73.24%

of the area falls under poor to moderate groundwater potential zones. Strict policy formulations should be implemented to avoid new construction of bore wells in these areas. The remaining 26.76% falls under good to very

good groundwater potential zones. Good to very good groundwater potential zones are suitable for agriculture activities and construction of bore wells.

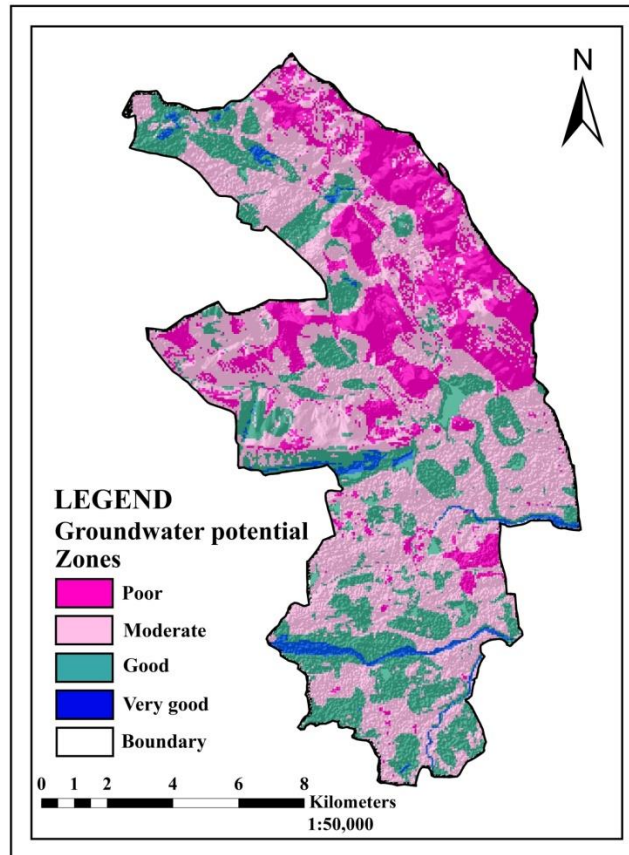


Figure 6. Groundwater potential zones map

CONCLUSION

An attempt has been made to evaluate groundwater potential zones of Renigunta area using remote sensing, GIS and MIF techniques. These techniques proved as rapid and cost-effective tools in evaluating groundwater resources. Various thematic maps such as geology, lineament density, land use/land cover, geomorphology, drainage density, soils and slope maps were prepared in GIS. Then each thematic map and their subclasses were given weight and rating by using MIF technique and integrated using weighted overlay tool in GIS. The resulted map was categorised into poor (21.75%), moderate (51.49%), good (24.17%) and very good (2.59%) groundwater potential

zones. The major part of the study area has poor to moderate groundwater potential zones whereas good to very good potential zones confined to limited spatial extents. This study is useful in planning and management scenario of groundwater resources of Renigunta area. The proposed methodology can be applied in similar terrains for sustainable management of groundwater resources.

ACKNOWLEDGEMENTS

The first author E. Balaji is thankful to the Council of Scientific and Industrial Research (CSIR), New Delhi for providing financial assistance and anonymous reviewers, whose comments have greatly improved this manuscript.

Compliance with Ethical Standards

The authors declare that they have no conflict of interest and adhere to copyright norms.

REFERENCES

- Aouragh, M.H., Essahlaoui, A., El Ouali, A., El Hmaidi, A. and Kamel, S., 2016. Groundwater potential of Middle Atlas plateaus, Morocco, using fuzzy logic approach, GIS and remote sensing. *Geomatics, Natural Hazards and Risk.*, 8(2), 194 -206.
- Arabameri, A., Rezaei, K., Cerda, A., Lombardo, L. and Rodrigo-Comino, J., 2019. GIS-based groundwater potential mapping in Shahroud plain, Iran. A comparison among statistical (bivariate and multivariate), data mining and MCDM approaches. *Science of the Total Environment.*, 658, 160 -177.
- Balaji, E., Veeraswamy, G., Peiyue, L. and SiddiRaju, R., 2019a. Deciphering Groundwater Potential Zones using MIF Technique and GIS: A study from Tirupati area, Chittoor District, Andhra Pradesh, India. *HydroResearch.*, 1, 1-7.
- Balaji, E., Veeraswamy, G., Narsimha A. and Subba Rao, M., 2019b. Factors controlling groundwater chemistry of Renigunta area, Chittoor District, Andhra Pradesh, South India. A multivariate statistical approach. *HydroResearch.*, 1, 57-62.
- Chaudhary, B.S. and Kumar, S., 2018. Identification of Groundwater Potential Zones using Remote Sensing and GIS of K-J Watershed, India. *J. Geol. Soc. India.*, 91(6), 717 - 721.
- Das, S., 2017. Delineation of groundwater potential zone in hard rock terrain in Gangajalghati block, Bankura district, India using remote sensing and GIS techniques. *Modeling Earth Systems and Environment.*, 3(4), 1589 -1599.
- GhorbaniNejad, S., Falah, F., Daneshfar, M., Haghizadeh, A. and Rahmati, O., 2016. Delineation of groundwater potential zones using remote sensing and GIS-based data-driven models. *Geocarto Int.*, 32, 167-187.
- Magesh, N.S., Chandrasekar, N. and Soundranayagam, J.P., 2012. Delineation of groundwater potential zones in Theni district, Tamil Nadu, using remote sensing, GIS and MIF techniques. *Geosci. Front.*, 3(2), 189 -196.
- Moghaddam, D.D., Rezaei, M., Pourghasemi, H.R., Pourtaghie, Z.S. and Pradhan, B. 2013. Groundwater spring potential mapping using bivariate statistical model and GIS in the Taleghan Watershed, Iran. *Arabian J.Geosci.*, 8(2), 913 - 929.
- Mohammadi-Behzad, H.R., Charchi, A., Kalantari, N., Nejad, A.M. and Vardanjani, H.K. 2018. Delineation of groundwater potential zones using remote sensing (RS), geographical information system (GIS) and analytic hierarchy process (AHP) techniques: a case study in the Leylia–Keynow watershed, southwest of Iran. *Carbonates and Evaporites.*, 1-13.
- Nasir, M.J., Khan, S., Zahid, H. and Khan, A., 2018. Delineation of groundwater potential zones using GIS and multi influence factor (MIF) techniques: a study of district Swat, Khyber Pakhtunkhwa, Pakistan. *Environmental Earth Sci.*, 77(10), 1-11.
- Panahi, M.R., Mousavi, S.M. and Rahimzadegan, M., 2017. Delineation of groundwater potential zones using remote sensing, GIS, and AHP technique in Tehran–Karaj plain, Iran. *Environmental Earth Sci.*, 76, 792, 1-15.
- Rai, S.N. and Thiagarajan, S., 2019. Delineation and sustainable development of groundwater resources in granitic terrain using electrical resistivity tomography. *J. Ind. Geophys. Union.*, 23(2), 109 -119.

- Rajaveni, S. P., Brindha, K. and Elango, L., 2015. Geological and geomorphological controls on groundwater occurrence in a hard rock region. *Applied Water Sci.*, 7(3), 1377 - 1389.
- Sashikkumar, M.C., Selvam, S., Kalyanasundaram, V.L. and Johnny, J.C., 2017. GIS based groundwater modeling study to assess the effect of artificial recharge: A case study from Kodaganar river basin, Dindigul district, Tamil Nadu. *J. Geol. Soc. India.*, 89(1), 57 - 64.
- Selvam, S., Dar, F.A., Magesh, N.S., Singaraja, C., Venkatraman, S. and Chung, S.Y., 2015. Application of remote sensing and GIS for delineating groundwater recharge potential zones of Kovilpatti Municipality, Tamil Nadu using IF technique. *Earth Sci. Informatics.*, 9(2), 137 - 150.
- Shaban, A., Khawlie, M. and Abdallah, C., 2006. Use of remote sensing and GIS to determine recharge potential zone: the case of Occidental Lebanon. *Hydrogeol. J.*, 14, 433-443.
- Shekhar, S. and Pandey, A.C., 2015. Delineation of groundwater potential zone in hard rock terrain of India using remote sensing, Geographic information system (GIS) and analytic hierarchy process (AHP) techniques. *Geocarto Int.*, 30, 402 - 421.
- Singh, P., Thakur, J.K. and Kumar, S., 2013. Delineating groundwater potential zones in a hard-rock terrain using geospatial tool. *Hydrological Sci. J.*, 58(1), 213 - 223.
- Thapa, R., Gupta, S., Guin, S. and Kaur, H., 2017. Assessment of groundwater potential zones using multi-influencing factor (MIF) and GIS: a case study from Birbhum district, West Bengal. *Appl. Water Sci.*, 7(7), 4117- 4131.
- The World Bank, 2010. Deep wells and prudence: towards pragmatic action for addressing groundwater overexploitation in India.
- Tiwari, A.K., Lavy, M., Amanzio, G., De Maio, M., Singh, P.K. and Mahato, M.K., 2017. Identification of artificial groundwater recharging zone using a GIS-based fuzzy logic approach: a case study in a coal mine area of the Damodar Valley, India. *Appl. Water Sci.*, 7(8), 4513- 4524.

Received on: 23.3.19; Revised on: 4.5.19; Accepted on: 2.6.19

A Report of the 55th Annual Convention of Indian Geophysical Union (IGU)

Kalachand Sain, ASSSRS Prasad, Md. Rafique Ahmad and Suryanshu Chowdhary

The 55th Annual Convention of Indian Geophysical Union (IGU) on the main theme “Changing Water Cycle and Water Resources” was jointly organized by Rabindranath Tagore University (RNTU), Bhopal and IGU, Hyderabad at RNTU, Bhopal during December 4-7, 2018. It started with the one-day pre-workshop on 4th December, 2019 for the benefit of students pursuing research on “Hard Rock Hydrogeology and estimating Groundwater Balance/Budget under Changing Climate”. It was planned for 6 Lectures (plus Introduction and Conclusions) covering different topics related to groundwater prospecting and surface geophysical techniques. Prof. Shakeel Ahmed, of JMI-Central University, Delhi provided a fascinating insight into the aquifer system and a glimpse of current scenario for groundwater management. Other faculty members were from CSIR-NGRI. Around 50 students participated to this workshop that engaged them in various logical exercises to get acquainted with the case studies.

Shri Santosh Choubey, Chancellor of RNTU was the Chief Guest at the Inaugurated Function on 5th December. He emphasized on the importance of geoscientific studies for the Science & Society, and remarked that water is not only a basic need but a fundamental human right that is supposed to be available in right quantity with right quality at right places. He suggested that India needs revolution in the area of water for socio-economic development. Prof Shailesh Nayak, President of IGU & Former Secretary of MoES and at present Director of NIAS underlined the necessity of remote sensing technique in geosciences and integrating the lithosphere, atmosphere and ionosphere for understanding numerous issues related to groundwater and climate change. He also stressed upon the geophysical survey for groundwater monitoring and measuring water level. He further motivated the researchers to take up geoscientific profession to meet the societal challenges, as there lies huge scopes and opportunities. Prof A.K. Gwal, VC of RNTU and LoC Chairman highlighted the importance of groundwater sustainability and its dependency on climate change in context of India. Dr. Kalachand Sain, Honorary Secretary of IGU and Chief Scientist at CSIR-NGRI gave an exhaustive report of IGU activities and explained why IGU has been organizing the convention every year – to provide a platform to the researchers for presentation of their works and receiving feedback from peers to improve further; creating a network for collaboration; interaction with experienced researchers; understanding societal issues and approach for mitigation; gaining knowledge for multi-disciplinary research; listening to experts on new results, discoveries, concepts, views etc., and recommending suitable measures by the policy-makers for the welfare of the society on a specific subject. This year, it was in the area of changing water cycle and water resources. During the inaugural program. The prestigious National Awards, which were conferred by Shri Santosh Choubey to both Young and Senior Scientists/Academicians for their outstanding contribution to Earth Sciences, are: IGU-Hari Narain Lifetime Achievement Award, IGU-Decennial Award, IGU-Krishnan Medal, IGU-Anni Talwani Memorial Prize, IGU- J.G. Negi Young Scientist Award, and IGU-Prof. D. Lal Best Paper Award. The inauguration ended with the vote of thanks proposed by Dr. Suryanshu Choudhary, LoC Convener followed by a group photograph. There were about 300 delegates from different Indian Universities, Research Institutes and organizations as well as from abroad.

The structure of the convention, spread over four days, consisted of 1 Full-day pre-workshop on 4th December; and Inaugural Session, 2 Plenary Sessions by 7 distinguished speakers, 7 Technical Sessions for 45 contributory oral presentations with 7 invited talks, 1 dedicated Technical Session with 85 posters display, and Concluding Session during December 5-7, 2019. The convention covered several areas of Solid Earth and Marine Geosciences, and Atmospheric & Space Sciences. In the first Plenary Session, chaired by Prof Shailesh Nayak, the most prestigious Prof. K.R. Ramanathan Memorial Lecture of IGU was delivered by Dr. Madhvan Nair Rajeevan, Secretary, MoES, GoI on ‘recent developments in weather and climate prediction in India’. This was followed by the lecture on ‘status of water resources in India’ by Prof P. Rajendra Prasad from Andhra University. Prof. Mrinal K. Sen from the University of Texas at Austin, USA delivered the third lecture on contemporary ‘physics based machine

learning for geophysics'. The Technical Session-I on Solid Earth Geosciences was chaired by Prof. Shakeel Ahmed and Dr. N. Purnachandra Rao, Director of ESSO-NCESS. They delivered invited talks on 'Knowledge based groundwater management to tackle the impact of climate change on water cycle' and 'Ambient Noise Tomography- A potential tool for Earth Structure, Exploration and Geo-hazards' respectively. The Technical Session-II (Young Researcher Program), chaired by Dr. O.P. Mishra, Joint Secretary of IGU and Senior Scientist at MoES and Dr. O.P. Pandey, Chief Editor of Journal of IGU, was specially designed to encourage the young researchers who just submitted their Ph.D. thesis or were awarded during the last one year time with the Best Presenter Award. In the Technical Session-III, jointly organised by IGU & ISES and chaired by Dr. V. M. Tiwari, Director of CSIR-NGRI and Dr. B.K. Rastogi, Retd. DG of ISR, Prof. Chalapathi Rao from BHU delivered an invited talk on 'sub-continental lithospheric mantle beneath NW India: New insights from the lamprophyres & their entrained xenoliths'. In the evening of the first day, the Pratibhalaya Arts Academy and RNTU Student performed amazing cultural program on the theme based on the Ramayana.

In the second Plenary Session, chaired by Prof Shailesh Nayak on 6th December, the first talk was delivered by Prof. Harsh Gupta, renowned seismologist & former Secretary of MoES on 'Coping with earthquakes in Himalayas'. This was followed by Dr. H.N. Siddiquie Memorial Lecture of IGU on 'sustainable anthropocene: scientific, political and ethical challenges' by Prof. Jagadish Shukla, Distinguished Professor at George Mason University, USA. Subsequently, two other talks on 'ground-water resources and application of geophysical techniques exploration, development and management in the context of Madhya Pradesh' by Dr. Subhash Singh from MP-CGWB; and on 'climate change and groundwater exploration in the Himalaya - geophysical vs. geological' by Dr. Ritesh Arya from Water and Geothermal Wing, International Sustainable Energy Organisation, Geneva, were delivered.

In the Technical session-IV, chaired by Prof A.K. Gwal, VC of RNTU and Dr. Kalachand Sain, Chief Scientist of CSIR-NGRI, the first talk was delivered by Dr. Sain on 'Influence of Rajmahal volcanism on the architecture of West Bengal sedimentary basin from seismic tomography'. To encourage researcher scholars, researchers and postgraduate students of Earth System Sciences, a dedicated 3-Hour Technical Session-V with ~80 scientific posters, inaugurated by Prof. Harsh Gupta, was organized in the afternoon of 6th December, 2019 for better interaction among delegates. This created a great enthusiasm, and the Best Posters Awards were given to the students and research scholars in recognition to their performances, as adjudged by a Jury consisting of Dr. O.P. Mishra and Dr. O.P. Pandey. A local visit to the Bhojpur Temple (Lord Shiva) was also arranged in the evening.

On 7th December, In the Technical Session-VI, chaired by Prof. P. Rama Rao from Andhra University, Dr. Tarun Khanna delivered an invited talk on 'Evolution of the Dongargarh Supergroup' followed by the Technical Session-VII, chaired by Dr. P. Sanjeeva Rao, Former Scientist.G at SERB-DST in which Dr. M. J. Nandan, PME-Head at CSIR-NGRI delivered an invited talk on 'assessment of groundwater quality and salinity dynamics in the central Godavari delta, AP'. Prof A. K. Gwal delivered an invited talk on 'detection of some powerful earthquake precursors by DEMETER satellite' in the last Technical Session VII, chaired by Dr. B.K. Rastogi.

IGU Awards for year 2018

IGU-Prof. K.R. Ramanathan Memorial Lecture

Dr. Madhavan Nair Rajeevan, MoES, GoI, New Delhi

IGU- Dr. Hari Narain Lifetime Achievement Award

Dr. Manik Talwani, Rice University, USA

IGU-Dr. H.N. Siddiquie Memorial Lecture

Prof. Jagadish Shukla, George Mason University, USA

IGU- Krishnan Medal

Dr. Tarun C. Khanna, CSIR-NGRI, Hyderabad

IGU- Anni Talwani Memorial Prize

Dr. N.V. Chalapathi Rao, BHU, Varanasi

IGU- Dr. JG Negi Young Scientist Award

Dr. R. Rajesh, CSIR-NGRI, Hyderabad

Young Researcher Program: Best Presenter Award

Mr. Priyadarshi Chimmoy Kumar, CSIR-NGRI, Hyderabad

Mr. Pankaj Bhardwaj, Kurukshetra University, Kurukshetra

IGU-ONGC Best Poster Awards**Research Scholars Category**

Mr. Rowtu Ramu, CSIR-NGRI, Hyderabad

Mr. Shubham Choudhary, WIHG, Dehradun

Ms. Dharmita Horo, IIT(ISM), Dhanbad

Student Category

Ms. Pousali Mukherjee, IISER, Kolkata

Ms. Simran & Mr. Shyam Chouhary, Kurukshetra University, Kurukshetra

Post-Doc, Research Associate and other Researchers

Dr. Amrita Singh, CSIR-NGRI, Hyderabad

IGU- Prof. Jegdeo Singh and Dr. S. Balakrishna Memorial Grant for Student Toppers (M.Sc. & M. Tech)

Geophysics, Osmania University, Hyderabad

1. Mr. Shaik Nasif Ahmed

2. Ms. Kandepu Swapnasri

Applied Geophysics, Kurukshetra University, Kurukshetra

1. Mr. Aman

2. Mr. Ashish Jangra

Geophysics, Andhra University, Vizag

1. Ms. P. Lathasri

2. Ms. G. Jayasri

Marine Geophysics, Andhra University, Vizag

1. Ms. Siripurapy Srivalli
2. Mr. Rajana Sivasai Kumar

Marine Geophysics, Cochin University of Science and Technology (CUSAT), Cochin

1. Mr. Gilbert M. George
2. Mr. Shijin K.K.

Earth Sciences (Geophysics), Swami Ramanand Teerth Marathwada University, Nanded

1. Ms. Shette Sneha Madhavrao
2. Ms. Kadam Shweta Bhujangrao

Geo- Technology, Manonmaniam Sundaranar University, Tirunelveli

1. Ms. Rema Vaishali
2. Ms. Muthulakshmi V

Applied Geophysics, IIT(ISM), Dhanbad

5-Year

1. Ms. Khushbu Kumari
2. Ms. Arnab Banerjee

3-Year

1. Ms. Sohini Dasgupta
2. Ms. Shrishti Gaur

Geosciences, Dr.BR Ambedkar University, Srikakulam

1. Mr. K.V. R.H. Prasad
2. Mr. K. Chinnam Naidu
2. Mr. N. Inya Raju

Geophysics, Adikavi Nannaya University, Rajamahendravaram

1. Mr. P. Chandra Sekhar
2. Ms. P. Manasa

IISER-Kolkata, Department of Earth Sciences, Kolkata

1. Ms. Srijita Ray
2. Ms. Pousali Mukherjee

Geophysics, Banaras Hindu University, VARANASI

1. Mr. Shubham Shukla
2. Ms. Jyoti Yadav

Geophysics, IIT Mumbai, Mumbai

1. Mr. Debraj Midya
2. Ms. Aashruti

Geophysical Technology, IIT Roorkee, Roorkee

Ms. Proyanka Choudhary

Anni Talwani Memorial Grant for Women Researchers

Ms. Jenifer Alam, Dept. of Applied Geophysics, IIT(ISM), Dhanbad

Ms. Anju K Joshi, Marine Seismics, Seismic Group, CSIR-NGRI, Hyderabad

Ms. Jayashree Ghosh, ESSO-Indian National Centre for Ocean Information Services, Hyderabad

Ms. Neetha Raj, Dept. of Geology & Geophysics, Adikavi Nannaya University, Rajamahendravaram

Ms. Poulommi Mondal, Geosciences and Technology Division of CSIR-NEIS, Jorhat

Ms. K. S. Sreenidhi, Dept. of Earth Sciences, Indian Institute of Technology Bombay, Mumbai

Ms. Triveni Gogoi, Dept. of Applied Geophysics, IIT(ISM), Dhanbad

At the Concluding Session of IGU, Prof. Shailesh Nayak appreciated the research scholars, research fellows, and PG and undergraduate students for their excellent posters during the convention and advised them to achieve excellence in whatever geoscientific field they pursue their research. Prof R.J. Rao, Vice Chancellor of Barkatullah University was the Chief Guest and Dr. Navin Chandra, Director General of Madhya Pradesh Council of Science and Technology, Bhopal was the Guest of Honour at the function. While addressing the gathering, Dr. Navin Chandra communicated to all scientists, academicians, research scholars and students in strengthening our nation scientifically, particularly in the area of geosciences and geophysics. He applauded the IGU in playing active role for the wellbeing of Society through Geosciences, and convening sessions in motivating students and young researchers. Prof R.J. Rao shared the importance of ground water resources for sustainable development of Earth, and congratulated IGU for organizing the 55th convention in Bhopal, MP. Both the Chief Guest and the Guest of Honour handed over various Awards, Cash Prizes, Mementoes, Trophy and Certificates to the delegates, research scholars, students for their performance at the 55th IGU.

IGU places on record the financial support received from National Centre for Polar and Ocean Research (NCPOR), Goa; Oil and Natural Gas Cooperation ONGC, Dehradun, Indian National Centre for Ocean Information Services (INCOIS), Hyderabad; National Centre for Earth Science Studies (NCESS), Thiruvananthapuram; CSIR-National Geophysical Research Institute (NGRI), Hyderabad; CSIR-National Institute of Oceanography (NIO), Goa; Physical Research Laboratory, Ahmadabad; Indian Space Research Organization (ISRO), Bengaluru; National Remote Sensing Centre (NRSC), Hyderabad, CSIR-National Environmental Engineering Research Institute (NEERI), Nagpur and CSIR- Central Institute of Mining and Fuel Research (CIMFR).

The 55th Annual Convention of IGU was concluded by rendering the Indian National Anthem.

Glimpses of 55th Annual Convention of IGU



GUIDE FOR AUTHORS

The Journal of Indian Geophysical Union (J-IGU), published bimonthly by the Indian Geophysical Union (IGU), is an interdisciplinary journal from India that publishes high-quality research in earth sciences with special emphasis on the topics pertaining to the Indian subcontinent and the surrounding Indian Ocean region. The journal covers several scientific disciplines related to the Earth sciences such as solid Earth geophysics, geology and geochemistry, apart from marine, atmosphere, space and planetary sciences. J-IGU welcomes contributions under the following categories:

- Research papers and short notes reporting new findings.
- Review articles providing comprehensive overview of a significant research field.

In addition, J-IGU also welcomes short communications, after communications and report on scientific activity, book reviews, news and views, etc.

The manuscript should be submitted electronically as a single word format (.doc file) including the main text, figures, tables, and any other supplementary information along with the signed "Declaration Letter". The manuscript should be submitted by email (jigu1963@gmail.com) to the Chief Editor.

After acceptance of the manuscript the corresponding author would be required to submit all source files (text and Tables in word format) and figures in high resolution standard (*.jpg, *.tiff, *.bmp) format. These files may be submitted to J-IGU as a single *.zip file along with the "Copyright Transfer Statement".

IMPORTANT INFORMATION

Ethics in publishing

J-IGU is committed to ensuring ethics in publication and takes a serious view of plagiarism including self-plagiarism in manuscripts submitted to the journal. Authors are advised to ensure ethical values by submitting only their original work and due acknowledgement to the work of others used in the manuscript. Authors must also refrain from submitting the same manuscript to more than one journal concurrently, or publish the same piece of research work in more than one journal, which is unethical and unacceptable. Editor of J-IGU is committed to make every reasonable effort to investigate any allegations of plagiarism brought to his attention, as well as instances that come up during the peer review process and has full authority to retract any plagiarized publication from the journal and take appropriate action against such authors if it is proven that such a misconduct was intentional.

Similarly, Editor and Reviewers are also expected to follow ethical norms of publishing by ensuring that they don't use any unpublished information, communicated to them for editorial or review purpose, in their own research without the explicit written consent of the author. They are also expected to keep manuscript/ data/ observations/ any other information related to the peer review confidential to protect the interest of the authors. Reviewers should refrain from reviewing the manuscripts in which they have conflicts of interest resulting from competitive, collaborative, or other relationships or connections with any of the authors, companies, or institutions connected to the manuscript.

Conflict of interest

All authors are requested to disclose any actual or potential conflict of interest including any financial, personal or other relationships with other people or organizations within three years of beginning the submitted work that could inappropriately influence, or be perceived to influence, their work.

Submission declaration

Submission of a manuscript implies that the work has not been published previously and it is not under consideration for publication elsewhere, and that if accepted it will not be published elsewhere in the same or any other form, in English or in any other language, without the written consent of the publisher. It also implies that the authors have taken necessary approval from the competent authority of the institute/organization where the work was carried out.

Copyright

After acceptance of the manuscript the corresponding author would be required to sign and submit the "Copyright Transfer Statement".

MANUSCRIPT PREPARATION

The corresponding author should be identified (include E-mail address, Phone/Mobile number). Full affiliation and postal address must be given for all co-authors.

Abstract:

An abstract of not more than 300 words must be included.

Text:

The manuscript should be structured to include a front page containing the title, Author(s) name, affiliation and address of the institute, where

the work was carried out, a short title, and 5-to-6 Key words. Author(s) present address, if different from the above mentioned address, may be given in the footnote. The corresponding author should be identified with an asterisk and his/her email ID should be provided. This page should be followed by the main text consisting of Abstract, Introduction, Methods/ Techniques/ Area description, Results, Discussion, Conclusions, Acknowledgements, and References. Tables and Figures with captions should be inserted at the end of main text. It should not be inserted in the body of the text.

Figures/ Illustrations:

All figures should be provided in camera-ready form, suitable for reproduction (which may include reduction) without retouching. Figures in high-resolution (at least 300 dpi) standard formats (*.jpg, *.tiff, *.bmp) are acceptable. Figures should be numbered according to their sequence in the text. References should be made in the text to each figure. Each figure should have a suitable caption.

Tables:

Authors should take note of the limitations set by the size and layout of the journal. Table should not exceed the printed area of the page. They should be typed on separate sheets and details about the tables should be given in the text. Heading should be brief. Large tables should be avoided and may be provided as supplementary information, if required.

Equations:

Equations should be numbered sequentially with Arabic numerals and cited in the text. Subscripts and Superscripts should be set off clearly. Equation writing software that presents each equation as an object in MS Word will be accepted. Style and convention adopted for the equations should be uniform throughout the paper.

References:

All references to publications cited in the main text should be presented as a list of references in order following the text and all references in the list must be cited in the text. References should be arranged chronologically, in the text. The list of references should be arranged alphabetically at the end of the paper.

References should be given in the following form:

Kaila, K.L., Reddy P.R., Mall D.M., Venkateswarlu, N., Krishna V.G. and Prasad, A.S.S.R.S., 1992. Crustal structure of the west Bengal Basin from deep seismic sounding investigations. *Geophys. J. Int.*, 111,45-66.

REVIEW PROCESS:

All manuscripts submitted to the journal are peer-reviewed. It is advisable to send the contact details of 4 potential reviewers along with the manuscript to expedite the review process. Editor has the option to select reviewers from the list or choose different reviewers. The review process usually takes about 3 months. All enquiries regarding the manuscript may be addressed to the Editor.

GALLEY PROOF:

Technical editing of manuscripts is performed by the editorial board. The author is asked to check the galley proof for typographical errors and to answer queries from the editor. Authors are requested to return the corrected proof within two days of its receipt to ensure uninterrupted processing. The editor will not accept new material in proof unless permission from the editorial board has been obtained for the addition of a "note added in proof". Authors are liable for the cost of excessive alterations to galley proof.

PUBLICATION CHARGES:

There are no page charges for publication and printing charges for b/w figures. However, in view of substantial cost involved in printing of color figures, author will be charged for printing of pages containing color figures @ Rs. 2,500/- per page. The charges may be revised at any time based on cost of printing and production. Author will receive an estimate/ invoice of the color figures reproduction cost along with the galley proof. It is the responsibility of the author to remit the color figures reproduction cost within one month of the receipt of the estimate/invoice.

The corresponding author will receive a soft copy (pdf format) of his/her published article. Should the author desire to purchase reprints of his/her publication, he/she must send the duly signed Reprint Order Form (accompanies the galley proof and contains price details) along with the corrected galley proof to the Editor. The reprint charges must be paid within one month of sending the Reprint Order Form.

Any payment related to printing of color figures and/or purchase of reprints should be made in the form of a Demand Draft in the name of Treasurer, Indian Geophysical Union, payable at Hyderabad.

You may download the pdf file from: <http://www.j-igu.in/IGU-Guide-forAuthors.pdf>